

University of Southampton Research Repository

Copyright © and Moral Rights for this thesis and, where applicable, any accompanying data are retained by the author and/or other copyright owners. A copy can be downloaded for personal non-commercial research or study, without prior permission or charge. This thesis and the accompanying data cannot be reproduced or quoted extensively from without first obtaining permission in writing from the copyright holder/s. The content of the thesis and accompanying research data (where applicable) must not be changed in any way or sold commercially in any format or medium without the formal permission of the copyright holder/s.

When referring to this thesis and any accompanying data, full bibliographic details must be given, e.g.

Thesis: Author (Year of Submission) "Full thesis title", University of Southampton, name of the University Faculty or School or Department, PhD Thesis, pagination.

Data: Author (Year) Title. URI [dataset]

University of Southampton

Faculty of PHYSICAL SCIENCES AND ENGINEERING School of Physics and Astronomy

A study of $B \to \pi \ell \nu$ and $B_s \to K \ell \nu$ form factors using dispersive constraints

by

Callum Radley-Scott

MPhys

ORCiD: 0009-0009-3869-6238

A thesis for the degree of Doctor of Philosophy

May 2025

University of Southampton

Abstract

Faculty of PHYSICAL SCIENCES AND ENGINEERING School of Physics and Astronomy

Doctor of Philosophy

A study of $B \to \pi \ell \nu$ and $B_s \to K \ell \nu$ form factors using dispersive constraints by Callum Radley-Scott

This thesis presents several approaches to improve the extrapolation of form factors for the exclusive semileptonic decays $B \to \pi \ell \nu$ and $B_s \to K \ell \nu$. These decays are of interest for testing the predictions of the Standard Model.

These form factors cannot be calculated perturbatively, and so we rely on techniques such as Lattice QCD (Quantum Chromodynamics) to make theoretical predictions. For these heavy-to-light decays, Lattice QCD gives form factor information in a limited region of phase space and the results must be extrapolated to cover the entire kinematically-allowed region. Model-independent approaches based on dispersion relations are now widely used. The most common is Z-fits, but recently interest has been revived in what will here be called the Dispersive matrix (DM) approach.

The z-fit approach parametrizes the dispersion relations for these decays and uses lattice information to find optimal coefficients for the resulting curves. Approaches to improving the precision of this technique are explored, such as an alternative parametrization, and making use of information from multiple decays simultaneously.

The Dispersive Matrix method does not require parametrizing the form factor results (and so avoids any issues with truncation of the *z* expansion). This method finds the minimum and maximum values of the form factors allowed by unitarity using known form factor points. Modifications to the method are trialled, including using information from multiple decays simultaneously, improving numerical stability when computing the bounds, and optimising the implementation of a kinematic constraint relating the form factors.

A novel method to generating form factor curves using the Dispersive matrix method is introduced, alongside several optimisations to improve computation time. This new method is tested, and the results, namely for the Cabibbo–Kobayashi–Maskawa matrix element, $|V_{ub}|$, are compared to those from the Z-fit approach.

Contents

Li	st of	Figures	;	vii
Li	st of	Tables		xi
D	eclara	ation of	Authorship	xiii
A	cknov	wledge	ments	xv
1	Intr	oductio	on	1
2	Star	ndard N	Model	3
	2.1	Funda	amental Particles	4
	2.2	Symm	netries	4
	2.3	Electro	oweak Interactions	6
		2.3.1	The Electroweak Lagrangian	6
		2.3.2	Spontaneous Symmetry Breaking & the Higgs Mechanism	9
		2.3.3	Yukawa Interactions	12
		2.3.4	CKM Matrix	13
	2.4	Quant	tum Chromodynamics	16
	2.5		e QCD	18
		2.5.1	Path Integrals	19
		2.5.2	Importance sampling	20
	2.6	Semile	eptonic Decays	20
	2.7	Corre	lation functions	21
	2.8	Form	Factors and Phenomenology	23
		2.8.1	Differential Decay Rate	23
		2.8.2	Forward-Backward Asymmetry	24
		2.8.3	R Ratio	25
3	Stat	istical	Techniques	27
	3.1	Bootst	trapping	27
	3.2	Kolmo	ogorov–Smirnov test	27
4	Cho	ice of I	Oata Oata	29
	4.1		$ au\ell u$	29
			Combining data for Belle 2013	30
	4.2	$B_s \rightarrow$	$K\ell\nu$	31
5	Dis	persive	Bounds	33

vi CONTENTS

6	Z-Fi	ts		37		
	6.1	BGL P	arametrization	37		
	6.2	BCL P	arametrization	38		
	6.3	Fitting	Procedure	39		
	6.4	Unitar	ity constraint	40		
	6.5	Altern	ative polynomials	40		
	6.6	Z-Fits	with 2 decays	42		
		6.6.1	Method	45		
		6.6.2	Comparison with single decay	46		
	6.7	Extrac	ting V_{ub}	51		
		6.7.1	$B \to \pi \ell \nu$	51		
		6.7.2	$B_s \to K\ell\nu$	52		
7	Dis	ersive	Matrix method	55		
	7.1	The Di	spersive Matrix	55		
		7.1.1	Bootstrapping Procedure	59		
	7.2	Impro	ving Numerical Stability	61		
	7.3	Sampl	ing Across the Overlap Region	63		
	7.4		M method for two decays	65		
		7.4.1	Comparison with single-decay	66		
	7.5	Form I	Factor Curves from the DM method	67		
		7.5.1	Method	68		
		7.5.2	Generating curves across bins	70		
		7.5.3	'Marching' across the full q^2 range	71		
		7.5.4	Tests	71		
			7.5.4.1 Direction of curve generation	72		
			7.5.4.2 Dependence on δ	73		
			7.5.4.3 Dependence on interpolation method	73		
		7.5.5	Marching parameters	74		
			7.5.5.1 Marching threshold	75		
			7.5.5.2 Warning threshold and marching delay	75		
		7.5.6	Number of curves per resample	76		
		7.5.7	Extraction of V_{ub} for DM Curves	77		
8	Phe	nomeno	ology	83		
	8.1	Compa	arison with 2015 Results	83		
	8.2	Z-fit aı	nd DM Curve Results	83		
9	Con	clusion	s	89		
Aı	peno	dix A I	Reconstruction of phenomenological quantities	93		
-	-			97		
4 * }	Appendix B Derivation of the Outer Function 97					

List of Figures

2.1	Standard model of elementary particles [70, 91]	5
2.2	An illustration of the Higgs potential [67]	9
2.3	Global constraints on the CKM unitarity triangle in the $(\overline{\rho}, \overline{\eta})$ plane. The overlapping red ellipse indicates the region allowed at a 95% confidence level. [55]	16
2.4	Running of the strong coupling constant, denoted here as α_S , with energy scale Q [86]	17
2.5	Feynman diagram for $B \to \pi \ell \nu$	20
2.6	Sketch of a generic three-point function. The spectator quark (dot-dashed line) originates from time slice t_{src} and propagates forward to time slice t_{snk} where we create a point sink and turn it into a sequential source for the parent quark (double line) propagating backward. This sequential propagator is contracted with the child light quark (solid line) also originating from t_{src} . [88]	21
6.1	Sum of coefficients (10000 sets) squared for $B_s \to K\ell\nu$ and $B \to \pi\ell\nu$, fitted without consideration of the unitarity constraint, using synethetic form factor points from the RBC/UKQCD [88] and JLQCD [80] collaborations, respectively	40
6.2	A schematic depiction of the mapping from the q^2 -plane (left) to the conformal z -plane (right). The coloured segments on the real axis denote the physical and unphysical regions for the $B \to K$ decay form factors, while the circle on the right represents the boundary of the unit disk after the conformal transformation.	41
6.3	Distribution of BsK coefficients for the circle and arc (a restricted arc of the unit disc) models	43
6.4	Distribution of BsK coefficients for the circle and arc (a restricted arc of the unit disc) models	44
6.5	Distribution of BPi coefficients for single and dual (2-decay) fitting methods	47
6.6	CDF of BPi coefficients for single and dual (2-decay) fitting methods	48
6.7	Distribution of BsK coefficients for single and dual (2-decay) fitting methods	49
6.8	CDF of BsK coefficients for single and dual (2-decay) fitting methods	50
6.9	Differential decay rate from coefficients (Blue) plotted alongside experimental bins (yellow/green) and differential decay rate values from lattice form factor values (red)	52
6.10	χ^2 optimisation of the V_{uh} weighted mean.	54

viii LIST OF FIGURES

7.1	Form factor bounds calculated using the DM method for $B_s \to K\ell\nu$ using unitarity only	56
7.2	Example form factor bounds calculated using the DM method for $B_s \rightarrow K\ell\nu$ with the unitarity constraint and a set of form factor points. Here,	50
	the curves plotted represent the top and the bottom of the region allowed by unitarity.	58
7.3	Example form factor bounds calculated using the DM method for $B_s \rightarrow K\ell\nu$ with the unitarity and kinematic constraints and a set of form factor points. Here, the curves plotted represent the top and the bottom of the region allowed by unitarity. This plot is for a single resample of form factors, and so, has no errors.	60
7.4	Form factor bounds calculated using the DM method over 2000 bootstrap events for $B_s \to K \ell \nu$ with both the unitarity and kinematic constraints. Synthetic form factor data is from the RBC/UKQCD collabora-	
7.5	tion [88]	61
7.6	bottom	63
7.6	f_0 bounds at $q^2 = 15 \text{ GeV}^2$ for $B_s \to K\ell\nu$, as the synthetic data point is moved away from the bottom of the overlap region	64
7.7	Example form factor inputs from Lattice data, and their resulting bounds at $q^2 = 0$ Ge V^2	68
7.8	Step by step visualisation of how form factor curves are generated	69
7.9	100 curves generated for a single resample of JLQCD $B \to \pi \ell \nu$ synthetic data points [80]	70
7.10	100 curves generated for a single resample of JLQCD $B \to \pi \ell \nu$ synthetic	71
7.11	Comparing the distribution of form factor curves at $q^2 = 10 GeV^2$, when using intermediate points (at $q^2 = 1, 2,, 9 \text{ GeV}^2$) and when jumping	
	directly	72
7.12	Comparison of the cross-section of f_0 curves at $q^2 = 10 GeV^2$, when generated forwards and backwards. For each direction, we have the K-S test	
	p-value associated to an underlying uniform distribution	73
7.13	Calculation of $\Gamma V_{ub} ^{-2}$ using 500 form factor curves for various values of δ . The plotted bars indicate the median, 16th and 84th percentile values.	74
7.14	Calculation of $\Gamma V_{ub} ^{-2}$ using 500 form factor curves for various interpolation methods. The plotted bars indicate the median, 16th and 84th	
	percentile values	74
7.15	Dependence of $\Gamma V_{ub} ^{-2}$ on marching threshold, using 500 curves per threshold	76
7.16	Effect of varying the number of curves per resample on $\Gamma V_{ub} ^{-2}$ for $B \to \pi \ell \nu$ (left) and $B_s \to K \ell \nu$ (right)	77
7.17	V_{ub} vs χ^2 /DoF for all curves	78
	Differential decay rate of all curve pairs, with opacity scaling with the	, (
	relative likelihood, alongside binned experimental results	80
7.19	Bayesian posterior distributions of V_{uh} for various experimental datasets.	81

LIST OF FIGURES ix

7.20	χ^2 minimisation to extract V_{ub} for $B_s \to K\ell\nu$ over a sample of 1760 curves, using the LHCb experimental results [76]
8.1	Differential decay rate divided by $ V_{ub} ^2$ for $B \to \pi \mu \nu_{\mu}$ using Z-fit (left) and DM curve (right) methods
8.2	Differential decay rate divided by $ V_{ub} ^2$ for $B_s \to K \mu \nu_{\mu}$ using Z-fit (left) and DM curve (right) methods
8.3	Differential decay rate divided by $ V_{ub} ^2$ for $B \to \pi \tau \nu_{\tau}$ using Z-fit (left) and DM curve (right) methods
8.4	Differential decay rate divided by $ V_{ub} ^2$ for $B_s \to K\tau\nu_{\tau}$ using Z-fit (left) and DM curve (right) methods
8.5	Forward-backward asymmetry for $B \to \pi \mu \nu_{\mu}$ using Z-fit (left) and DM curve (right) methods
8.6	Forward-backward asymmetry for $B_s \to K \mu \nu_{\mu}$ using Z-fit (left) and DM curve (right) methods
8.7	Forward-backward asymmetry for $B \to \pi \tau \nu_{\tau}$ using Z-fit (left) and DM curve (right) methods
8.8	Forward-backward asymmetry for $B_s \to K\tau\nu_{\tau}$ using Z-fit (left) and DM curve (right) methods
8.9	Normalized forward-backward asymmetry for $B \to \pi \mu \nu_{\mu}$ using Z-fit (left) and DM curve (right) methods
8.10	Normalized forward-backward asymmetry for $B_s \to K\mu\nu_\mu$ using Z-fit (left) and DM curve (right) methods
8.11	Normalized forward-backward asymmetry for $B \to \pi \tau \nu_{\tau}$ using Z-fit (left) and DM curve (right) methods
8.12	Normalized forward-backward asymmetry for $B_s \to K\tau\nu_{\tau}$ using Z-fit (left) and DM curve (right) methods
Арр	endix A.1 Differential decay rate divided by $ V_{ub} ^2$ for $B_s \to K \mu \nu_{\mu}$ and $B \to \pi \mu \nu_{\mu}$ from the 2015 paper (left) and central value curve reconstruction (right)
Арр	endix A.2 Differential decay rate divided by $ V_{ub} ^2$ for $B_s \to K\tau\nu_{\tau}$ and $B \to \pi\tau\nu_{\tau}$ from the 2015 paper (left) and central value curve reconstruction (right)
App	endix A.3 Forward-backward asymmetry for $B_s \to K \mu \nu_{\mu}$ from the 2015 paper (left) and central value curve reconstruction (right).
App	endix A.4 Forward-backward asymmetry for $B_s \to K\tau\nu_{\tau}$ from the 2015 paper (left) and central value curve reconstruction (right)
App	endix A.5 Normalized forward-backward asymmetry for $B \to \pi \tau \nu_{\tau}$ and $B_s \to K \tau \nu_{\tau}$ from the 2015 paper (left) and central value curve reconstruc-
	tion (right)

List of Tables

4.1	Synthetic data points for f_+ and f_0 at $q_1^2 = 19.15 GeV^2$, $q_2^2 = 23.65 GeV^2$ and $q_3^2 = 26.40 GeV^2$	29
4.2	Statistical correlation matrix for f_+ and f_0 at $q_1^2 = 19.15 GeV^2$, $q_2^2 = 23.65 GeV^2$ and $q_3^2 = 26.40 GeV^2$	29
4.3	Systematic correlation matrix for f_+ and f_0 at $q_1^2 = 19.15 GeV^2$, $q_2^2 = 23.65 GeV^2$ and $q_3^2 = 26.40 GeV^2$	30
6.1	$\chi^2/(\text{d.o.f.})$ and P-value for $B_s \to K\ell\nu$ and $B \to \pi\ell\nu$ fit without respecting the unitarity constraint.	40
6.2	The V_{ub} , χ^2 /d.o.f., and P-values for each experiment and the combined fits	52
6.3	V_{ub} calculated for low and high range experimental results from LHCb[66], alongside the weighted mean value. Lattice form factor results used are from the RBC/UKQCD collaboration[88]	53
7.1	Means and uncertainties for the approach looking at only the top and bottom of the overlap region and when finding the minimum and maximum using the optimiser routine	64
7.2	Comparison of the single decay and 2-decay DM methods for 2000 independent bootstrap events. The "% Improvement" is defined as the amount the standard deviation has decreased using the 2 Decay method compared to the single decay result.	66
7.3	V_{ub} results for $B \to \pi \ell \nu$ from different experiments	78
7.4	V_{ub} results for $B \to \pi \ell \nu$ for different experimental datasets using the posterior distribution[62, 65, 63, 68]	79
8.1	Various phenomenological quantities calculated using the Z-fit method (with 10000 sets of coefficients) and the DM curves method (1760 curve pairs)	84
9.1	V_{ub} results for $B \to \pi \ell \nu$ and $B_s \to K \ell \nu$ for different experimental datasets using Z-Fit and DM Curves	91
Арр	pendix A.1 Comparison of RBC/UKQCD $B \to \pi \ell \nu$ phenomenological quantities and the reconstructed values from the central values of the corresponding BCL coefficients	95

Declaration of Authorship

I declare that this thesis and the work presented in it is my own and has been generated by me as the result of my own original research.

I confirm that:

- 1. This work was done wholly or mainly while in candidature for a research degree at this University;
- 2. Where any part of this thesis has previously been submitted for a degree or any other qualification at this University or any other institution, this has been clearly stated;
- 3. Where I have consulted the published work of others, this is always clearly attributed;
- 4. Where I have quoted from the work of others, the source is always given. With the exception of such quotations, this thesis is entirely my own work;
- 5. I have acknowledged all main sources of help;
- 6. Where the thesis is based on work done by myself jointly with others, I have made clear exactly what was done by others and what I have contributed myself;
- 7. None of this work has been published before submission

Signed:	Date:

Acknowledgements

I would firstly like to thank my supervisor, Prof. Jonathan Flynn, for all of his help, patience and guidance throughout my time at Southampton. He has always made himself available to answer my questions and has provided an immense amount of knowledge and insight.

Secondly, I would like to thank everyone I have worked within the lattice group at the University of Southampton, in particular Nikolai Husung, for his assistance and ideas, and Prof. Andreas Jüttner who provided many helpful insights and suggestions.

I thank Toby Peterken for his many discussions with me about physics and academia over the last 8 years, and Jack Arthur for helping me become a better programmer.

Finally, I am forever grateful for the support and guidance from my mum throughout my academic journey. I could not be where I am today without her.

Chapter 1

Introduction

The Standard Model (SM) of particle physics describes all known fundamental particles and their interactions through 3 of the 4 known fundamental forces (Strong, Weak and Electromagnetic). It has been a very successful theory and has made many experimental predictions, such as the existence of the top quark, tau neutrino and Higgs boson.

Despite its many successful predictions, there exist several tensions between the theoretical predictions of the SM and experimental measurements (some examples being the muon anomalous magnetic moment [73] and inclusive vs exclusive measurements of V_{ub} [69]). Additionally, the Standard Model, as originally written, does not allow neutrinos to have mass.

Beyond this, we know the Standard Model is not a complete theory of all physics as it does not describe the fourth fundamental force, Gravity. There is then a need for more precise theoretical predictions to help guide us towards a theory beyond the Standard Model.

A common place to look for new physics is in the decays of hadrons containing heavy quarks, for which many decay channels are possible. The top quark decays too quickly, making the decays of hadrons containing bottom quarks of interest. Exclusive semileptonic decays such as $B \to \pi \ell \nu$ and $B_s \to K \ell \nu$ occur at tree level in the standard model and can be used to determine the strength of quark flavour changes, in this case through the Cabibbo–Kobayashi–Maskawa (CKM) matrix [17, 29] element V_{ub} . Rare B meson decays, such as rare flavour-changing neutral current decays like $B \to K \ell^+ \ell^-$ are suppressed in the Standard Model, possibly making new physics contributions easier to see (however, these will not be the focus of this work).

Computing SM predictions for decays typically boils down to computing matrix elements of quark-level operators between hadronic states like $B_{(s)}$ mesons and lighter mesons. Since the strong interaction is strong at low energy scales, this is a

non-perturbative problem. For a decay matrix element, Lorentz and other relevant symmetries can be used to express the matrix element in terms of a number of 'form factors' which are then the non-perturbative quantities to be computed.

Lattice QCD is a first-principles systematically improvable method for computing masses and matrix elements controlled by the strong interaction, and hence for computing form factors. It then is possible to compute, say, a decay rate up to factors containing SM parameters like CKM matrix elements. Comparing these results with experimental decay information allows the CKM matrix elements to be determined.

Another source of theoretical predictions are called sum rules, which rely on the perturbative nature of QCD over very short distances, and extrapolate to the regime of the interactions of interest [51]. These rely heavily on the Operator Product Expansion (OPE) which allows for perturbative calculations. In comparison to lattice QCD, these methods have additional assumptions, and results from sum rules will not be considered in this work.

Heavy-to-light $B \to \pi \ell \nu$ and $B_s \to K \ell \nu$ decays allow the determination of the modulus of the CKM matrix element, V_{ub} , controlling the strength of charged-current $b \to u$ transitions in the SM. Lattice simulations of these decays work best in the low-recoil, high q^2 (where q is the 4-momentum of the outgoing lepton pair) region of the physical phase space. Because of this, we rely on extrapolation to compare theory predictions using lattice QCD to experimental results over all the allowed q^2 range.

Part of this work concerns methods that exploit unitarity and analyticity constraints stemming from dispersion relations to make model-independent extrapolations of form factors from a (small) number of known points without relying on any parametrised functions for those form factors.

Chapter 2

Standard Model

The Standard Model is built on the gauge group:

$$G = U(1)_Y \times SU(2)_L \times SU(3)_C \tag{2.1}$$

Here *C* denotes colour, which underpins the strong nuclear force. *Y* and *L* denote the hypercharge and the left-handed weak isospin sectors of electroweak interactions. The following sections describe some core aspects of the Standard Model, as well as Lattice QCD, since we will rely on using Lattice QCD form factor results as our known input information for comparison to experiment.

The theoretical development of the Standard Model was shaped by many Physicists. Yang and Mills formulated the principle of gauge invariance for non-Abelian gauge theories [7], a critical step in describing the strong and weak interactions. Glashow [9, 14], Salam and Ward [10, 20], and Weinberg [21] independently formulated the electroweak theory, unifying the electromagnetic and weak interactions and introducing a mechanism for particle masses through spontaneous symmetry breaking. This mechanism was further developed by Higgs [19], Brout and Englert [18], who proposed the scalar field now known as the Higgs field.

Progress in understanding the strong interaction was driven by Gell-Mann's quark model [13, 27], which incorporated the concept of colour charge to describe the structure of hadrons. The mathematical framework of Quantum Chromodynamics (QCD) was later formalized by Politzer [30], Gross and Wilczek [28], who demonstrated asymptotic freedom, explaining the energy-dependent behaviour of quarks. Together, these developments form the theoretical basis of the Standard Model.

This chapter goes through many of the concepts of the Standard Model. For a more complete introduction, there are many helpful textbooks available, for example

Quantum Field Theory and the Standard Model by Schwartz [71], A Modern Introduction to Quantum Field Theory by Maggoire [57], and An Introduction To Quantum Field Theory by Peskin and Schroeder [45].

2.1 Fundamental Particles

The Standard Model describes 17 fundamental particles and their interactions. Particles with spin $\frac{1}{2}$, called fermions, are the matter content of the Standard Model. Particles with integer spins, bosons, mediate the three forces (electromagnetic, weak and strong).

Fermionic fields anti-commute, resulting in the Pauli exclusion principle, as two identical fermions cannot occupy the same state. Fermions in the SM are divided into two categories, quarks and leptons, each with three generations. Each fermion also has a corresponding anti-particle with opposite quantum numbers.

Quarks interact with all three SM fundamental forces; they have electric charge (up-type quarks and down-type quarks have charges of $+\frac{2}{3}$ and $-\frac{1}{3}$, respectively, in units of e), and colour-charge: Quarks transform in the fundamental, 3-dimensional, representation of SU(3) and hence are commonly described as coming in 3 colours, red, green and blue.

Each generation in the SM contains a charged lepton, e, μ , and τ , plus a corresponding neutral neutrino. Leptons do not feel the strong force and so the electrically neutral neutrinos interact only weakly.

The bosons consist of gluons, g, (of which there are 8 types, each carrying a colour and anti-colour charge), the photon, γ mediates the electromagnetic force and W^{\pm} and Z^0 bosons which mediate the weak force. Additionally, the Higgs boson is the fundamental particle associated with the Higgs field, which is responsible for giving particles their intrinsic masses.

2.2 Symmetries

Symmetries play a very important role in field theories. These are transformations that leave the Lagrangian unchanged. These can be discrete symmetries, such as C, P and T (representing charge, parity and time reversal, respectively), or continuous symmetries such as Lorentz boosts and gauge symmetries. According to Noether's theorem, continuous symmetries are intimately linked to conserved quantities; for example, invariance under time translations corresponds to the conservation of energy [2].

2.2. Symmetries 5

Standard Model of Elementary Particles

three generations of matter interactions / force carriers (bosons) Ш Ш ≈2.16 MeV/d ≈172.57 GeV/c ≈125.2 GeV/c² ≈1.273 GeV/c 2/3 1/2 2/3 1/2 H C t g gluon higgs charm up top ≈4.7 MeV/c² ≈93.5 MeV/c2 ≈4.183 GeV/c **DUARKS** d S b γ down strange bottom photon ≈105.66 MeV/c 1.77693 GeV/c² е μ Z τ Z boson electron muon tau **EPTONS** <0.8 eV/c 80.3692 GeV/ W $\nu_{\rm e}$ ν_{μ} ν_{τ} electron muon W boson neutrino

FIGURE 2.1: Standard model of elementary particles [70, 91]

Symmetries can also be classified as being local or global; local symmetries correspond to transformations which can be different at different space-time points, whereas global symmetries come from transformations that are applied uniformly to all points. Gauge symmetries are local symmetries characterized by transformations that can vary independently at each spacetime point while preserving the invariance of the Lagrangian, and thereby necessitating the introduction of gauge fields. These symmetries are fundamental to the structure of the Standard Model, where each interaction is governed by the gauge group associated with the underlying field theory.

Symmetry breaking occurs when the Lagrangian density after a transformation is not equivalent to that beforehand. Explicit symmetry breaking occurs when

$$\delta \mathcal{L} \equiv \mathcal{L}' - \mathcal{L} \tag{2.2}$$

is non-zero. Spontaneous symmetry breaking, on the other hand, occurs when the transformation leaves the Lagrangian density unchanged, but the resulting ground state is not invariant under the symmetry. Spontaneous breaking of a continuous symmetry leads to the appearance of a massless Goldstone boson [15], but in the case of a gauge symmetry, the Goldstone boson is 'eaten', giving mass to the corresponding gauge field [19].

2.3 Electroweak Interactions

The electroweak interaction is described by the $U(1)_Y \times SU(2)_L$ symmetry in the Standard Model and combines the electromagnetic and weak interactions. The electromagnetic force, mediated by the massless photon, describes phenomena such as the interactions of charged particles with electric and magnetic fields.

The weak interaction is a short-range force and is responsible for processes such as flavour-changing decays and neutral current interactions involving the Z^0 boson. These interactions are mediated by the W^\pm and Z^0 bosons, which acquire mass via spontaneous symmetry breaking. Unlike the electromagnetic force, the weak interaction violates parity symmetry. This was first demonstrated by Wu [8], who showed that beta decay rates are asymmetrically distributed with respect to the spin direction of decaying nuclei. This parity violation arises because the weak force couples differently to left-handed and right-handed particles.

The relative strengths of the electromagnetic and weak interactions differ significantly. At low energies, the weak interaction is much weaker than the electromagnetic force, primarily due to the large masses of the W^{\pm} and Z^0 bosons. How these interactions come from the underlying Lagrangian and the mechanism of symmetry breaking will be explored in this section.

The gauge fields associated to the electroweak interaction, W_{μ}^{a} (a=1,2,3) and B_{μ} , give rise to the electroweak bosons through the process of electroweak spontaneous symmetry breaking [71, 45, 57]. After this symmetry breaking, the residual $U(1)_{\rm em}$ symmetry corresponds to the electromagnetic interactions described by quantum electrodynamics (QED), an Abelian gauge theory [4, 5].

2.3.1 The Electroweak Lagrangian

A key observed phenomenon of the electroweak interaction is that it beaks parity, to see how this works we first introduce the right and left-handed parts of the Fermion field, ψ , as

$$\psi_L = P_L \psi = \frac{1 - \gamma_5}{2} \psi; \quad \psi_R = P_R \psi = \frac{1 + \gamma_5}{2} \psi,$$
 (2.3)

where we have used the chiral projectors P_R and P_L , and

$$\gamma^5 \equiv i\gamma^0 \gamma^1 \gamma^2 \gamma^3 = \begin{pmatrix} 0 & 0 & 1 & 0 \\ 0 & 0 & 0 & 1 \\ 1 & 0 & 0 & 0 \\ 0 & 1 & 0 & 0 \end{pmatrix}, \tag{2.4}$$

where γ^i are the gamma matrices (I have used the ordinary/standard representation) [57].

 $SU(2)_L$ acts only on left-handed (LH) fields, and the W^\pm bosons are linear combinations of the $W^{1,2}$ components of the $SU(2)_L$ gauge field. SU(2) is the group of 2×2 unitary matrices with determinant 1, and the Pauli matrices are the basis of its Lie algebra.

Part of the specification of the SM is that the LH quarks and leptons are doublets under $SU(2)_L$ (the Lagrangian is invariant under SU(2) matrix transformations):

$$L_i = \begin{pmatrix} \nu_{iL} \\ \ell_{iL} \end{pmatrix} \tag{2.5}$$

This is the doublet for the i^{th} generation of charged and neutral leptons and

$$Q_i = \begin{pmatrix} u_{iL} \\ d_{iL} \end{pmatrix} \tag{2.6}$$

is the doublet for the i^{th} generation of up-type and down-type quarks.

The B_{μ} gauge field couples to both left and right-handed fermions (with gauge coupling, g') according to their weak hypercharge, Y, which is

$$Y = Q - I_3, \tag{2.7}$$

where I_3 is the third generator of $SU(2)_L$ (with eigenvalue T_L^3) and Q is electric charge.

The top and bottom components of these doublets have weak isospin of $+\frac{1}{2}$ and $-\frac{1}{2}$, respectively, and leptons/quarks have hypercharges $Y_L^l = -1$ and $Y_L^q = -1$, respectively. The right-handed components are SU(2) singlets (i.e. they don't transform under SU(2) but do transform under U(1)):

$$l_{-} = (e_R, \mu_R, \tau_R),$$
 (2.8)

$$q_{+} = (u_{R}, c_{R}, t_{R}),$$
 (2.9)

$$q_{-} = (d_R, s_R, b_R). (2.10)$$

The right-handed leptons/quarks have hypercharges $Y_R^l = -2$, $Y_{R+}^q = +\frac{4}{3}$ and $Y_{R-}^q = -\frac{2}{3}$.

The electroweak Lagrangian densities for quarks and leptons are given by:

$$\mathcal{L}_{EW}^{l} = \sum_{i=1}^{3} \left(i \bar{L}_{i} \gamma^{\mu} D_{\mu}^{L} L_{i} + i \bar{l}_{i-} \gamma^{\mu} D_{\mu}^{R} l_{i-} \right)$$
 (2.11)

$$\mathcal{L}_{EW}^{q} = \sum_{i=1}^{3} \left(i \bar{Q}_{i} \gamma^{\mu} D_{\mu}^{L} Q_{i} + i \bar{q}_{i+} \gamma^{\mu} D_{\mu}^{R} q_{i+} + i \bar{q}_{i-} \gamma^{\mu} D_{\mu}^{R} q_{i-} \right)$$
(2.12)

Here, i sums over the three generations. For charged leptons, these generations are e, μ , and τ , and for neutrinos, they are the corresponding neutrino types. For quarks, the generations are up/down, charm/strange, and top/bottom, with + or - indicating up-like or down-like quarks, respectively.

The absence of l_{i+} in \mathcal{L}^l_{EW} reflects the fact that neutrinos are only left-handed in the Standard Model. As a result, they are massless in this framework, as the lack of a right-handed component prevents a Dirac mass term for neutrinos. The observation of neutrino oscillations is the strongest evidence for physics beyond the Standard Model, as this confirms that neutrinos have mass [52].

The covariant derivatives are given by

$$D_{\mu}^{L} = \partial_{\mu} - ig \frac{1}{2} \sigma^{a} W_{\mu}^{a}(x) - ig' \frac{Y}{2} B_{\mu}(x), \qquad (2.13)$$

$$D_{\mu}^{R} = \partial_{\mu} - ig' \frac{Y}{2} B_{\mu}(x). \tag{2.14}$$

Here, σ^a are the Pauli matrices. The Lagrangian density of the electroweak gauge terms is

$$\mathcal{L}_{EW,G} = -\frac{1}{4} W^{a}_{\mu\nu} W^{a\mu\nu} - \frac{1}{4} B_{\mu\nu} B^{\mu\nu}, \qquad (2.15)$$

where we have defined field strength tensors

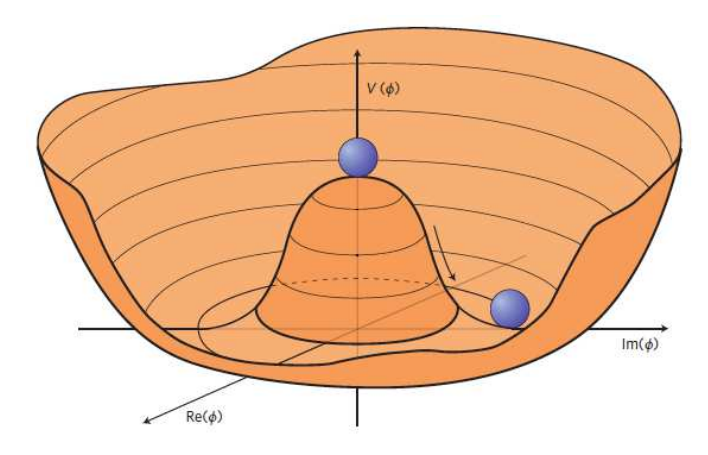


FIGURE 2.2: An illustration of the Higgs potential [67].

$$W_{\mu\nu}^{i} = \partial_{\mu}W_{\nu}^{i} - \partial_{\nu}W_{\mu}^{i} - g\epsilon_{ijk}W_{\mu}^{j}W_{\nu}^{k}, \qquad (2.16)$$

$$B_{\mu\nu} = \partial_{\mu}B_{\nu} - \partial_{\nu}B_{\mu}. \tag{2.17}$$

2.3.2 Spontaneous Symmetry Breaking & the Higgs Mechanism

Symmetry requires that the electroweak gauge bosons, W_{μ}^{a} (a=1,2,3) and B_{μ} , be massless in the unbroken $SU(2)_{L} \times U(1)_{Y}$ theory. However, the weak interaction is observed to be short-ranged, indicating that the mediating bosons must acquire mass through some mechanism. This occurs via the Higgs mechanism [19], where spontaneous symmetry breaking of $SU(2)_{L} \times U(1)_{Y}$ to $U(1)_{EM}$ results in the masses of the W^{\pm} and Z bosons while leaving the photon massless. The Higgs potential, often illustrated as a "Mexican hat" potential (shown in Figure 2.2), causes the Higgs field to acquire a non-zero vacuum expectation value. This vacuum expectation value (VEV) gives mass to the electroweak gauge bosons through their interactions with the Higgs field and to fermions through Yukawa couplings. This section outlines this spontaneous symmetry breaking and the Higgs mechanism.

The Higgs field is a complex scalar doublet, and its Lagrangian is given by

$$\mathcal{L}_{\text{Higgs}} = D^{\mu} \phi^{\dagger} D_{\mu} \phi - V(\phi), \tag{2.18}$$

where

$$\phi(x) = \begin{pmatrix} \phi_{+}(x) \\ \phi_{0}(x) \end{pmatrix} = \frac{1}{\sqrt{2}} \begin{pmatrix} \phi_{1}(x) + i\phi_{2}(x) \\ \phi_{3}(x) + i\phi_{4}(x) \end{pmatrix}, \tag{2.19}$$

and the Higgs potential, $V(\phi)$, is

$$V(\phi) = -\mu^2 \left(\sum_{i=1}^4 \phi_i^2 \right) + \lambda \left(\sum_{i=1}^4 \phi_i^2 \right)^2.$$
 (2.20)

This potential has an infinite number of degenerate states with minimum energy for values of ϕ satisfying

$$|\phi|^2 = \frac{\mu^2}{4\lambda} \equiv \frac{v^2}{2},\tag{2.21}$$

where we have defined the vacuum energy as $v^2 = \frac{\mu^2}{2\lambda}$.

Substituting the expression for the Higgs doublet gives:

$$\phi_1^2 + \phi_2^2 + \phi_3^2 + \phi_4^2 = v^2 \tag{2.22}$$

This equation defines a 3-dimensional sphere. We may reparametrize the Higgs doublet, choosing θ_1^2 , θ_2^2 , and θ_3^2 to be three real fields tangent to the surface of the sphere and a real field H(x) which is normal to the surface. The Higgs doublet can now be written as:

$$\phi(x) = \frac{1}{\sqrt{2}} e^{i\frac{1}{2v}\sigma^a \theta^a(x)} \begin{pmatrix} 0\\ v + H(x) \end{pmatrix}$$
 (2.23)

Here the fields θ_i correspond to three Goldstone bosons[11, 15] and H(x), to the Higgs. We may now use a gauge transformation to the unitary gauge, setting θ_i to zero:

$$\phi(x) = \frac{1}{\sqrt{2}} \begin{pmatrix} 0\\ v + H(x) \end{pmatrix} \tag{2.24}$$

Substituting this expression for ϕ into the kinetic part of the Higgs Lagrangian, and restricting our attention only to the parts which couple to the vacuum expectation value, v:

$$(D_{\mu}\phi)^{\dagger}(D^{\mu}\phi) \supset \frac{v^2}{8} \left[g^2((W^1)^2 + (W^2)^2) + (g'B_{\mu} - gW^3)^2 \right]. \tag{2.25}$$

Our goal is to rewrite these gauge fields in terms of physical fields. We start by defining

$$W^{\pm} = \frac{1}{\sqrt{2}} \left(W^1 \mp i W^2 \right). \tag{2.26}$$

This allows us to rewrite the first term in 2.25. We now look at the second term:

$$(g'B_{\mu} - gW_3)^2 = g^2W_3^2 - 2B_{\mu}W_3 + g'^2B_{\mu}^2$$
 (2.27)

$$= \begin{pmatrix} W_3 & B_{\mu} \end{pmatrix} \begin{pmatrix} g^2 & -gg' \\ -gg' & g'^2 \end{pmatrix} \begin{pmatrix} W_3 \\ B_{\mu} \end{pmatrix}$$
 (2.28)

We diagonalize our coupling matrix:

$$\begin{pmatrix} g^2 & -gg' \\ -gg' & g'^2 \end{pmatrix} = UDU^{-1}, \tag{2.29}$$

where *U* and *D* are

$$U = \frac{1}{\sqrt{g^2 + g'^2}} \begin{pmatrix} g' & g \\ g & -g' \end{pmatrix}, \quad D = \begin{pmatrix} 0 & 0 \\ 0 & g^2 + g'^2 \end{pmatrix}. \tag{2.30}$$

Now we absorb the unitary rotation matrix into the redefined fields:

$$\begin{pmatrix} W_3 & B_{\mu} \end{pmatrix} U D U^{-1} \begin{pmatrix} W_3 \\ B_{\mu} \end{pmatrix} = \begin{pmatrix} A_{\mu} & Z_{\mu} \end{pmatrix} \begin{pmatrix} 0 & 0 \\ 0 & g^2 + g'^2 \end{pmatrix} \begin{pmatrix} A_{\mu} & Z_{\mu} \end{pmatrix}^T \tag{2.31}$$

Our new physical fields A_{μ} and Z_{μ} are given by

$$A_{\mu} = \frac{1}{\sqrt{g^2 + g'^2}} (g'W_3 + gB_{\mu}),$$

$$Z_{\mu} = \frac{1}{\sqrt{g^2 + g'^2}} (gW_3 - g'B_{\mu}).$$
(2.32)

We can now rewrite 2.25 in terms of the physical fields:

$$(D^{\mu}\phi)^{\dagger}(D_{\mu}\phi) \supset \frac{v^2}{8} \left[g^2 W^{+2} + g^2 W^{-2} + (g^2 + g'^2) Z_{\mu}^2 + 0 \cdot A_{\mu}^2 \right]$$
 (2.33)

We can now see that after spontaneous symmetry breaking, we have 1 massless Goldstone boson, the photon, and 3 massive Goldstone bosons, W^{\pm} and Z, with masses

$$m_{W^{\pm}} = \frac{1}{2}vg, \quad m_Z = \frac{v}{2}\sqrt{g^2 + g'^2}.$$
 (2.34)

2.3.3 Yukawa Interactions

The Standard Model is a chiral gauge theory. As left and right-handed fermions do not transform the same way under gauge symmetry, it is not possible to write gauge invariant mass terms for fermions.

The Yukawa Lagrangian for the three generations of leptons is given by:

$$\mathcal{L}_{Y}^{l} = -\sqrt{2} \sum_{i,j=1}^{3} \left[\bar{L}_{i-} \phi m_{ij} l_{j-} + \bar{l}_{j-} m_{ji}^{*} \phi^{\dagger} L_{i-} \right]$$
 (2.35)

Here L and l are the left and right-handed lepton fields, and m_{ij} is the 3x3 matrix containing the Yukawa coupling constants that determine the strength of interaction between the Higgs field and the lepton fields.

Following our unitarity gauge transformation, our Higgs doublet, ϕ , is given by 2.24. The fields in our Lagrangian are represented in the electroweak basis. We wish to find the mass eigenstates, so we diagonalise our matrix, m_{ij} :

$$m_{ij} = D_{ik}^{(1)} \Lambda_{kl} D_{lj}^{(2)} (2.36)$$

Here $\Lambda = \text{diag}(\lambda_e, \lambda_\mu, \lambda_\tau)$, a diagonal matrix of the Yukawa couplings. We absorb these rotation matrices into our lepton fields:

$$L'_{i-} = D_{ij}^{(L)} L_{j-} (2.37)$$

$$l'_{i-} = D_{ii}^{(R)} l_{j-} (2.38)$$

The masses of the leptons are given by:

$$m_e = \lambda_e v, \quad m_u = \lambda_u v, \quad m_\tau = \lambda_\tau v$$
 (2.39)

For quarks, the procedure is similar, with the added complexity of there being up and down-types; the Yukawa Lagrangian for quarks is:

$$\mathcal{L}_{Y}^{q} = -\sqrt{2} \sum_{i,j=1}^{3} \left[\bar{Q}_{i} \phi m_{ij}^{-} q_{j-} + \bar{q}_{j-} m_{ji}^{-*} \phi^{\dagger} Q_{i} + \bar{Q}_{i} \tilde{\phi} m_{ij}^{+} q_{j+} + \bar{q}_{j+} m_{ji}^{+*} \tilde{\phi}^{\dagger} Q_{i} \right]$$
(2.40)

Where, after our reparametrization and transformation into the unitary gauge, $\tilde{\phi}$ is defined to be

$$\tilde{\phi}_i(x) = \begin{pmatrix} v + H(x) \\ 0 \end{pmatrix}. \tag{2.41}$$

 $(\tilde{\phi}=i\sigma^2\phi^*)$ before going to the unitary gauge). $\tilde{\phi}$ is an SU(2) doublet with the opposite hypercharge to ϕ . This construction exploits a property of SU(2): the fundamental representation (doublets) is pseudoreal. Pseudoreality means that the fundamental representation is equivalent to its complex conjugate under a similarity transformation, a feature specific to SU(2). The operator $i\sigma^2$ is used to define $\tilde{\phi}$ in a way that preserves the SU(2) transformation properties while reversing the hypercharge.

We wish to find the mass eigenstates, so we diagonalize our matrices m_{ij}^{\pm} , and set $\tilde{\phi}$ to its VEV:

$$m_{ij}^{\pm} = U_{il}^{(R)\pm\dagger} \Lambda_{lm}^{\pm} U_{mj}^{(L)\pm}$$
 (2.42)

Our unitary rotation matrices, $U^{(L)\pm}$ and $U^{(R)\pm}$ are absorbed into our quark fields:

$$Q'_{i\pm} = U^{(L)\pm}_{ij} Q_{j\pm} \tag{2.43}$$

$$q'_{i\pm} = U_{ij}^{(R)\pm} q_{j\pm} \tag{2.44}$$

2.3.4 CKM Matrix

Following our transformation into the mass basis using the unitary matrices, $U^{(L)\pm}$ and $U^{(R)\pm}$, we must now see how this transformation changes the interaction terms between quarks and electroweak bosons in our electroweak Lagrangian. After the spontaneous symmetry breaking, these terms are:

$$\mathcal{L}_{q-EWb} = \frac{g}{\sqrt{2}} \sum_{i=1}^{3} \left(J_{+i}^{\mu} W_{\mu}^{-} + J_{-i}^{\mu} W_{\mu}^{+} \right)$$
 (2.45)

Here, J_{\pm}^{μ} are the left-handed quark currents given by

$$J_{+}^{\mu} = \bar{Q}_{-}^{\prime} \gamma^{\mu} Q_{+} = \bar{Q}_{-} U^{(L)-\dagger} \gamma^{\mu} U^{(L)+} Q_{+}^{\prime}$$
 (2.46)

$$J_{-}^{\mu} = \bar{Q}'_{+} \gamma^{\mu} Q_{-} = \bar{Q}_{+} U^{(L)+\dagger} \gamma^{\mu} U^{(L)-} Q'_{-}$$
 (2.47)

We define the Cabibbo-Kobayashi-Maskawa (CKM) matrix, V_{CKM} , using this, as

$$V_{CKM} = U^{(L)+\dagger}U^{(L)-} = \begin{pmatrix} V_{ud} & V_{us} & V_{ub} \\ V_{cd} & V_{cs} & V_{cb} \\ V_{td} & V_{ts} & V_{tb} \end{pmatrix}.$$
(2.48)

The CKM matrix gives the mixing of up and down-type quarks in the Standard Model[17, 29]. This matrix is unitary by construction. Because of this, there are only four degrees of freedom in the CKM matrix (three mixing angles and a CP-violating phase). The matrix arises because we need different U matrices to diagonalise the up-type and down-type quark masses, but left-handed up-type and left-handed down-type quarks are in the same SU(2) doublets. It is worth noting that no flavour-changing couplings to the Z boson arise.

A common parametrization for the CKM matrix arises from the following mixing:

$$V_{CKM} = \begin{pmatrix} 1 & 0 & 0 \\ 0 & c_{23} & s_{23} \\ 0 & -s_{23} & c_{23} \end{pmatrix} \begin{pmatrix} c_{13} & 0 & s_{13}e^{-i\phi} \\ 0 & 1 & 0 \\ -s_{13}e^{i\phi} & 0 & c_{13} \end{pmatrix} \begin{pmatrix} c_{12} & s_{12} & 0 \\ -s_{12} & c_{12} & 0 \\ 0 & 0 & 1 \end{pmatrix}$$
(2.49)

$$= \begin{pmatrix} c_{12}c_{13} & s_{12}c_{13} & s_{13}e^{-i\phi} \\ -s_{12}c_{23} - c_{12}s_{23}s_{13}e^{i\phi} & c_{12}c_{23} - s_{12}s_{23}s_{13}e^{i\phi} & s_{23}c_{13} \\ s_{12}s_{23} - c_{12}c_{23}s_{13}e^{i\phi} & -c_{12}s_{23} - s_{12}c_{23}s_{13}e^{i\phi} & c_{23}c_{13} \end{pmatrix}$$
(2.50)

Here, $s_{ij} = sin(\theta_{ij})$ and $c_{ij} = cos(\theta_{ij})$, where θ_{ij} is the mixing angle between generations i and j. ϕ is the CP-violating angle[41].

An alternative parametrization, known as the Wolfenstein parametrization, approximates the CKM matrix by expanding it in terms of a parameter, λ , equal to V_{us} . It makes use of the observed difference in magnitudes between mixing between different generations of quarks[40].

At the time of its origin, two well observed CKM matrix elements were V_{us} and V_{cb} . It was observed V_{cb} is of order λ^2 , so we define a factor, A, such that

$$V_{cb} = A\lambda^2. (2.51)$$

To order λ^2 , the CKM matrix is then

$$V_{CKM} = \begin{pmatrix} 1 - \frac{1}{2}\lambda^2 & \lambda & 0 \\ & & & \\ -\lambda & 1 - \frac{1}{2}\lambda^2 & A\lambda^2 \\ 0 & -A\lambda^2 & 1 \end{pmatrix}$$
 (2.52)

We can now use unitarity to go to order λ^3 :

$$V_{CKM} = \begin{pmatrix} 1 - \frac{1}{2}\lambda^{2} & \lambda & \lambda^{3}A(\rho - i\eta) \\ -\lambda & 1 - \frac{1}{2}\lambda^{2} & \lambda^{2}A \\ \\ \lambda^{3}A(1 - \rho - i\eta) & -\lambda^{2}A & 1 \end{pmatrix}, \tag{2.53}$$

where we have introduced two parameters, ρ and η . In terms of our common parametrization parameters, λ , A, ρ and η are given by:

$$\lambda = s_{12} \tag{2.54}$$

$$A = \frac{s_{23}}{s_{12}^2} \tag{2.55}$$

$$\rho = \mathcal{R}_e \left\{ \frac{s_{13}e^{-i\delta}}{s_{12}s_{23}} \right\} \tag{2.56}$$

$$\eta = -\mathcal{I}_m \left\{ \frac{s_{13} e^{-i\delta}}{s_{12} s_{23}} \right\} \tag{2.57}$$

Wolfenstein introduced the parametrization in Equation 2.53 as an approximation, but it was later realised that you can define

$$V_{us} = \lambda$$
, $V_{cb} = A\lambda^2$, $V_{ub} = A\lambda^3(p - i\eta)$, (2.58)

as exact, and then construct the rest of the CKM matrix by unitarity. You can then expand to any order in λ (this also uses a phase convention that V_{ud} , V_{us} , V_{cs} , V_{cb} and V_{tb} are all real and positive).

Figure 2.3 shows the global constraints on the CKM unitarity triangle in the $(\overline{\rho}, \overline{\eta})$ plane. $\overline{\rho}$ and $\overline{\eta}$ are defined as

$$\overline{\rho} = \rho \left(1 - \frac{\lambda^2}{2} \right), \quad \overline{\eta} = \eta \left(1 - \frac{\lambda^2}{2} \right).$$
 (2.59)

The CKM unitarity triangle plot is constrained by several experimental measurements. The blue band comes from CP violation in decays such as

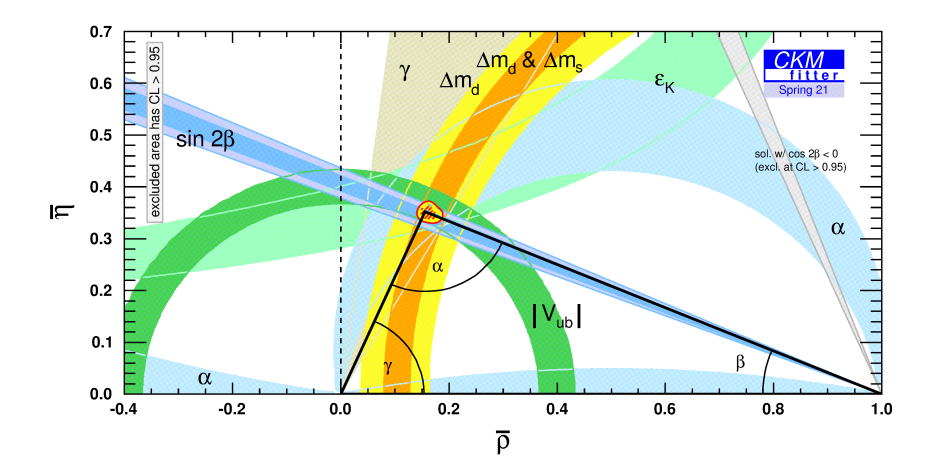


FIGURE 2.3: Global constraints on the CKM unitarity triangle in the $(\overline{\rho}, \overline{\eta})$ plane. The overlapping red ellipse indicates the region allowed at a 95% confidence level. [55]

 $B^0 \to J/\psi \, K_S^0$; the light-blue wedge is based on neutral kaon mixing through the measurement of ε_K ; and the orange/yellow bands reflect the mass differences observed in B_d and B_s meson oscillations. The semileptonic decays analyzed in this work provide a constraint for $|V_{ub}|$, which is shown by the green band.

2.4 Quantum Chromodynamics

Quantum Chromodynamics (QCD) is the theory of the strong force, which describes the interactions of hadronic matter: quarks and gluons. It is a non-abelian SU(3) gauge theory[71, 45, 57]. Quarks are in the fundamental representation of SU(3). Gluons (like all gauge bosons) are in the adjoint, which has dimension equal to the number of generators of the group. For SU(3) this is 8, corresponding to each colour charge-anti-charge combination, each with a gluon field, G^a_μ . The QCD Lagrangian density is given by

$$\mathcal{L}_{QCD} = \sum_{f} \bar{\phi}_f (i\gamma^{\mu} D_{\mu} - m_f) \phi_f - \frac{1}{4} G^a_{\mu\nu} G^{a\mu\nu}$$
 (2.60)

where $G_{\mu\nu}$ is the gluon field strength tensor and ϕ_f represents the quark fields (with f indexing flavours u,d,s,c,b,t). The covariant derivative is defined as

$$D_{\mu} = \partial_{\mu} - ig_s \frac{1}{2} \lambda^a G_{\mu}^a. \tag{2.61}$$

The mass, m_f in Equation 2.60 comes from the Higgs mechanism in the $SU(2) \times U(1)$ sector, and g_S is the strong coupling constant. Analogous to the 2x2 Pauli matrices, we

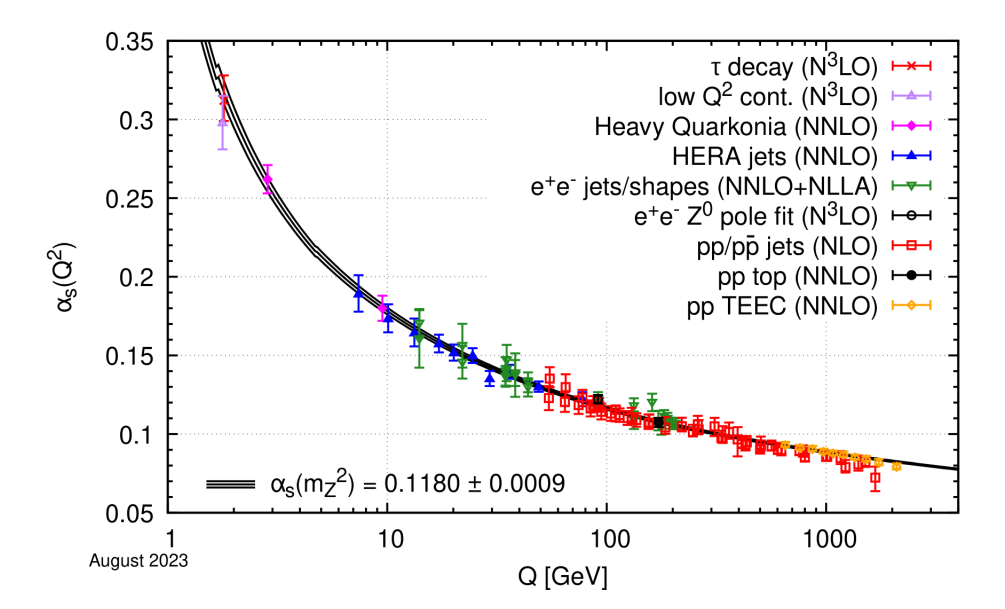


FIGURE 2.4: Running of the strong coupling constant, denoted here as α_S , with energy scale Q [86].

have made use of the 3x3 Gell-Mann matrices[16], λ_i , which are a representation of the generators of the SU(3) symmetry.

$$\lambda_1 = \begin{pmatrix} 0 & 1 & 0 \\ 1 & 0 & 0 \\ 0 & 0 & 0 \end{pmatrix} \quad \lambda_2 = \begin{pmatrix} 0 & -i & 0 \\ i & 0 & 0 \\ 0 & 0 & 0 \end{pmatrix} \quad \lambda_3 = \begin{pmatrix} 1 & 0 & 0 \\ 0 & -1 & 0 \\ 0 & 0 & 0 \end{pmatrix}$$
 (2.62)

$$\lambda_4 = \begin{pmatrix} 0 & 0 & 1 \\ 0 & 0 & 0 \\ 1 & 0 & 0 \end{pmatrix} \quad \lambda_5 = \begin{pmatrix} 0 & 0 & -i \\ 0 & 0 & 0 \\ i & 0 & 0 \end{pmatrix} \quad \lambda_6 = \begin{pmatrix} 0 & 0 & 0 \\ 0 & 0 & 1 \\ 0 & 1 & 0 \end{pmatrix}$$
 (2.63)

$$\lambda_7 = \begin{pmatrix} 0 & 0 & 0 \\ 0 & 0 & -i \\ 0 & i & 0 \end{pmatrix} \lambda_8 = \begin{pmatrix} 1/\sqrt{3} & 0 & 0 \\ 0 & 1/\sqrt{3} & 0 \\ 0 & 0 & -2/\sqrt{3} \end{pmatrix}$$
(2.64)

Due to the nature of the strong coupling, at low energies (below Λ_{QCD}), perturbation theory is not a valid approach. This is because the running of the strong coupling constant, α_s , becomes large at low energies, making perturbative methods ineffective. As a result, non-perturbative techniques must be employed to study Quantum Chromodynamics (QCD). Some of the prominent methods include lattice QCD, sum rules, and the AdS/CFT correspondence, though the latter has not yet been successfully applied to realistic, phenomenologically useful examples. In the high-energy regime, above Λ_{QCD} , QCD exhibits asymptotic freedom, as demonstrated by the behaviour of the Non-Abelian Gauge Theories (NAGTs) in 4D, where the coupling strength decreases at higher energy scales. However, at low energy scales,

the coupling grows stronger, leading to confinement and the breakdown of perturbation theory. In this low-energy regime, we rely on non-perturbative approaches such as lattice QCD to obtain insights into the behaviour of QCD. The form factor information used in this work exclusively comes from lattice QCD, and so I shall very briefly cover the main concepts in the following section.

2.5 Lattice QCD

Lattice QCD provides a systematic framework for studying strong interactions directly from first principles[33, 32, 35, 61]. It discretizes spacetime into a finite-volume grid and reformulates the theory in Euclidean spacetime for numerical tractability. Quarks are positioned at lattice points, while gluons are modelled as link variables connecting the points.

There are many ways to implement this discretization that ensure that the continuum limit $a \to 0$ recovers the QCD Lagrangian. Different lattice formulations of quarks, such as Wilson [31], staggered [34], domain wall [43], and twisted mass [53], can be employed, each with specific advantages and challenges in reproducing the correct chiral continuum behaviour. Discretization effects of order $\mathcal{O}(a^n)$ can be mitigated using techniques such as the Symanzik improvement program [38, 39, 90].

The lattice parameters, including the lattice spacing *a*, volume, and quark masses, must be tuned to match the physical world. This requires extrapolating quark masses to their physical values, often done through chiral extrapolation, to recover the correct behaviour in the continuum limit. As part of this process, the lattice spacing *a* is sent to zero (the continuum limit), and the volume is taken to infinity to remove finite volume effects.

This method is systematically improvable, with accuracy improving as computational power increases, with simulations getting closer to $a \to 0$, $L \to \infty$, and quark masses to their physical values.

An important part of this formulation is the discretization of the gauge fields. In this approach the continuous gauge fields are represented by link variables that lie on the edges between lattice points. These link variables are chosen to be elements of the underlying gauge group and are designed to preserve the gauge invariance of the theory. The discretization of fermions is accomplished by defining quark fields on the lattice sites and choosing an appropriate formulation such as Wilson or staggered fermions.

An important component of the gauge action is the plaquette. This is defined as the product of four link variables that form a square on the lattice. The resulting plaquette

2.5. Lattice QCD

is unitary as each link is a unitary matrix, and it is essential in approximating the gauge field strength in the continuum limit.

2.5.1 Path Integrals

To perform measurements over our discretized spacetime, such as measuring correlation functions, we make use of path integrals. Discretizing spacetime on a finite volume transforms the path integral into an ordinary, albeit extremely high-dimensional, integral. This integral is most efficiently evaluated using importance sampling methods, such as Monte Carlo simulations. To facilitate this, we perform a rotation to Euclidean space, where the factor e^{iS} (from the action S) becomes e^{-S} , making it possible to interpret the integrand as a probability density.

A general n-point correlation function is of the form

$$C_n(x_1, x_2, \dots, x_n) = \langle T\{\mathcal{O}_1(x_1)\mathcal{O}_2(x_2)\dots\mathcal{O}_n(x_n)\}\rangle,$$
 (2.65)

where we have the expectation value of the time ordered product of n operators $\mathcal{O}_i(x_i)$ [45]. I will implicitly assume the time ordering from now on. Our correlation function is then given by the following path integral in Minkowski spacetime:

$$\langle \mathcal{O} \rangle = \frac{1}{Z} \int \mathcal{D}[\Phi] \mathcal{O}e^{iS_M[\Phi]}$$
 (2.66)

Here, Φ , represents all fermion and gauge fields. Z is our partition function:

$$Z = \int \mathcal{D}[\Phi]e^{iS_M[\Phi]} \tag{2.67}$$

To calculate these on the lattice, we now modify our path integral expression as follows:

- We perform a Wick rotation to transform from Minkowski spacetime to Euclidean spacetime. This transforms our action as $iS_M \rightarrow -S$ [6, 33, 32].
- Discretize our spacetime into a lattice of points with a spacing, *a*, and volume L³ × T. We also must ensure the correct action is recovered in the continuum limit (*a* → 0)[45].

Our path integral on the lattice is now of the form

$$\langle \mathcal{O} \rangle = \frac{1}{Z} \int \mathcal{D}[\Phi] \mathcal{O}e^{-S[\Phi]}.$$
 (2.68)

Measurements on the lattice are performed over variations of lattice spacing, volumes and quark masses where possible. Results are extrapolated to the chiral continuum limit, where the lattice spacing, $a \to 0$, the volume, $L^3 \to \infty$, and the quark masses are taken to their physical values.

2.5.2 Importance sampling

The Euclidean path integral for an observable, O, is given in Equation 2.68. This is a weighted average of all possible quark/gluon field configurations according to $e^{-S[\Phi]}$ varies enormously, so evaluating this integral numerically is best done through sampling the tiny region which contributes significantly [58].

This is importance sampling, which is a variance reduction method (compared to say, sampling the space uniformly), meaning stochastic estimates of the integral of interest have a reduced standard error.

Importance sampling focuses computation time on the most highly contributing configurations. It does this through a Monte Carlo procedure, where all sampled configurations are given equal weighting, but the probability of being sampled is proportional to e^{-S} [56].

2.6 Semileptonic Decays

The work in this thesis focuses on pseudoscalar-to-pseudoscalar semileptonic decays, namely $B \to \pi \ell \nu$ (the Feynman diagram for this is given in 2.5) and $B_s \to K \ell \nu$ (however much of the work applies to other exclusive semileptonic decays, such as $B \to D \ell \nu$, $D \to K \ell \nu$ and those with vector final states, such as $B \to D^* \ell \nu$, $D \to K^* \ell \nu$).

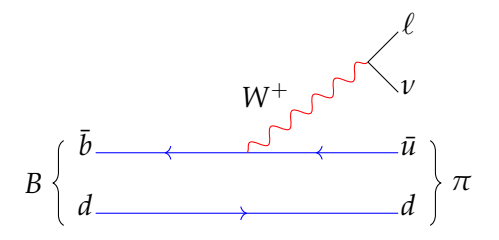


FIGURE 2.5: Feynman diagram for $B \to \pi \ell \nu$.

We can decompose our matrix element, $\langle P(k) | \mathcal{V}^{\mu}(0) | B_s(p) \rangle$, in terms of the two form factors, f_- and f_+ . P and B_s represent pseudoscalar mesons with 4-momenta k and p,

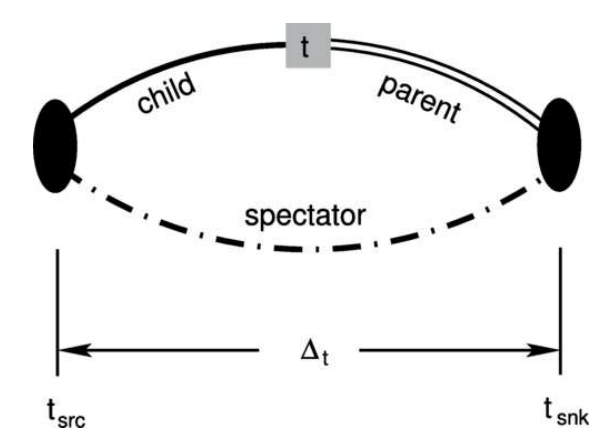


FIGURE 2.6: Sketch of a generic three-point function. The spectator quark (dot-dashed line) originates from time slice t_{src} and propagates forward to time slice t_{snk} where we create a point sink and turn it into a sequential source for the parent quark (double line) propagating backward. This sequential propagator is contracted with the child light quark (solid line) also originating from t_{src} . [88]

and masses M_P and $M_{B_{(S)}}$, respectively. As our matrix element has a Lorentz index, μ , it must be constructed from available vectors with the same index:

$$\langle P(k)|\mathcal{V}^{\mu}(0)|B_s(p)\rangle = f_+(q^2)p^{\mu} + f_-(q^2)q^{\mu}$$
 (2.69)

Here $q^{\mu} = p^{\mu} - k^{\mu}$, the 4-momenum transferred to the outgoing lepton-pair. It is useful to express Equation 2.69 in terms of the form factors f_0 and f_+ , as these form factors relate to the transition amplitude with the exchange of a scalar (0^+) and vector (1^-) boson in the t-channel, respectively [77]. f_0 is defined as

$$f_0(q^2) = f_+(q^2) + \frac{q^2}{M^2 - m^2} f_-(q^2).$$
 (2.70)

Substituting this expression gives the form factor decomposition

$$\langle P(k) | \mathcal{V}^{\mu}(0) | B_s(p) \rangle = 2f_+(q^2) \left(p^{\mu} - \frac{p \cdot q}{q^2} q^{\mu} \right) + f_0(q^2) \frac{M^2 - m^2}{q^2} q^{\mu}.$$
 (2.71)

In the limit of $q^2 \to 0$, this matrix element must not diverge, and so $f_+(0) = f_0(0)$. This constraint on the form factors will be referred to as the kinematic constraint.

2.7 Correlation functions

Form factor information can be obtained through lattice simulations through the measurement of two and three-point correlation functions.

In the example case of $B_s \to K\ell\nu$, where we create a B_s meson (at rest) at time $t_{src}=0$ and destroy the Kaon at the sink at $t_{snk}=\Delta t$, and the flavour changing current, $\mathcal{V}_{\mu}=\bar{u}\gamma_{\mu}b$ acts at time t (as shown in Figure 2.6). The three-point correlation function is of the form

$$C_{3,\mu}(t,\Delta_t,\mathbf{p}_K) = \sum_{\mathbf{x},\mathbf{y}} e^{i\mathbf{p}_K\cdot\mathbf{y}} \langle 0|\mathcal{O}_{\mathrm{B}_{\mathrm{s}}}(\mathbf{x},\Delta t)\mathcal{V}_{\mu}(\mathbf{y},t)\mathcal{O}_K^{\dagger}(\mathbf{0},0)|0\rangle$$
(2.72)

We make use of the relation $\mathcal{O}(\mathbf{x},t) = e^{\hat{H}t}e^{i\hat{\mathbf{p}}.\mathbf{x}}\mathcal{O}(\vec{0},0)e^{-\hat{H}t}e^{-i\hat{\mathbf{p}}.\mathbf{x}}$:

$$C_{3,\mu}(t,\Delta_t,\mathbf{p}_K) = \sum_{\mathbf{x},\mathbf{y}} e^{i\mathbf{p}_K\cdot\mathbf{y}} \langle 0|e^{\hat{H}\Delta t}\mathcal{O}_{\mathsf{B}_{\mathsf{S}}}(\mathbf{x},0)e^{-\hat{H}\Delta t}e^{\hat{H}t}V_{\mu}(\mathbf{y},0)e^{-\hat{H}t}\mathcal{O}_K^{\dagger}(\mathbf{0},0)|0\rangle \qquad (2.73)$$

We insert complete sets of states, *n* and *m*:

$$C_{3,\mu}(t,\Delta_t,\mathbf{p}_K) = \sum_{\mathbf{x},\mathbf{y},n,m} e^{i\mathbf{p}_K\cdot\mathbf{y}} \langle 0|\mathcal{O}_{\mathrm{B}_{\mathrm{s}}}(\mathbf{x},0)e^{-E_n\Delta t} \frac{|n\rangle\langle n|}{2E_n} e^{E_n t} V_{\mu}(\mathbf{y},0)e^{-E_m t} \frac{|m\rangle\langle m|}{2E_m} \mathcal{O}_K^{\dagger}(\mathbf{0},0)|0\rangle,$$
(2.74)

where our exponentiated Hamiltonians have acted on states, n and m, constraining their momenta (their other quantum numbers are constrained by the matrix elements):

$$C_{3,\mu}(t, \Delta_t, \mathbf{p}_K) = \sum_{\mathbf{x}, \mathbf{y}, n, m} \frac{e^{-E_n(\Delta t - t)} e^{-E_m t}}{4E_n E_m} e^{i\mathbf{p}_K \cdot \mathbf{y}}$$

$$\times \langle 0 | \mathcal{O}_{\mathbf{B}_{\mathbf{s}}}(\mathbf{x}, 0) | B_s^{(n)} \rangle \langle B_s^{(n)} | V_{\mu}(\mathbf{y}, 0) | K^{(m)} \rangle \langle K^{(m)} | \mathcal{O}_K^{\dagger}(\mathbf{0}, 0) | 0 \rangle$$

$$(2.75)$$

For sufficiently long time separations, this is dominated by the ground states (as these are the lowest energy states, the exponential terms decay slower than for other states), B_s and K. In the limit $t \to \infty$:

$$C_{3,\mu}(t,\Delta_t,\mathbf{p}_K) = \sum_{\mathbf{x},\mathbf{y}} \frac{e^{M_{\mathrm{B}_{\mathrm{S}}}(\Delta t - t)}e^{-E_K t}}{4M_{\mathrm{B}_{\mathrm{S}}}E_K} e^{i\mathbf{p}_K \cdot \mathbf{y}} \langle 0|\mathcal{O}_{\mathrm{B}_{\mathrm{S}}}(\mathbf{x},0)|B_{\mathrm{S}}\rangle \langle B_{\mathrm{S}}|V_{\mu}(\mathbf{y},0)|K\rangle \langle K|\mathcal{O}_K^{\dagger}(\mathbf{0},0)|0\rangle$$
(2.76)

To extract the matrix element $\langle B_s|V_{\mu}(\mathbf{y},0)|K\rangle$, we make use of the following 2-point correlation functions:

$$C_{B_s}(t,\mathbf{0}) = \sum_{\mathbf{x}} \langle 0 | \mathcal{O}_{B_s}(\mathbf{x},t) \mathcal{O}_{B_s}(\mathbf{0},0) | 0 \rangle$$
 (2.77)

$$C_K(t, \mathbf{p}_k) = \sum_{\mathbf{x}} e^{i\mathbf{p}_k \cdot \mathbf{x}} \langle 0 | \mathcal{O}_K(\mathbf{x}, t) \mathcal{O}_K(\mathbf{0}, 0) | 0 \rangle$$
 (2.78)

Repeating the same procedure and taking the limit $t \to \infty$ gives:

$$C_{B_s}(t, \mathbf{0}) = |\langle 0 | \mathcal{O}_{B_s}(\mathbf{0}, 0) | B_s(\mathbf{0}) \rangle|^2 \frac{e^{-M_{B_s}t}}{2M_{B_s}}$$

$$C_K(t, \mathbf{p}_k) = |\langle 0 | \mathcal{O}_K(\mathbf{0}, 0) | K(\mathbf{p}_k) \rangle|^2 \frac{e^{-E_K t}}{2E_K}$$
(2.80)

$$C_K(t, \mathbf{p}_k) = |\langle 0|\mathcal{O}_K(\mathbf{0}, 0)|K(\mathbf{p}_k)\rangle|^2 \frac{e^{-E_K t}}{2E_K}$$
(2.80)

We can extract our desired matrix element by taking the ratio of our 3-point function with the square root of these 2-point functions.

This can be done for many values of Kaon momentum, allowing us to measure the matrix element for various values of q^2 . Once the chiral continuum extrapolation has been performed, this allows us to generate form factor values from the lattice.

Practically, we are limited on how many form factor values we can generate on the lattice to avoid the covariance matrix becoming singular. As f_+ cannot be determined at q_{max}^2 , in the case of an odd number of points, we choose to allocate an extra point to f_0 (so if we can only extract 5 form factor points from the lattice simulation results before making the covariance matrix singular, we choose to take 3 values for f_0 and 2 for f_+) [60].

Form Factors and Phenomenology 2.8

2.8.1 **Differential Decay Rate**

To compare experimental results with theoretical predictions from the lattice, an important phenomenological value is the differential decay rate:

$$\frac{d\Gamma\left(B_{(s)} \to P\ell\nu\right)}{dq^{2}} = \frac{G_{F}^{2} |V_{ub}|^{2}}{24\pi^{3}} \frac{\left(q^{2} - m_{\ell}^{2}\right)^{2} \sqrt{E_{P}^{2} - M_{P}^{2}}}{q^{4}M_{B_{(s)}}^{2}} \times \left[\left(1 + \frac{m_{\ell}^{2}}{2q^{2}}\right) M_{B_{(s)}}^{2} \left(E_{P}^{2} - M_{P}^{2}\right) |f_{+}(q^{2})|^{2} + \frac{3m_{\ell}^{2}}{8q^{2}} \left(M_{B_{(s)}}^{2} - M_{P}^{2}\right)^{2} |f_{0}(q^{2})|^{2}\right] \tag{2.81}$$

With knowledge of the functional dependence of the form factors, extrapolated from lattice results, we can calculate all parts of this equation besides $|V_{ub}|$. The differential decay rate without the CKM matrix factor, $d\tilde{\Gamma}/dq^2$ is given by

$$\frac{d\tilde{\Gamma}}{dq^2} = \frac{1}{|V_{ub}|^2} \frac{d\Gamma}{dq^2} \tag{2.82}$$

With binned experimental measurements of the differential decay rate, and by integrating $d\tilde{\Gamma}/dq^2$ from our theoretical predictions over the same bins, we can extract $|V_{ub}|$.

2.8.2 Forward-Backward Asymmetry

The angular dependence of the differential decay rate is given by

$$\frac{d^{2}\Gamma(B_{s} \to K\ell\nu)}{dq^{2}d\cos\theta_{l}} = \eta_{EW} \frac{G_{F}^{2}|V_{ub}|^{2}}{128\pi^{3}M_{B_{s}}^{2}} \left(1 - \frac{m_{\ell}^{2}}{q^{2}}\right)^{2} \times |\mathbf{p}_{K}| \left[4M_{B_{s}}^{2}|\mathbf{p}_{K}|^{2} \left(\sin^{2}\theta_{l} + \frac{m_{\ell}^{2}}{q^{2}}\cos^{2}\theta_{\ell}\right) f_{+}^{2}(q^{2}) + \frac{m_{\ell}^{2}}{q^{2}} (M_{B_{s}}^{2} - M_{K}^{2})M_{B_{s}}|\mathbf{p}_{K}|\cos\theta_{\ell}f_{0}(q^{2})f_{+}(q^{2}) + \frac{m_{\ell}}{q^{2}} (M_{B_{s}}^{2} - M_{K}^{2})^{2}f_{0}^{2}(q^{2})\right], \tag{2.83}$$

where θ_ℓ is the angle between the incoming B_s and the outgoing charged-lepton in the dilepton rest frame. The forward-backward asymmetry is the difference in the integrated decay rate in the forward ($0 \le cos\theta_\ell \le 1$) and backward directions ($-1 \le cos\theta_\ell \le 0$) [88]:

$$\mathcal{A}_{FB}^{\ell}(q^2) \equiv \begin{bmatrix} \int_{0}^{1} - \int_{-1}^{0} d \cos \theta_{\ell} \frac{d^2 \Gamma(B_s \to K \ell \nu)}{dq^2 d \cos \theta_{\ell}} \end{bmatrix}$$
(2.84)

$$\mathcal{A}_{FB}^{\ell}(q^2) = \eta_{EW} \frac{G_F^2 |V_{ub}|^2}{32\pi^3 M_{B_s}} \left(1 - \frac{m_{\ell}^2}{q^2} \right)^2 |\mathbf{p}_K|^2$$

$$\times \frac{m_{\ell}^2}{q^2} \left(M_{B_s}^2 - M_K^2 \right) f_+(q^2) f_0(q^2)$$
(2.85)

2.8.3 R Ratio

Another important test of the Standard Model is lepton flavour universality (LFU), which occurs due to the identical couplings to the weak gauge bosons from each generation of lepton. Differences in masses between the leptons causes the shapes of the decay rates to differ.

The R ratio tests LFU and is largely free of hadronic uncertainties:

$$R_{B_s \to K} = \frac{\int_{m_\tau^2}^{q_{\text{max}}^2} dq^2 \frac{d\Gamma(B_s \to K\tau\bar{\nu}_\tau)}{dq^2}}{\int_{m_\ell^2}^{q_{\text{max}}^2} dq^2 \frac{d\Gamma(B_s \to K\ell\bar{\nu}_\ell)}{dq^2}}$$
(2.86)

Here, ℓ denotes either e or μ , which are both essentially massless compared to the tau lepton and the kinematic range of q^2 .

An improved R ratio can be constructed to improve upon several features present in $R_{B_s \to K}$ [88]:

- The integration range from $m_\ell^2 \le q^2 \le m_\tau^2$ in the denominator is unmatched in the numerator. This can be solved by choosing a common integration range starting at q_{\min}^2 (where $q_{\min}^2 \ge m_\tau^2$).
- A weighting factor is introduced, ω , that scales the differential decay rate by the phase space factor related to lepton mass. This factor makes the f_+ components of the numerator and denominator the same.

This phase space weighting comes from the following expression for the differential decay rate:

$$\frac{d\Gamma(B_s \to K\ell\nu)}{dq^2} = \Phi\omega_\ell(q^2) \left[F_V^2 + (F_S^\ell)^2 \right]$$
 (2.87)

Where

$$\Phi = \eta_{\rm EW} \frac{G_F^2 |V_{ub}|^2}{24\pi^3},\tag{2.88}$$

$$\omega_{\ell}(q^2) = \left(1 - \frac{m_{\ell}^2}{q^2}\right)^2 \left(1 + \frac{m_{\ell}^2}{2q^2}\right),\tag{2.89}$$

$$F_V^2 = |\mathbf{p}_K|^3 |f_+(q^2)|^2, \tag{2.90}$$

$$(F_S^{\ell})^2 = \frac{3}{4} \frac{m_{\ell}^2 |\mathbf{p}_K|}{m_{\ell}^2 + 2q^2} \frac{(M_{B_s}^2 - M_K^2)^2}{M_{B_s}^2} |f_0(q^2)|^2.$$
 (2.91)

Our improved R ratio is then given by:

$$R_{B_s \to K}^{\text{imp}} = \frac{\int_{q_{\text{min}}^2}^{q_{\text{max}}^2} dq^2 \frac{d\Gamma(B_s \to K\tau\bar{\nu}_\tau)}{dq^2}}{\int_{q_{\text{min}}^2}^{q_{\text{max}}^2} dq^2 \left[\frac{\omega_\tau(q^2)}{\omega_\ell(q^2)}\right] \frac{d\Gamma(B_s \to K\ell\nu)}{dq^2}}$$
(2.92)

We note that the contribution of the scalar term, $(F_S^\ell)^2$, in the denominator is very small $(m_{e,\mu}^2/2q^2 \le m_\mu^2/2q^2 \le m_\mu^2/2m_\tau^2 = 0.002$ in the integration range), and so we ignore it in our denominator. Our simplified approximation of the R ratio is:

$$R_{B_s \to K}^{\text{imp}} \approx 1 + \frac{\int_{q_{\min}^2}^{q_{\max}^2} dq^2 \omega_{\tau}(q^2) (F_S^{\tau})^2}{\int_{q_{\infty}^2}^{q_{\max}^2} dq^2 \omega_{\tau}(q^2) F_V^2}$$
(2.93)

Chapter 3

Statistical Techniques

3.1 Bootstrapping

A statistical technique used extensively in this work is bootstrapping, which allows the propagation of statistical uncertainties throughout the analysis.

The primary input data for this analysis are synthetic form factor values from lattice simulations, with an associated covariance matrix. The bootstrapping procedure involves generating numerous resamples of these data points and performing the same analysis on each resample [37].

With a sufficiently large number of samples, the distribution of outcomes will capture the statistical uncertainty from the distribution of inputs, without relying on assumptions about the underlying error distribution.

3.2 Kolmogorov–Smirnov test

A statistical tool employed multiple times in this work is the Kolmogorov–Smirnov (K-S) test [49]. This allows us to test whether two sets of data are likely to be samples from the same underlying distribution. There are two main ways we use this test in this work.

The first is to determine if a given distribution is consistent with the uniform distribution. Firstly, we take many sets of samples of a uniform distribution between the minimum and maximum value. These sets consist of n samples, where n is the number of elements in our test data.

For each set, we measure the Kolmogorov–Smirnov statistic, $D_{n,m}$, which is the maximum difference between the sample's empirical distribution function (EDF),

 $F_{1,n}(x)$, and the uniform distribution's cumulative distribution function (CDF), $F_{2,m}(x)$ [74]:

$$D_{n,m} = \sup_{x} |F_{1,n}(x) - F_{2,m}(x)|$$
(3.1)

The P-value is then the proportion of sets with a greater or equal Kolmogorov–Smirnov statistic than that of the distribution we are testing. If the P-value is within the range, $0.05 < x \le 1$ (here we denote this as $\alpha = 0.05$) then we do not have sufficient evidence to reject our null hypothesis (the distribution of curves is uniform).

The second way we use this test is to determine if two distributions are from the same, unknown, underlying distribution. Here we use the two-sample Kolmogorov–Smirnov test, which involves the same measure (Kolmogorov–Smirnov statistic), but we only need to compare the two distributions once as we are not sampling from a known distribution for comparison. The threshold for rejecting the null hypothesis, at level α , is:

$$D_{n,m} > \sqrt{-\ln\left(\frac{\alpha}{2}\right) \cdot \frac{1 + \frac{m}{n}}{2m}} \tag{3.2}$$

Chapter 4

Choice of Data

The analysis in this work focuses on two semileptonic pseudoscalar to pseudoscalar decays, $B \to \pi \ell \nu$ and $B_s \to K \ell \nu$. The lattice data used for each decay consists of the synthetic points and their covariances (both systematic and statistical).

4.1 $B \rightarrow \pi \ell \nu$

For $B \to \pi \ell \nu$, form factor results from the JLQCD collaboration are chosen [80]. The synthetic form factor points are given in Table 4.1, with statistical and systematic correlation matrices given in Tables 4.2 and 4.3.

	$f_{+}(q_1^2)$	$f_{+}(q_2^2)$	$f_{+}(q_3^2)$	$f_0(q_1^2)$	$f_0(q_2^2)$	$f_0(q_3^2)$
Mean	1.165	2.600	6.597	0.500	0.703	0.937
Stat. err	0.067	0.152	0.423	0.019	0.026	0.036
Syst. err	0.099	0.229	0.631	0.027	0.037	0.043

Table 4.1: Synthetic data points for f_+ and f_0 at $q_1^2=19.15 GeV^2$, $q_2^2=23.65 GeV^2$ and $q_3^2=26.40 GeV^2$

	$f_{+}(q_1^2)$	$f_{+}(q_2^2)$	$f_{+}(q_3^2)$	$f_0(q_1^2)$	$f_0(q_2^2)$	$f_0(q_3^2)$
$f_{+}(q_1^2)$	1.000	0.957	0.901	0.799	0.728	0.663
$f_{+}(q_{2}^{2})$	0.957	1.000	0.989	0.758	0.720	0.662
$f_{+}(q_3^2)$	0.901	0.989	1.000	0.708	0.682	0.639
$f_0(q_1^2)$	0.799	0.758	0.708	1.000	0.971	0.921
$f_0(q_2^2)$	0.728	0.720	0.682	0.971	1.000	0.943
$f_0(q_3^{\bar{2}})$	0.663	0.662	0.639	0.921	0.943	1.000

Table 4.2: Statistical correlation matrix for f_+ and f_0 at $q_1^2=19.15 GeV^2$, $q_2^2=23.65 GeV^2$ and $q_3^2=26.40 GeV^2$

To obtain phenomenological results for $B \to \pi \ell \nu$, several sources of experimental results will be used. These experimental results consist of binned integrated branching

	$f_{+}(q_1^2)$	$f_{+}(q_{2}^{2})$	$f_{+}(q_3^2)$	$f_0(q_1^2)$	$f_0(q_2^2)$	$f_0(q_3^2)$
$f_{+}(q_1^2)$	1.000	0.996	0.969	0.761	0.675	0.692
$f_{+}(q_{2}^{2})$	0.996	1.000	0.981	0.737	0.650	0.663
$f_{+}(q_{3}^{2})$	0.969	0.981	1.000	0.682	0.590	0.604
$f_0(q_1^2)$	0.761	0.737	0.682	1.000	0.992	0.996
$f_0(q_2^2)$	0.675	0.650	0.590	0.992	1.000	0.996
$f_0(q_3^{\bar{2}})$	0.692	0.663	0.604	0.996	0.996	1.000

TABLE 4.3: Systematic correlation matrix for f_+ and f_0 at $q_1^2=19.15 GeV^2$, $q_2^2=23.65 GeV^2$ and $q_3^2=26.40 GeV^2$

fractions, alongside systematic and statistical covariance matrices (or correlation matrices with corresponding errors). The experimental results chosen are:

- Belle 2010 [64] $B^0 \to \pi^- \ell^+ \nu$ branching fractions from EPAPS Table III, with associated statistical and systematic correlation matrices from Tables I and II.
- Belle 2013 [68] Combined $\bar{B}^0 \to \pi^+$ and $B^- \to \pi^0$ branching fractions, and correlation matrices given in Tables XVII-XX.
- BaBar 2010 [62] $B^0 \to \pi^-$ 4-mode fit branching fraction given in Table X, with total correlation matrix from TABLE XXI.
- BaBar 2012 [65] Combined $B^0 \to \pi^-$ and $B^+ \to \pi^0$ branching fractions, given in Table XXIII, with statistical and systematic correlation matrices from Tables XXVIII and TABLE XXXI.

In all cases, branching fractions are converted into differential decay rates using lifetimes from the Particle Data Group [91].

4.1.1 Combining data for Belle 2013

For Belle 2013 there are 2 sets of data, one for $\bar{B}^0 \to \pi^+$ and the other for $B^- \to \pi^0$. For each we have binned branching fractions, statistical error, systematic error, total error, and statistical correlation matrix. Each decay has different bins, 13 for $\bar{B}^0 \to \pi^+$ and 7 for $B^- \to \pi^0$.

We rescale each decay by the lifetime and isospin factor to give the differential decay rate:

$$\Delta \mathcal{B}(\bar{B}^0 \to \pi^+ \ell \nu) = 2 \frac{\tau_{\bar{B}^0}}{\tau_{B^-}} \Delta \mathcal{B}(B^- \to \pi^0 \ell \nu) \tag{4.1}$$

For a given decay, the integrated branching fraction bins have systematic error that is fully correlated. Between decays, the systematic correlation is 0.49 (estimated by Belle

4.2. $B_s \rightarrow K\ell\nu$

in [68]). From this, we construct a 20x20 systematic correlation matrix. The statistical error is not correlated between decays, so the full correlation matrix is block diagonal. From these, we construct the statistical and systematic covariance matrices from the statistical and systematic errors. The total covariance matrix is then the sum of these.

4.2
$$B_s \rightarrow K\ell\nu$$

For $B_s \to K\ell\nu$, we use synthetic form factor values from the RBC/UKQCD collaboration's 2023 paper [88]. These form factor points are generated at $q^2 = 17.6$, 20.8 and 23.4 GeV^2 for f_0 , and at $q^2 = 17.6$ and 23.4 GeV^2 for f_+ . Tables VII and VIII give the central values, errors and correlation matrices for these points.

 $B_s \to K \ell \nu$ experimental data is very limited, so extraction of V_{ub} will only be performed using data from the LHCb collaboration [76], that measures the ratio of branching fractions for $B_s^0 \to K^- \ell \nu$ and $B_s^0 \to D_s^- \ell \nu$, using the procedure outlined in [88].

Chapter 5

Dispersive Bounds

 $\Pi_J^{\mu\nu}$ is the two-point momentum-space Green's Function of a vector-like quark current, $J^\mu \equiv \bar{Q}\Gamma^\mu Q'$. We can decompose $\Pi_J^{\mu\nu}$ into spin-1 (Π_{1^-}) and spin-0 (Π_{0^+}) components:

$$\Pi_J^{\mu\nu}(q) \equiv i \int d^4x e^{iq\cdot x} \langle 0|TJ^{\mu}(x)J^{\dagger\nu}(0)|0\rangle \tag{5.1}$$

$$= \frac{1}{q^2} \left(q^{\mu} q^{\nu} - q^2 g^{\mu \nu} \right) \Pi_{1^-} \left(q^2 \right) + \frac{q^{\mu} q^{\nu}}{q^2} \Pi_{0^+} \left(q^2 \right) \tag{5.2}$$

We define $z(t;t_0)$ as

$$z(t;t_0) \equiv \frac{\sqrt{t_{\text{cut}} - t} - \sqrt{t_{\text{cut}} - t_0}}{\sqrt{t_{\text{cut}} - t} + \sqrt{t_{\text{cut}} - t_0}},$$
(5.3)

We define t_{cut} as the minimum value of the invariant mass squared required for the vacuum to produce a physical quark–antiquark pair. In practical terms, it's the energy threshold at which pair production becomes possible, marking the beginning of the continuum region in dispersion relations.

 $t_0 = t_{cut} - \sqrt{t_{cut}(t_{cut} - (M - m)^2)}$ is a common choice to make z(t) symmetric around 0 for the range of available t values (M and m are the masses of the initial-state meson and final-state meson in the decay, respectively). This mapping takes the q^2 complex plane onto a unit disc.

For a semi-leptonic pseudoscalar to pseudoscalar decay, the imaginary parts of the longitudinal and transverse components of the HVP tensors are related to their derivatives via the following dispersion relations:

$$\chi_{0^{+}}(Q^{2}) \equiv \frac{\partial}{\partial q^{2}}[q^{2}\Pi_{0^{+}}(q^{2})] = \frac{1}{\pi} \int_{0}^{\infty} dz \, \frac{z \text{Im}\Pi_{0^{+}}(z)}{z^{2}},$$
(5.4)

$$\chi_1^-(Q^2) \equiv \frac{1}{2} \left(\frac{\partial}{\partial q^2} \right)^2 [q^2 \Pi_{1^-}(q^2)] = \frac{1}{\pi} \int_0^\infty dz \frac{z \text{Im} \Pi_{1^-}(z)}{z^3},$$
(5.5)

Where q^2 is the momentum of the outgoing lepton pair, and

$$Im\Pi_{J} = \frac{1}{2} \sum_{n} \int d\mu(n) (2\pi)^{4} \delta^{(4)}(q - p_{n}) |\langle 0|J|n \rangle|^{2}.$$
 (5.6)

Here a complete set of states has been inserted with the same quantum numbers as a generic current, J. $d\mu(n)$ is the phase space for the states, n. $\chi(Q^2)$ are known as the susceptibilities, and the values used in this work are from the 2023 RBC/UKQCD paper [88], calculated perturbatively using the common choice of $Q^2=0$:

$$\chi_{1^{-}}(0) = 6.03 \times 10^{-4} \text{GeV}^{-2}$$

$$\chi_{0^{+}}(0) = 1.48 \times 10^{-2}$$
(5.7)

These susceptibilities will be denoted as χ_{1^-} and χ_{0^+} (ignoring the $Q^2=0$). The completeness sum is positive semidefinite. By inserting a subset of hadronic states we can obtain inequalities allowing us to bound the form factors. In this case, we consider those relating to two decays, $B_s \to K\ell\nu$ and $B \to \pi\ell\nu$. For a generic susceptibility (from the current-current correlator), χ , we have

$$\chi(q^2) \ge \frac{1}{\pi} \int_{t_{cut}}^{\infty} dt \frac{W(t)|f(t)|^2}{(t-q^2)^a}$$
 (5.8)

where a is the degree of subtraction (a = 2 for $J = 0^+$ and a = 3 for $J = 1^-$). For a given spin-parity channel, we may write the dispersion relation as:

$$\frac{1}{2\pi i} \int_{|z|=1} \frac{dz}{z} |\phi(z)f(z)|^2 \le \chi \tag{5.9}$$

The full derivation of W(t) and the outer functions ϕ can be found in Appendix B. We introduce Blaschke factors, $B_0(z)$ and $B_+(z)[1]$, for our two form factors f_0 and f_+ , respectively. The Blaschke factor for a given pole is defined as

$$B(z;a) = \frac{z - z(q_{\text{pole}}^2)}{1 - \overline{z}(q_{\text{pole}}^2)z}.$$
 (5.10)

These Blaschke factors ensure analyticity in the presence of sub-threshold poles without changing the value of the integrand on the unit disc, leaving the integral unchanged.

$$\frac{1}{2\pi i} \int_{|z|=1} \frac{dz}{z} |B_i(z)\phi_i(z)f_i(z)|^2 \le \chi_i$$
 (5.11)

From this dispersion relation, we can proceed in two different ways. One approach, which I will denote the z-fit method, makes use of the analyticity of the integrand by expanding it in terms of a power series in z, which I shall discuss in Section 6 [44, 46, 48, 59].

The second approach I will explore in Section 7 is the Dispersive Matrix (DM) method, which uses the inequality in Equation 5.11 to bound the form factor at any z (hence q^2), independent of any parametrisation or assumed functional form. These bounds are commonly referred to as "unitarity bounds". The DM method can exploit known information on the form factors to tighten the bounds [36, 47, 24, 25, 26].

In both cases, kinematic constraints on the form factors, for example the relation $f_+(0) = f_0(0)$ for the semileptonic decays of interest here, can also be taken into account.

Chapter 6

Z-Fits

Parametrizing form factors to extrapolate theoretical predictions has a long history. Some examples include the Ball-Zwicky approach (which utilises light-cone sum rules) [54], the Becirevic-Kaidalov parameterization [50] and Bauer-Stech-Wirbel parameterization [42]. In recent times, these have fallen out of favour in comparison to parametrizations stemming from dispersion relations, such as the BCL [59] and BGL [44, 46, 48] parametrizations, which, by relying only on general quantum field theory properties of analyticity and unitarity, are model-independent.

6.1 BGL Parametrization

From Equation 5.11, our dispersion relation is given by:

$$\frac{1}{2\pi i} \int_{|z|=1} \frac{dz}{z} |B_i(z)\phi_i(z)f_i(z)|^2 \le \chi_i$$
 (6.1)

As the integrand of our dispersion relation is analytic, by construction in the unit disc, we may expand as power series (note that χ_i is absorbed into ϕ_i):

$$f_0(z) = \frac{1}{B_0(z)\phi_0(z)} \sum_{n=0}^{\infty} a_n z^n$$
 (6.2)

$$f_{+}(z) = \frac{1}{B_{+}(z)\phi_{+}(z)} \sum_{n=0}^{\infty} b_{n} z^{n}$$
(6.3)

This power series expansion is known as the BGL expansion [44, 46, 48]. The unitarity constraint is then given by

$$\sum_{n=0}^{\infty} |a_n|^2 \le 1, \quad \sum_{n=0}^{\infty} |b_n|^2 \le 1 \tag{6.4}$$

The kinematic constraint, which enforces that our form factors must be equal at $z(q^2 = 0)$, is a linear relation between the a_n and b_n , allowing any one of them to be expressed in terms of the others.

$$\frac{1}{B_0(z(q^2=0))\phi_0(z(q^2=0))} \sum_{n=0}^{\infty} a_n z(q^2=0)^n - \frac{1}{B_+(z(q^2=0))\phi_+(z(q^2=0))} \sum_{n=0}^{\infty} b_n z(q^2=0)^n = 0.$$
(6.5)

The number of independent synthetic form-factor points available from lattice data is relatively limited. This in turn limits the number of terms we can use in a z-expansion when making a (frequentist) fit. Hence, although the full z-expansion is model-independent, in practice we have to consider the systematic effect of using a truncated expansion. If experimental inputs are also used, then it becomes possible to use higher order truncations of the z-series.

6.2 BCL Parametrization

This parametrization was created to improve upon some limitations of the BGL approach. It makes use of an additional constraint on the derivative of f_+ [59]:

$$\left. \left[\frac{df_+}{dz} \right] \right|_{z=-1} = 0 \tag{6.6}$$

This comes from angular momentum conservation, and enforces that the form factor obeys the known asymptotic behaviour near the $B\pi$ production threshold [72]. The constraint imposes an additional linear relation on the expansion coefficients for f_+ . In a truncation of the BCL series for f_+ , is it usually taken into account by writing

$$f_{+}(q^{2}) = \frac{1}{1 - q^{2}/m_{B^{*}}^{2}} \sum_{k=0}^{K-1} b_{+}^{(k)} \left[z^{k} - (-1)^{k-K} \frac{k}{K} z^{K} \right]$$
(6.7)

There is no equivalent derivative constraint for f_0 , so we have the following expressions:

$$f_0^{B\pi}(q^2) = \sum_{k=0}^{K-1} b_0^{(k)} z^k$$
 (6.8)

$$f_0^{B_sK}(q^2) = \frac{1}{1 - q^2/m_{B_{(0^+)}^*}^2} \sum_{k=0}^{K-1} b_0^{(k)} z^k$$
(6.9)

Unfortunately, the BCL expansion has no direct unitarity constraint, and instead one can be obtained from mapping the BCL coefficients to those in a BGL expansion and utilizing this unitarity constraint [59]. In this analysis, the BGL expansion is exclusively used, as this comes directly from the dispersion relation.

6.3 Fitting Procedure

To perform the form factor extrapolation using only the lattice data, the statistical and systematic errors of the synthetic data points may be factored in to the results through bootstrapping.

The synthetic data points are resampled n_{boot} times, and for each resample we perform our fitting procedure assuming perfect knowledge of the form factors at these points. For a given resample, we find the optimal set of coefficients by minimising χ^2 , our squared residual,

$$\chi^{2} = \left(\vec{F}_{calc} - \vec{F}_{lattice}\right)^{T} M_{cov}^{-1} \left(\vec{F}_{calc} - \vec{F}_{lattice}\right), \tag{6.10}$$

where \vec{F}_{calc} are the values of the form factors (f_0 and f_+) calculated from the coefficients, $\vec{F}_{lattice}$ are the resampled form factor values from the lattice data, and M_{cov} is the covariance matrix of the lattice form factor values. This minimisation is done through multivariable minimisation, in this case using the "BFGS" method using SciPy's optimize.minimize function [75]. The variables being minimised are all but one of the coefficients for the form factors, as one can be expressed in terms of all others due to the kinematic constraint. This optimisation is constrained through unitarity, which dictates that the sum of squares of coefficients for a form factor must not exceed 1.

This process is repeated for all $n_{\rm boot}$ resamples, allowing analysis to be performed on each set of coefficients individually. When generating synthetic form factor input values from lattice data, the mean values and their covariance can be computed directly, enabling a z-fit using a single minimization. This approach assumes a Gaussian distribution for the coefficients. However, if you wish to investigate, for

example (as will be done in the following section), the impact of the unitarity constraint on the fit, a bootstrapping procedure is more appropriate.

6.4 Unitarity constraint

We can see how frequently the unitarity constraint influences the optimal coefficients generated for each resample of our inputs. Figure 6.1 shows the distribution of sums of coefficients squared for $B_s \to K\ell\nu$ and $B \to \pi\ell\nu$. In both cases, the unitarity constraint was ignored in the fitting procedure, and in all 10000 sets of coefficients the unitarity constraint was met regardless. This shows that this constraint never, for the synthetic data we are using, impacted the coefficients generated.



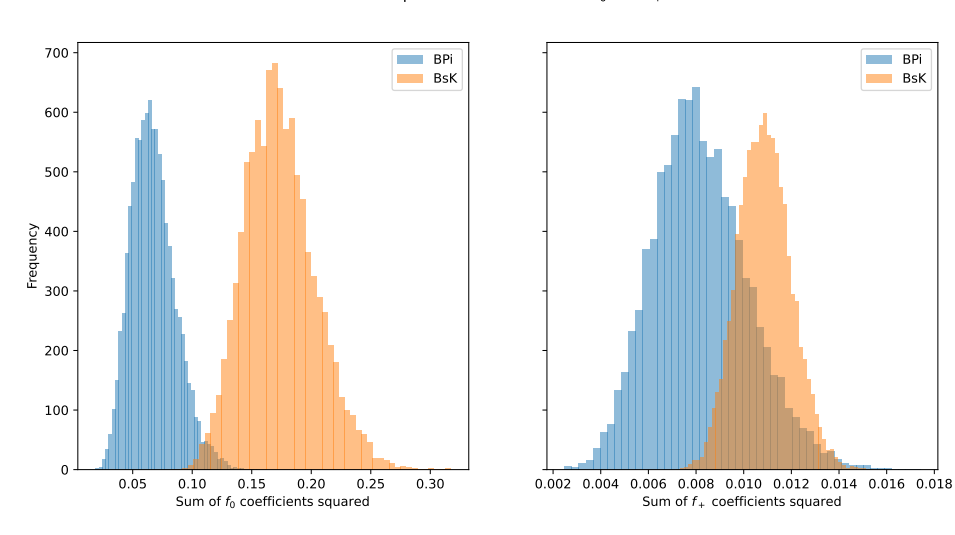


FIGURE 6.1: Sum of coefficients (10000 sets) squared for $B_s \to K\ell\nu$ and $B \to \pi\ell\nu$, fitted without consideration of the unitarity constraint, using synethetic form factor points from the RBC/UKQCD [88] and JLQCD [80] collaborations, respectively.

Decay
$$\beta \to \pi \ell \nu$$
 2.24 0.106
 $\beta \to \kappa \ell \nu$ 2.28 0.102

TABLE 6.1: $\chi^2/(\text{d.o.f.})$ and P-value for $B_s \to K\ell\nu$ and $B \to \pi\ell\nu$ fit without respecting the unitarity constraint.

6.5 Alternative polynomials

In the dispersion relation, the start of the cut is determined by the lowest energy state that can be produced from the vacuum by the current. The current and hence the start of the cut is the same for $B \to \pi \ell \nu$ and $B_s \to K \ell \nu$ decays. For $B_s \to K \ell \nu$ the cut starts

below the production threshold. As such, integrating over the whole unit disc adds unphysical contribution to the unitarity constraint [87].

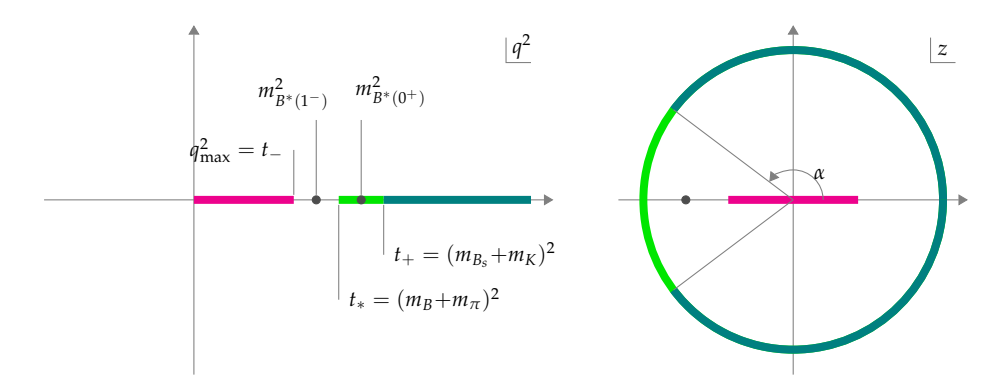


FIGURE 6.2: A schematic depiction of the mapping from the q^2 -plane (left) to the conformal z-plane (right). The coloured segments on the real axis denote the physical and unphysical regions for the $B \to K$ decay form factors, while the circle on the right represents the boundary of the unit disk after the conformal transformation.

When integrating over the unit circle, z^n form an orthonormal basis. For $B_s \to K\ell\nu$, we wish to construct a new orthonormal basis over the range $-\alpha \le \theta \le \alpha$, $\alpha = arg(z(q^2 = t_{th}))$, where $t_{th} = (m_{B_s} - m_K)^2$ (for $B_s \to K\ell\nu$, $\alpha = 1.117$). This can be done using the Gram-Schmidt process, as few orders of the polynomial are needed (these are the Rogers–Szegö polynomials [3]).

Equivalently, we can stick to expanding in powers of *z* over the restricted integration range, with a modified inner product [88]:

$$\langle z^{i}|z^{j}\rangle_{\alpha} = \frac{1}{2\pi} \int_{-\alpha}^{\alpha} d\phi(z^{i})^{*}z^{j}|_{z=e^{i\phi}},$$

$$= \begin{cases} \frac{\sin(\alpha(i-j))}{\pi(i-j)} & i \neq j \\ \frac{\alpha}{\pi} & i = j \end{cases}$$
(6.11)

The resulting unitarity constraint is

$$\sum_{i,j\geq 0} a_i^* \langle z^i \mid z^j \rangle_{\alpha} a_j \leq 1. \tag{6.12}$$

For the decay $B_s \to K\ell\nu$, the unitarity constraint rarely restricts the optimisation of coefficients. Figure 6.3 shows the distribution of coefficients, a_i , when fitting $B_s \to K\ell\nu$ using the circle and arc models (using the whole unit disc vs an arc of the disc, again, using data from the RBC/UKQCD collaboration [88]). Here i=0,1,2 correspond to the coefficients for f_0 and i=3,4 for f_+ .

We perform the two-sample Kolmogorov-Smirnov test to calculate the P-value associated with both sets of coefficients coming from the same unknown distribution.

As we are looking at 5 separate coefficients, we adjust our P-value threshold using the Bonferroni correction [12]. This means our previous threshold of $\alpha = 0.05$ now becomes $\alpha = 0.01$ (note that this is the α for the K-S test, not that which defines the arc we integrate over).

The results of these K-S tests indicate that the two sets of coefficients are consistent with the same distribution, giving evidence that the arc fitting method does not impact the fitting for this decay. This can be expected from the sums of squared coefficients given in 6.1, as for each decay the sum stays much below 1 for all 10000 resamples. As a result, the arc model, which does not overestimate the $B_s \to K\ell\nu$ contribution to the dispersive integral, will not have any practical difference in fitting. It is possible the differences between these two models is more significant for other decays where the start of the cut also does not coincide with the pair production threshold.

6.6 Z-Fits with 2 decays

Both $B \to \pi \ell \nu$ and $B_s \to K \ell \nu$ decays have the same weak flavour changing current. The following procedure allows simultaneous fitting of form factors for both decays using a shared unitarity constraint.

From Equation 5.6, we have

$$\operatorname{Im}\Pi_{0^{+},1^{-}} = \frac{1}{2} \sum_{n} \int d\mu(n) (2\pi)^{4} \delta^{(4)}(q - p_{n}) |\langle 0|J|n \rangle|^{2}.$$
 (6.13)

Here a complete set of states has been inserted with the same quantum numbers as a generic current, J. $d\mu(n)$ is the phase space for the states, n.

The completeness sum is positive semidefinite, and as such we may only consider a subset of hadronic states. In this case, we consider those relating to both decays, $B_s \to K\ell\nu$ and $B \to \pi\ell\nu$, where previously we restricted ourselves to one. For a generic susceptibility, χ , and form factor, f(t), we now have

$$\chi \ge \frac{1}{\pi} \int_{t_{th}}^{\infty} dt \frac{W(t)^{B_s K} |f(t)^{B_s K}|^2}{(t - q^2)^a} + \frac{1}{\pi} \int_{t_{cut}}^{\infty} dt \frac{W(t)^{B\pi} |f(t)^{B\pi}|^2}{(t - q^2)^a}.$$
(6.14)

W(t) for each decay is given by

Histograms of BsK Coefficients - Circle vs Arc Model

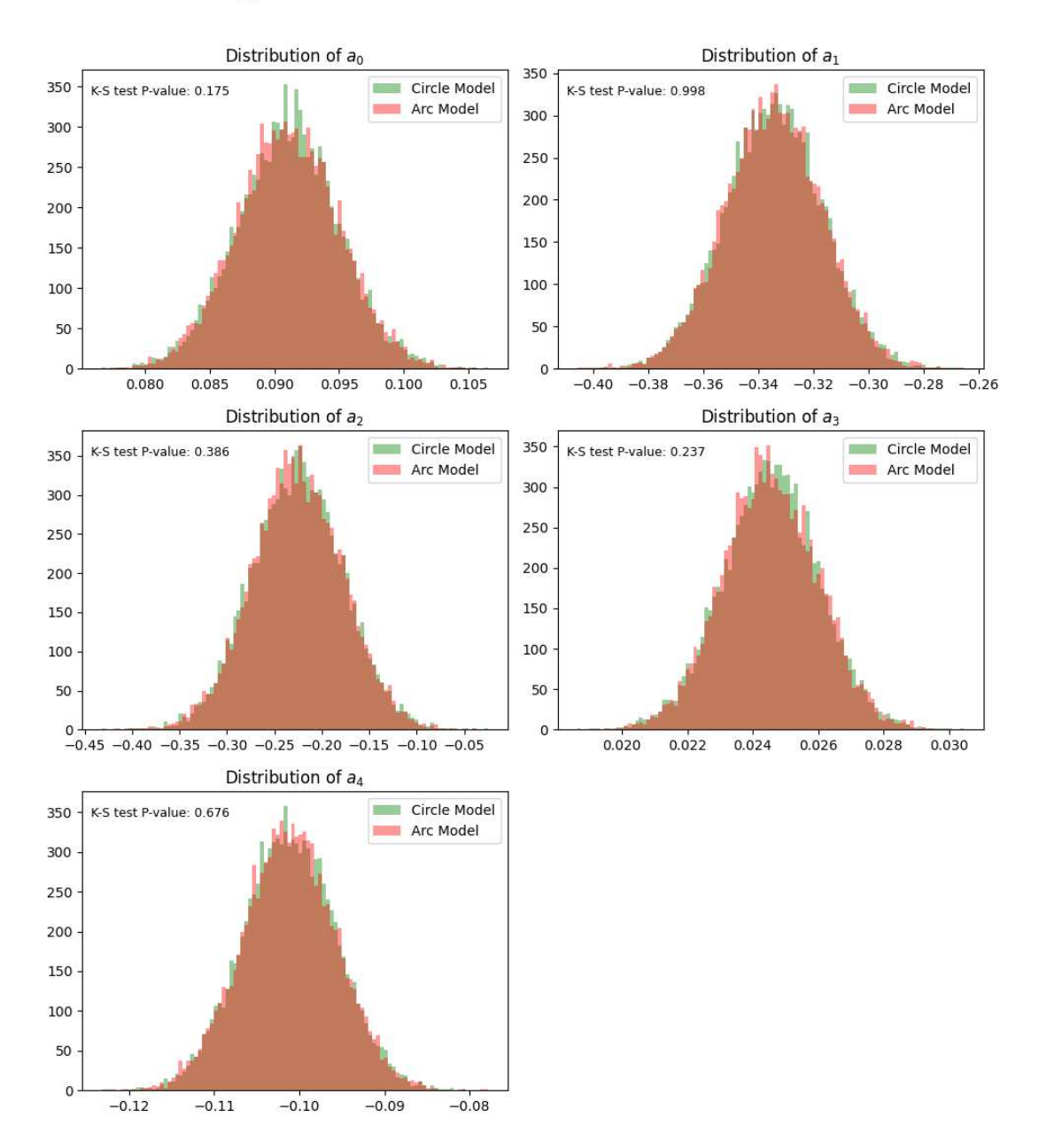


FIGURE 6.3: Distribution of BsK coefficients for the circle and arc (a restricted arc of the unit disc) models.

$$W_{+}^{B_sK}(t) = \frac{\eta^{B_sK}}{6\pi t^{\frac{1}{2}}} \left(\frac{(t - t_{+}^{B_sK})(t - t_{-}^{B_sK})}{4t} \right)^{\frac{3}{2}}, \tag{6.15}$$

$$W_0^{B_sK}(t) = \frac{\eta^{B_sK}}{8\pi t^{\frac{3}{2}}} (t_+^{B_sK} t_-^{B_sK}) \left(\frac{(t - t_+^{B_sK})(t - t_-^{B_sK})}{4t} \right)^{\frac{1}{2}}, \tag{6.16}$$

$$W_{+}^{B\pi}(t) = \frac{\eta^{B\pi}}{6\pi t^{\frac{1}{2}}} \left(\frac{(t - t_{+}^{B\pi})(t - t_{-}^{B\pi})}{4t} \right)^{\frac{3}{2}},\tag{6.17}$$

$$W_0^{B\pi}(t) = \frac{\eta^{B\pi}}{8\pi t^{\frac{3}{2}}} (t_+^{B\pi} t_-^{B\pi}) \left(\frac{(t - t_+^{B\pi})(t - t_-^{B\pi})}{4t} \right)^{\frac{1}{2}}, \tag{6.18}$$

Histograms of BsK Coefficients - Circle vs Arc Model

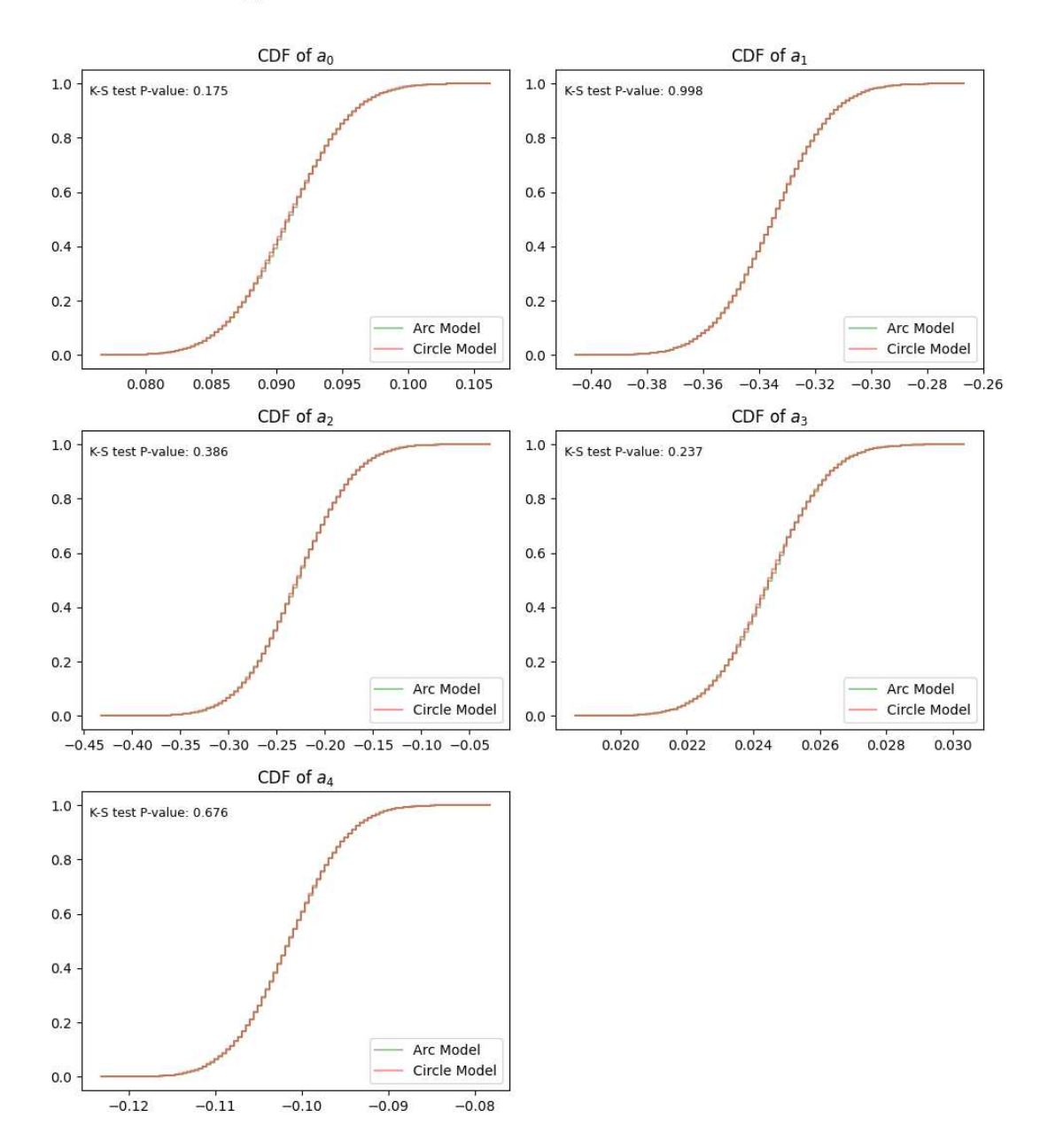


FIGURE 6.4: Distribution of BsK coefficients for the circle and arc (a restricted arc of the unit disc) models.

 $t_{\pm}^{B_sK}=(M_{B_s}\pm M_K)^2$, $t_{\pm}^{B\pi}=(M_B\pm M_\pi)^2$ and the isospin factors are $\eta^{B\pi}=\frac{3}{2}$ and $\eta^{B_sK}=1$ have been absorbed into W(t).

We again apply the conformal transformation

$$z(t) = \frac{\sqrt{t_{cut} - t} - \sqrt{t_{cut} - t_0}}{\sqrt{t_{cut} - t} + \sqrt{t_{cut} - t_0}},$$
(6.19)

where we choose $t_0 = t_{cut} - \sqrt{t_{cut}(t_{cut} - (M_{B_s} - M_K)^2)}$, which makes z(t) symmetric around 0 for the range of available t values, $[0, t_-^{B_s K}]$, for $B_s \to K \ell \nu$ (one could choose to make it symmetric for the range of z for either decay, or any other reasonable choice that keeps z small). We may now express Equation 6.14 as:

$$\chi \geq \frac{1}{2\pi i} \int_{\text{arc}} \frac{dz}{z} \left| B^{B_s K} \phi(z, q^2)^{B_s K} f(z)^{B_s K} \right|^2 + \frac{1}{2\pi i} \int_{|z|=1} \frac{dz}{z} \left| B^{B\pi} \phi(z, q^2)^{B\pi} f(z)^{B\pi} \right|^2$$
(6.20)

As in the single decay case, Blaschke factors, B, have been introduced to ensure analyticity in the presence of subthreshold poles. ϕ , the kinematical functions dependent on the form factor and decay, are given by:

$$\phi_{+}^{B_{s}K}(t;t_{0}) = \sqrt{\frac{\eta^{B_{s}K}}{48\pi}} \left(\frac{t_{cut} - t}{t_{cut} - t_{0}}\right)^{\frac{1}{4}} \left(\sqrt{t_{cut} - t} + \sqrt{t_{cut} - t_{0}}\right) \left(t_{+}^{B_{s}K} - t\right)^{\frac{3}{4}}$$

$$\left(\sqrt{t_{cut} - t} + \sqrt{t_{cut} - t_{-}^{B_{s}K}}\right)^{\frac{3}{2}} \left(\sqrt{t_{cut} - t} + \sqrt{t_{cut}}\right)^{-5}$$

$$\phi_{0}^{B_{s}K}(t;t_{0}) = \sqrt{\frac{\eta^{B_{s}K}}{16\pi}} \left(\frac{t_{cut} - t}{t_{cut} - t_{0}}\right)^{\frac{1}{4}} \left(\sqrt{t_{cut} - t} + \sqrt{t_{cut} - t_{0}}\right) \left(t_{+}^{B_{s}K} - t\right)^{\frac{1}{4}}$$

$$\left(\sqrt{t_{cut} - t} + \sqrt{t_{cut} - t_{-}^{B_{s}K}}\right)^{\frac{1}{2}} \left(\sqrt{t_{cut} - t} + \sqrt{t_{cut}}\right)^{-4}$$

$$(6.22)$$

$$\phi_{+}^{B\pi}(t;t_{0}) = \sqrt{\frac{\eta^{B\pi}}{48\pi}} \left(\frac{t_{cut} - t}{t_{cut} - t_{0}}\right)^{\frac{1}{4}} \left(\sqrt{t_{cut} - t} + \sqrt{t_{cut} - t_{0}}\right) \left(t_{+}^{B\pi} - t\right)^{\frac{3}{4}}$$

$$\left(\sqrt{t_{cut} - t} + \sqrt{t_{cut} - t_{-}^{B\pi}}\right)^{\frac{3}{2}} \left(\sqrt{t_{cut} - t} + \sqrt{t_{cut}}\right)^{-5}$$

$$\phi_{0}^{B\pi}(t;t_{0}) = \sqrt{\frac{\eta^{B\pi}}{16\pi}} \left(\frac{t_{cut} - t}{t_{cut} - t_{0}}\right)^{\frac{1}{4}} \left(\sqrt{t_{cut} - t} + \sqrt{t_{cut} - t_{0}}\right) \left(t_{+}^{B\pi} - t\right)^{\frac{1}{4}}$$

$$\left(\sqrt{t_{cut} - t} + \sqrt{t_{cut} - t_{-}^{B\pi}}\right)^{\frac{1}{2}} \left(\sqrt{t_{cut} - t} + \sqrt{t_{cut}}\right)^{-4}$$

$$(6.24)$$

6.6.1 Method

This method makes use of the shared unitarity constraint between the two decays. For each resampling of our form factor data (for both decays, where the resampling is independent for each decay), we perform a simultaneous optimization of the coefficients for all form factor curves given the unitarity constraint.

Practically, this extends our squared residual we wish to minimize,

$$\chi^{2} = \left[\left(\vec{F_{calc}} - \vec{F_{lattice}} \right)^{T} M_{cov}^{-1} \left(\vec{F_{calc}} - \vec{F_{lattice}} \right) \right]^{B\pi}$$
 (6.25)

$$+ \left[\left(\vec{F_{calc}} - \vec{F_{lattice}} \right)^T M_{cov}^{-1} \left(\vec{F_{calc}} - \vec{F_{lattice}} \right) \right]^{B_s K}, \tag{6.26}$$

where the unitarity constraint for each form factor now has contributions from both decays:

$$\sum_{n=0}^{\infty} |a_n^{(B\pi)}|^2 + \sum_{i,j=0}^{\infty} a_i^{(B_sK)} \langle z^i \, | \, z^j \rangle_{\alpha} a_j^{(B_sK)} \le 1$$
 (6.27)

The $\chi^2/(\text{d.o.f.})$ for this combined fit is 2.25 with a corresponding P-value of 0.06.

6.6.2 Comparison with single decay

Figures 6.5 -6.8 show the distribution of coefficients, a_i , when fitting each decay separately and together for $B \to \pi \ell \nu$ and $B_s \to K \ell \nu$, respectively, as well as their Cumulative Density Functions (CDF). Here i=0,1,2 correspond to the coefficients for f_0 and the rest are for f_+ .

In both cases, we perform the two-sample Kolmogorov-Smirnov test to calculate the P-value associated with both sets of coefficients coming from the same unknown distribution. As, for each decay, we are looking at 5 separate coefficients, we adjust our P-value threshold in the same way as in Section 6.5.

The results of these K-S tests indicate that the two sets of coefficients are consistent with the same underlying distribution, giving evidence that the two-decay fitting method does not impact the fitting for these decays. This can be expected from the sums of squared coefficients given in 6.1, as each for each decay the sum never goes above 0.5 for any of the 10000 resamples. As a result, the combined fit will not combine to be greater than 1, and so the unitarity constraint plays no part in the fitting procedure. It is possible this combined fit provides a stronger constraint for other decays.

Histograms of BPi Coefficients

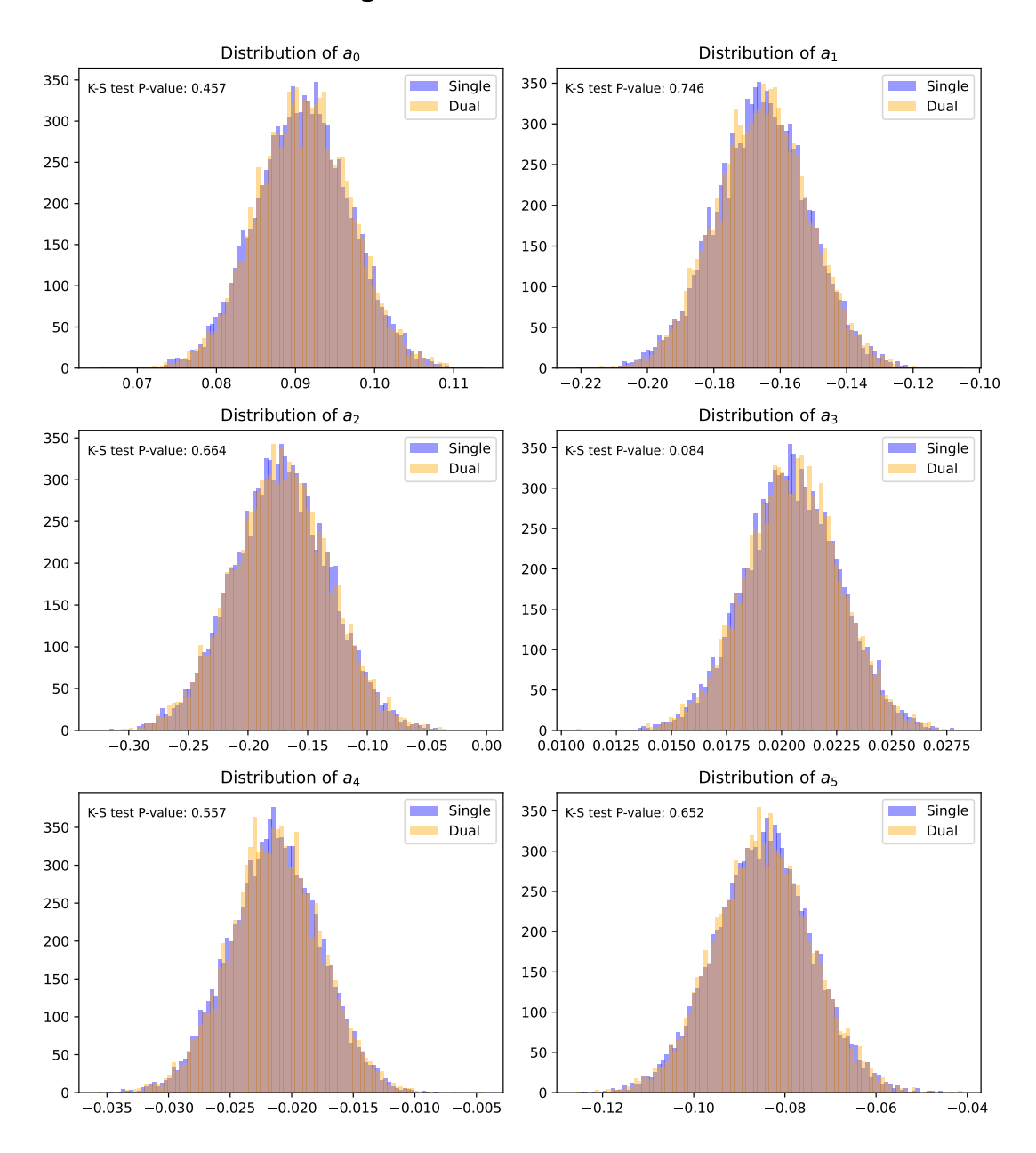


FIGURE 6.5: Distribution of BPi coefficients for single and dual (2-decay) fitting methods.

Histograms of BPi Coefficients

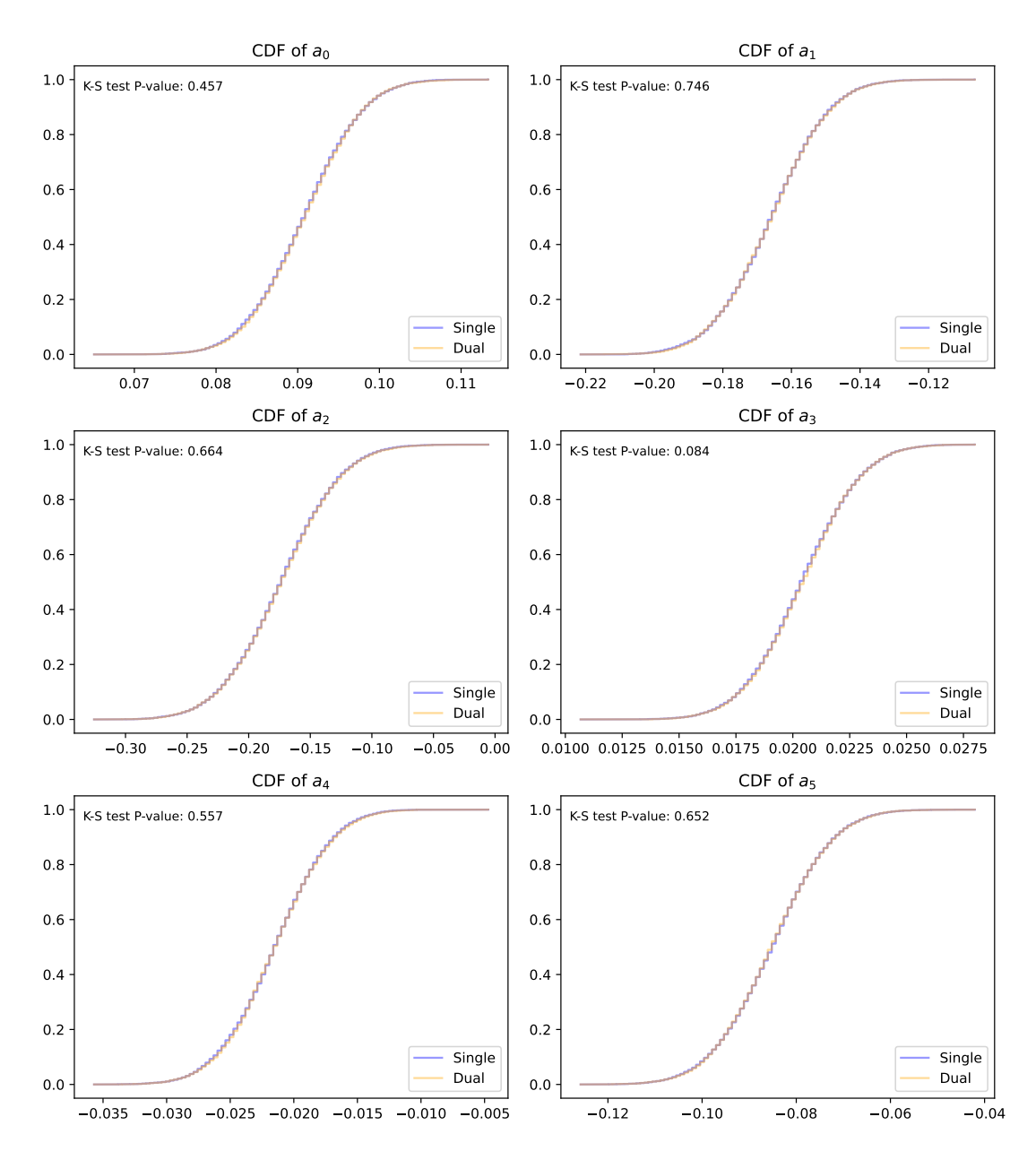


FIGURE 6.6: CDF of BPi coefficients for single and dual (2-decay) fitting methods.

Histograms of BsK Coefficients

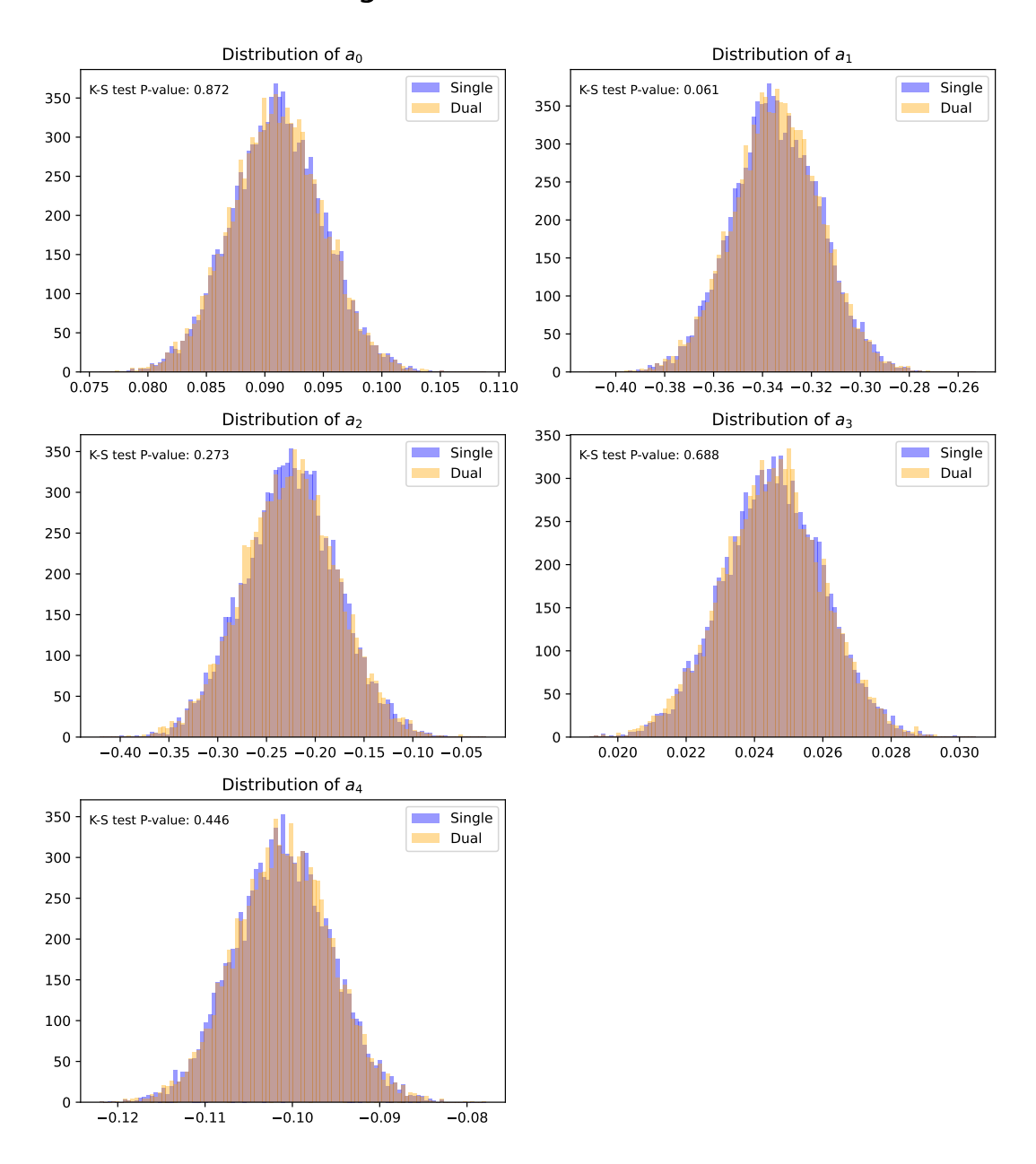


FIGURE 6.7: Distribution of BsK coefficients for single and dual (2-decay) fitting methods.

Histograms of BsK Coefficients

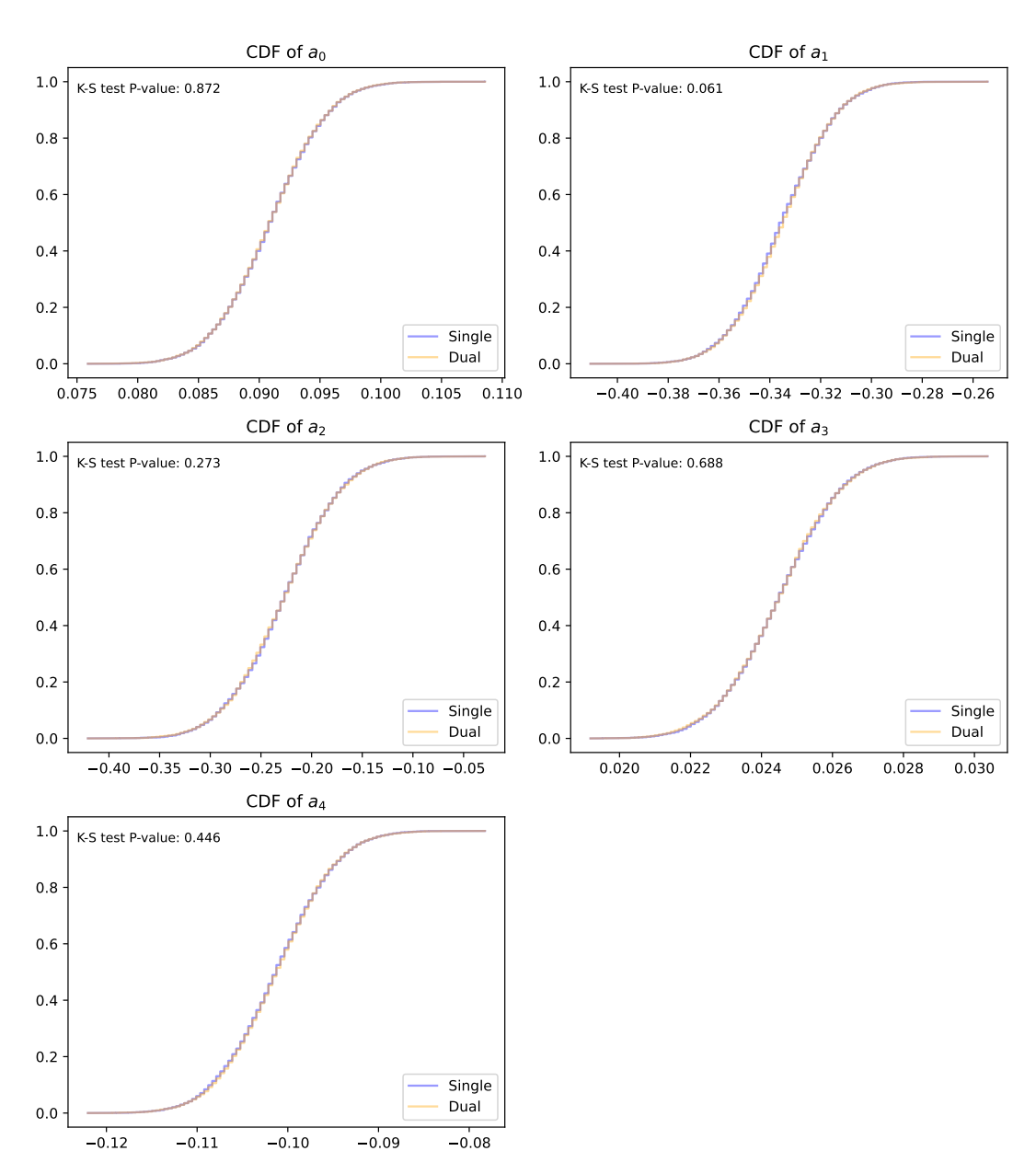


FIGURE 6.8: CDF of BsK coefficients for single and dual (2-decay) fitting methods.

6.7 Extracting V_{ub}

6.7.1 $B \rightarrow \pi \ell \nu$

For a theory-only fit, our squared residual, χ^2 (note that this is not the same χ as the susceptibility) is given by:

$$\chi_{lattice}^{2} = \left(\vec{F_{calc}} - \vec{F_{lattice}}\right)^{T} M_{cov}^{-1} \left(\vec{F_{calc}} - \vec{F_{lattice}}\right)$$
(6.28)

Where \vec{F}_{calc} are the values of the form factors (f_0 and f_+) calculated from the coefficients, $\vec{F}_{lattice}$ are the resampled form factor values from the lattice data, and M_{cov} is the covariance matrix of the lattice form factor values.

We may extend our χ^2 to include the experimental data:

$$\chi^{2} = \left(\vec{F_{calc}} - \vec{F_{lattice}}\right)^{T} M_{cov,latt}^{-1} \left(\vec{F_{calc}} - \vec{F_{lattice}}\right) + \left(\vec{D_{calc}} - \vec{D_{exp}}\right)^{T} M_{cov,exp}^{-1} \left(\vec{D_{calc}} - \vec{D_{exp}}\right)$$

$$(6.29)$$

Here we are optimizing the coefficients of z-fit parametrization as well as V_{ub} , and from these parameters, we calculate the Differential Decay Rate and integrate numerically over the q^2 bins given by the experiment (\vec{D}_{calc}). $M_{cov,exp}$ is the total covariance matrix of the differential decay rate bins for the experiment. This can be extended by adding in data from multiple experiments, each with its own contribution to the χ^2 .

Combined fits of lattice and experimental data are done through "BFGS" parameter optimization, where the function being minimised is the total χ^2 . This is performed using SciPy's optimize.minimize function on the chi-squared formed using the input form factor data and the binned DR from experiment. This produces the optimal set of coefficients and V_{ub} alongside the χ^2 value and the Hessian matrix. The covariance matrix of the fitted parameters is given by twice the inverse Hessian matrix.

For $B \to \pi \ell \nu$, we have 4 experimental datasets that we can use to obtain V_{ub} . Table 6.2 shows the V_{ub} , $\chi^2/\text{d.o.f.}$ and the P-value for each experiment. This is also done for the fit for all experimental datasets simultaneously, and for all experiments besides BaBar2010. Figure 6.9 shows why excluding BaBar2010 leads to a better $\chi^2/\text{d.o.f.}$, as the shape of the BaBar2010 differential decay rate bins is an outlier from the other experiments. These results are consistent with those from JLQCD using a BCL parametrization [80].

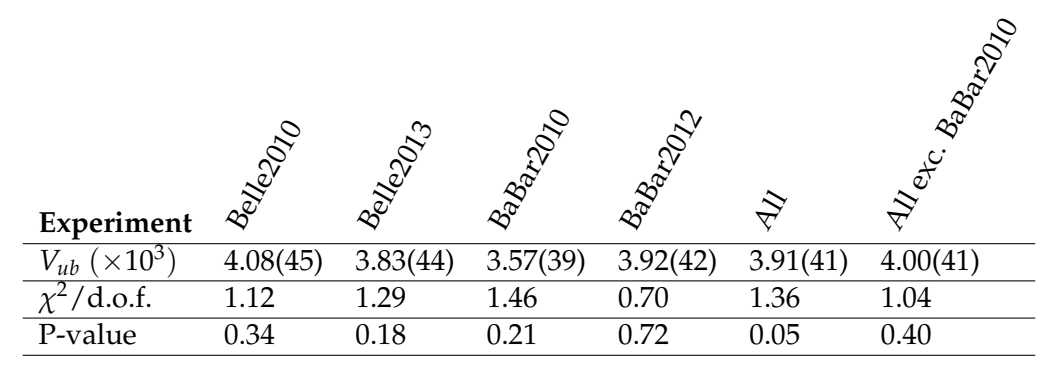


TABLE 6.2: The V_{ub} , $\chi^2/\text{d.o.f.}$, and P-values for each experiment and the combined fits.

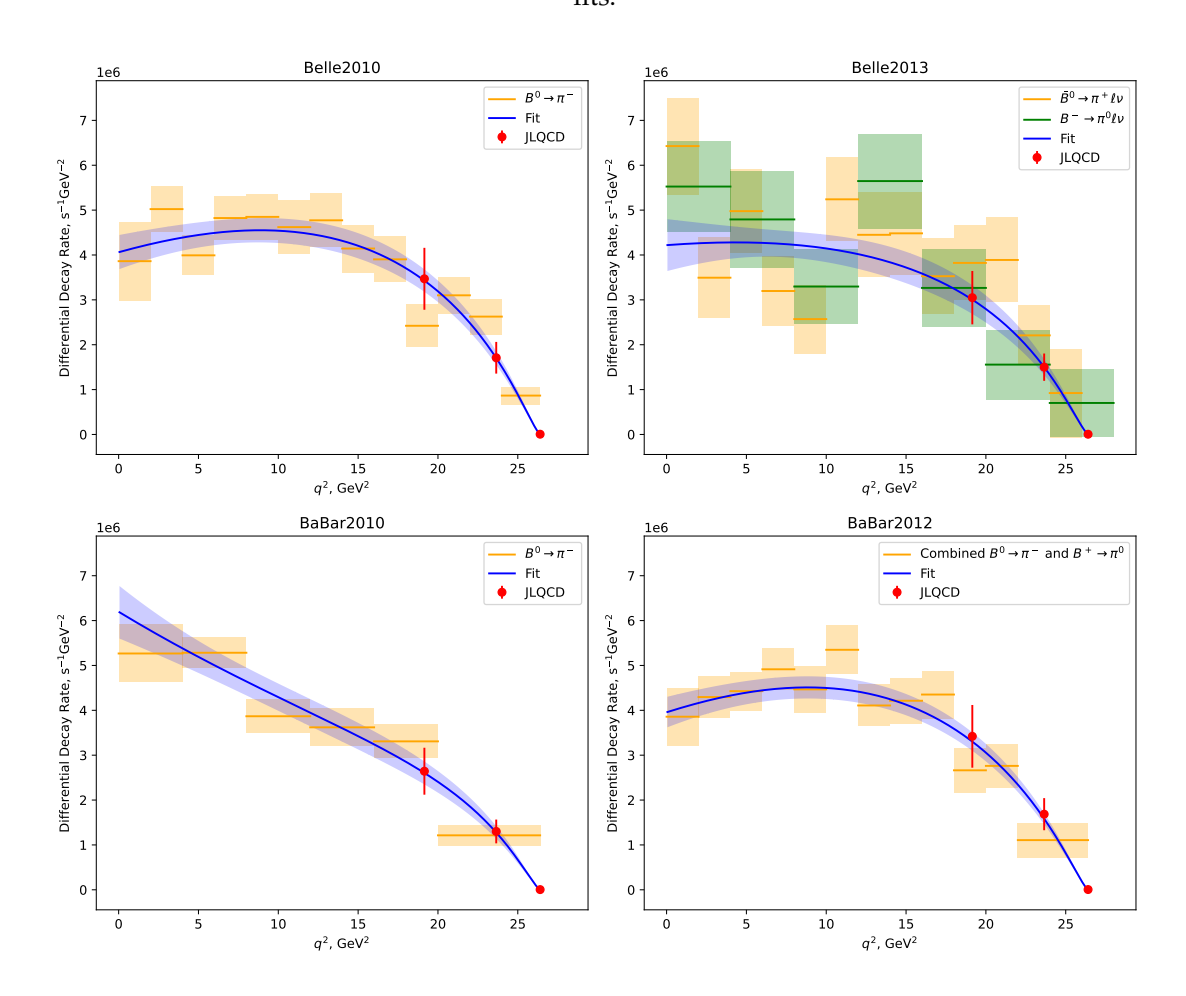


FIGURE 6.9: Differential decay rate from coefficients (Blue) plotted alongside experimental bins (yellow/green) and differential decay rate values from lattice form factor values (red).

6.7.2 $B_s \to K\ell\nu$

For $B_s \to K\ell\nu$, the experimental results are very limited. We use the LHCb measurements [66] of

$$R_{\rm BF} = \frac{\mathcal{B}(B_s^0 \to K^- \mu^+ \nu_\mu)}{\mathcal{B}(B_s^0 \to D_s^- \mu^+ \nu_\mu)}.$$
 (6.30)

Which are measured over two bins, low $(q^2 \le 7GeV^2)$ and high $(q^2 > 7GeV^2)$:

$$R_{BF}^{\text{low}} = 1.66(08)(09) \times 10^{-3}$$

 $R_{BF}^{\text{high}} = 3.25(21)\binom{+18}{-19} \times 10^{-3}$ (6.31)

We can use this information alongside the branching ratio,

$$\mathcal{B}(B_s^0 \to D_s^- \mu^+ \nu_\mu) = 2.49(12)(21) \times 10^{-2},$$
 (6.32)

and the B_s^0 lifetime, $\tau_{B_s^0} = 1.520(5) \times 10^{-12}$ s, to extract V_{ub} using the expression:

$$|V_{ub}| = \sqrt{\frac{R_{BF}^{\text{bin}}\mathcal{B}(B_s^0 \to D_s^- \mu^+ \nu_\mu)}{\tau_{B_s^0} \bar{\Gamma}^{\text{bin}}(B_s \to K\ell\nu)}}$$
(6.33)

This is the procedure presented in the 2023 RBC/UKQCD collaboration paper for $B_s \to K \ell \nu$ [88].

To extract the best full range V_{ub} value, we take the weighted mean of the 'low' and 'high' bin results. This weighted mean is calculated by calculating the covariance matrix for V_{ub}^{low} and V_{ub}^{high} , M, and optimising θ such that it minimises

$$\chi^{2}(\theta) = \left[\begin{pmatrix} V_{ub}^{\text{low}} \\ V_{ub}^{\text{high}} \end{pmatrix} - \begin{pmatrix} \theta \\ \theta \end{pmatrix} \right] M^{-1} \left[\begin{pmatrix} V_{ub}^{\text{low}} \\ V_{ub}^{\text{high}} \end{pmatrix} - \begin{pmatrix} \theta \\ \theta \end{pmatrix} \right]$$
(6.34)

The uncertainty in this result is given by the range of V_{ub} at $\chi^2_{min} + 1$, illustrated in Figure 6.10. Table 6.3 shows the low and high range values using the corresponding experimental results, alongside the weighted mean. The final $\chi^2/\text{d.o.f.} = 1.13$, which has a corresponding p-value of 0.337.

Range	$V_{ub} \times 10^3$
Low	7.51(2.12)
High	4.17(41)
Weighted Mean	3.66(31)

TABLE 6.3: V_{ub} calculated for low and high range experimental results from LHCb[66], alongside the weighted mean value. Lattice form factor results used are from the RBC/UKQCD collaboration[88].

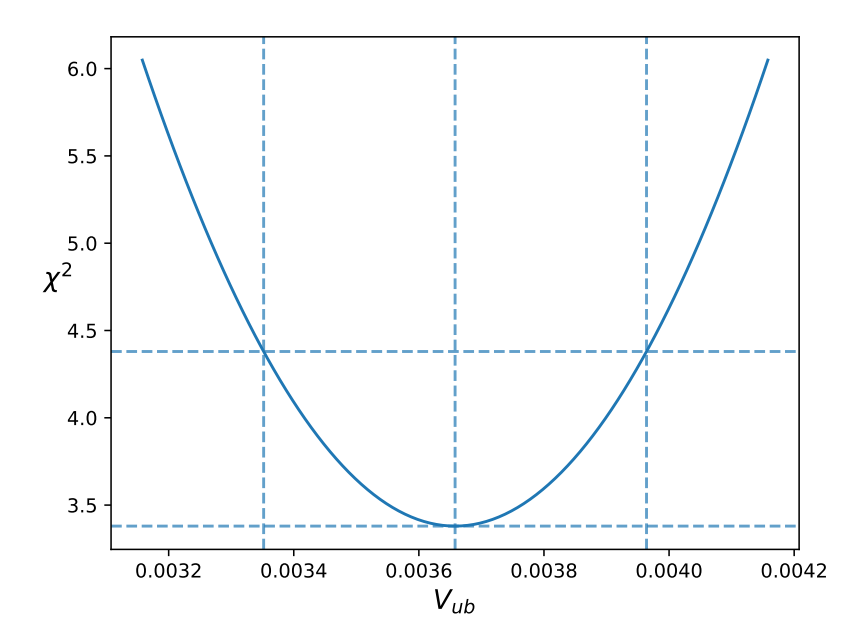


Figure 6.10: χ^2 optimisation of the V_{ub} weighted mean.

Chapter 7

Dispersive Matrix method

7.1 The Dispersive Matrix

The dispersive bounds method aims to provide a model-independent approach to extrapolate from lattice simulations (low-recoil, high q^2) form factor results into the high-recoil (low- q^2) area of the allowed kinematic region using our dispersion relations. It provides bounds without using any parametrisation or series expansion of the form factors [24, 25, 26, 36, 47, 78, 82, 84].

From Equation 5.11, our familiar dispersion relation:

$$\frac{1}{2\pi i} \int_{|z|=1} \frac{dz}{z} |B(z)\phi(z)f(z)|^2 \le \chi \tag{7.1}$$

We define the inner product

$$\langle g \mid h \rangle = \frac{1}{2\pi i} \oint_{|z|=1} \frac{dz}{z} \bar{g}(z) h(z), \tag{7.2}$$

so, using the positivity of the inner product, we may rewrite eq 7.1 as

$$0 \le \langle B\phi f \mid B\phi f \rangle \le \chi. \tag{7.3}$$

It is useful to define $g_t(z)$ as

$$g_t(z) \equiv \frac{1}{1 - \bar{z}(t)z} \quad , \tag{7.4}$$

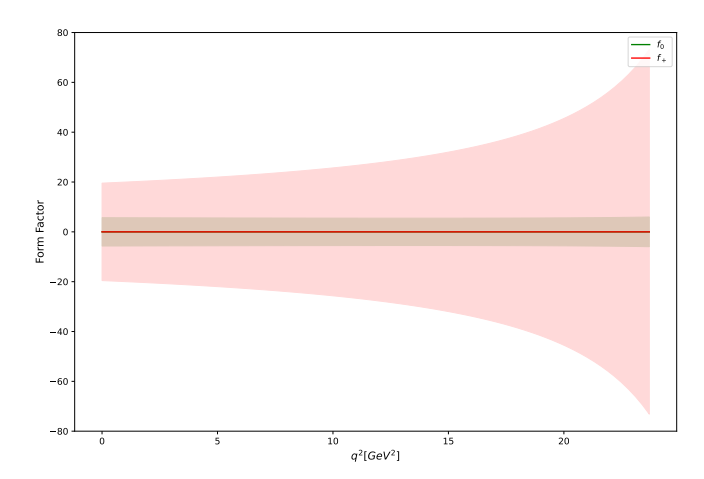


FIGURE 7.1: Form factor bounds calculated using the DM method for $B_s \to K \ell \nu$ using unitarity only.

so that the inner product, $\langle g_t | B\phi f \rangle = B(t)\phi(t)f(t)$ ($g_t(z)$ picks out the value f(t)). Consequently

$$\langle g_{t_m} \mid g_{t_l} \rangle = \frac{1}{1 - z(t_l) \, \bar{z}(t_m)}. \tag{7.5}$$

From eq 7.3 we may construct a 2x2 Gram matrix,

$$\begin{pmatrix}
\langle B\phi f \mid B\phi f \rangle & \langle B\phi f \mid g_t \rangle \\
\langle g_t \mid B\phi f \rangle & \langle g_t \mid g_t \rangle
\end{pmatrix},$$
(7.6)

which can be used to impose a loose constraint on the form factors:

This constraint comes from the non-negativity of the matrix determinant. The bounds from unitarity alone can be seen in Figure 7.1. This is the form of the DM method first developed by Bourelly et al. [36] (which uses a procedure from Okubo to exploit the analyticity of the form factors to establish bounds on their values [24, 25, 26]). Earlier work by Ling-Fong and Pagels establish bounds for Kaon semileptonic decays using information from the dispersion relation [23, 22].

The dispersive bounds method may impose a stricter constraint by also making use of known form factor values, as was pioneered by Lellouch for $B \to \pi \ell \nu$ [47]. To do this, we construct an extended Gram matrix, M:

$$\mathbf{M} = \begin{pmatrix} \langle B\phi f \mid B\phi f \rangle & \langle B\phi f \mid g_{t} \rangle & \langle B\phi f \mid g_{t_{1}} \rangle & \cdots & \langle B\phi f \mid g_{t_{n}} \rangle \\ \langle g_{t} \mid B\phi f \rangle & \langle g_{t} \mid g_{t} \rangle & \langle g_{t} \mid g_{t_{1}} \rangle & \cdots & \langle g_{t} \mid g_{t_{n}} \rangle \\ \langle g_{t_{1}} \mid B\phi f \rangle & \langle g_{t_{1}} \mid g_{t} \rangle & \langle g_{t_{1}} \mid g_{t_{1}} \rangle & \cdots & \langle g_{t_{1}} \mid g_{t_{n}} \rangle \\ \vdots & \vdots & \vdots & \vdots & \vdots \\ \langle g_{t_{n}} \mid B\phi f \rangle & \langle g_{t_{n}} \mid g_{t} \rangle & \langle g_{t_{n}} \mid g_{t_{1}} \rangle & \cdots & \langle g_{t_{n}} \mid g_{t_{n}} \rangle \end{pmatrix}$$
(7.7)

Here t_i denote the q^2 values for the input lattice form factor values, and t is the value of q^2 for which we wish to constrain the form factor. We introduce the notation $M^{\{(i_1,j_1),(i_2,j_2),\ldots\}}$, representing the matrix M with rows i_1,i_2,\ldots and columns j_1,j_2,\ldots removed. We will name the matrix $M^{\{(0,0)\}}$, G.

Due to the improvement in lattice data, this method has become more popular in recent years. This followed a paper by Di Carlo et al. [78], which was the first analysis using the DM method using only lattice inputs (previously the susceptibilities, χ , had been calculated perturbatively), and also improved the implementation of the kinematic constraint. The procedure and notation used in this paper is the basis of the DM explanation described in this section. Since then, this method has been used to obtain form factor information for many decays (see papers[82, 79, 83, 85, 89], for example).

Due to the positivity of the inner product, matrix M is positive semi-definite. Using this, we may write the determinant of M as

$$\langle B\phi f | B\phi f \rangle \det(G) - \sum_{i,j=0}^{n} (B\phi f)_{i} (B\phi f)_{j} (-1)^{i+j} \det(G^{\{(i,j)\}}) \ge 0$$
 (7.8)

Here $t_0 = t$. From eq 7.3 we know we may replace $\langle B\phi f | B\phi f \rangle$ with the susceptibility in the above inequality and, as G is also positive semi-definite, will only increase the left-hand side (or leave it unchanged). Doing this gives us

$$\chi \det(G) - \sum_{i,j=0}^{N} (B\phi f)_i (B\phi f)_j (-1)^{i+j} \det(G^{\{(i,j)\}}) \ge 0$$
 (7.9)

Rearranging and grouping powers of f_t gives

$$\gamma - 2\beta (B\phi f)_t - \alpha (B\phi f)_t^2 \ge 0, \tag{7.10}$$

where

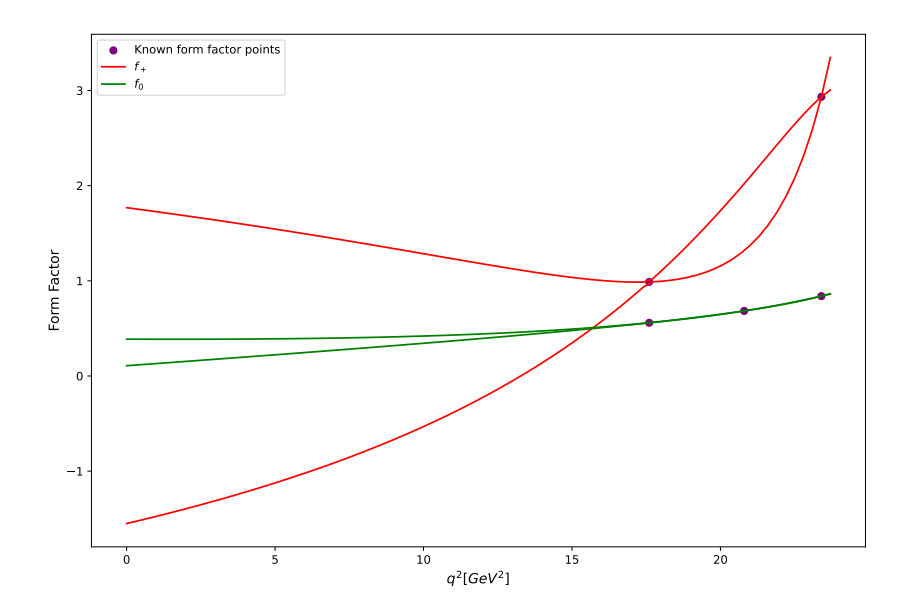


FIGURE 7.2: Example form factor bounds calculated using the DM method for $B_s \to K\ell\nu$ with the unitarity constraint and a set of form factor points. Here, the curves plotted represent the top and the bottom of the region allowed by unitarity.

$$\alpha = \det(G^{\{(0,0)\}}) \tag{7.11}$$

$$\beta = \sum_{j=1}^{n} (B\phi f)_{j} (-1)^{j} \det(G^{\{(0,j)\}})$$
(7.12)

$$\gamma = \chi \det(G) - \sum_{i,j=1}^{n} (B\phi f)_{i} (B\phi f)_{j} (-1)^{i+j} \det(G^{\{(i,j)\}}). \tag{7.13}$$

The bounds on each form factor are then given by

$$\frac{-\beta - \sqrt{\beta^2 + \alpha \gamma}}{\alpha} \le (B\phi f)_t \le \frac{-\beta + \sqrt{\beta^2 + \alpha \gamma}}{\alpha} \tag{7.14}$$

It can be shown that the discriminant, Δ , is equal to $\det(G)\det(M^{\{(1,1)\}})$. It is worth noting that $\det(G) \geq 0$ (provided t and all t_i are distinct) and $\det(M^{\{(1,1)\}}) \geq 0$ if $f(t_i)$ themselves satisfy unitarity.

It is worth noting that when calculating the bounds at a t value coinciding with an input form factor value, t_j , matrix G becomes singular, meaning the discriminant becomes zero, and we recover the form factor value $f(t_j)$ exactly. Figure 7.1 shows example bounds calculated from input form factor points.

7.1.1 Bootstrapping Procedure

We now know how to generate bounds for a given set of form factor inputs and susceptibilities using the dispersion relations.

In addition to this unitarity constraint, we also have a kinematical constraint on our two form factors f_0 and f_+ . This states that the two form factors must have the same value at t=0: $f_0(0)=f_+(0)$. This is apparent from the form factor decomposition in equation 2.71, as in the limit of $q^2 \to 0$ the two form factors must tend to the same value to keep the matrix element finite.

As our lattice form factors are not precisely known, we resample the form factors using a multivariate normal distribution from their covariance matrix, giving N_{boot} input data sets (I shall refer to this as the 'outer bootstrap').

From these form factor values we calculate $\det(M^{\{(1,1)\}})$, removing any bootstrap events that don't satisfy unitarity (for the decays in this work, this never occurred). We then calculate the bounds at t=0 for both form factors and discard any bounds that do not satisfy the kinematic constraint (the bounds at t=0 do not overlap). This leaves us with \tilde{N}_{boot} events.

For a given bootstrap event the form factors can take any value in the overlap region at t=0, from f_{lo}^* to f_{up}^* (being the bottom and top of the overlap region, respectively). For each event we sample N_0 form factor values (uniform distribution). For this inner bootstrap of N_0 form factor values we repeat the form factor bounds procedure by extending our matrix M, treating this value as an additional input form factor input value, $\langle B\phi f \mid g_{t_0} \rangle$. Our extended matrix, M_C for each form factor takes the form

$$\mathbf{M_{C}} = \begin{pmatrix} \langle B\phi f \mid B\phi f \rangle & \langle B\phi f \mid g_{t} \rangle & \langle B\phi f \mid g_{t_{1}} \rangle & \cdots & \langle B\phi f \mid g_{t_{n}} \rangle & \langle B\phi f \mid g_{t_{0}} \rangle \\ \langle g_{t} \mid B\phi f \rangle & \langle g_{t} \mid g_{t} \rangle & \langle g_{t} \mid g_{t_{1}} \rangle & \cdots & \langle g_{t} \mid g_{t_{n}} \rangle & \langle g_{t} \mid g_{t_{0}} \rangle \\ \langle g_{t_{1}} \mid B\phi f \rangle & \langle g_{t_{1}} \mid g_{t} \rangle & \langle g_{t_{1}} \mid g_{t_{1}} \rangle & \cdots & \langle g_{t_{1}} \mid g_{t_{n}} \rangle & \langle g_{t_{1}} \mid g_{t_{0}} \rangle \\ \vdots & \vdots & \vdots & \vdots & \vdots & \vdots \\ \langle g_{t_{n}} \mid B\phi f \rangle & \langle g_{t_{n}} \mid g_{t} \rangle & \langle g_{t_{n}} \mid g_{t_{1}} \rangle & \cdots & \langle g_{t_{n}} \mid g_{t_{n}} \rangle & \langle g_{t_{n}} \mid g_{t_{0}} \rangle \\ \langle g_{t_{0}} \mid B\phi f \rangle & \langle g_{t_{0}} \mid g_{t} \rangle & \langle g_{t_{0}} \mid g_{t_{1}} \rangle & \cdots & \langle g_{t_{0}} \mid g_{t_{n}} \rangle & \langle g_{t_{0}} \mid g_{t_{0}} \rangle \end{pmatrix}$$
 (7.15)

From this we find the bounds, $(f_{lo}^1, f_{lo}^2, ..., f_{lo}^{N_0})$ and $(f_{up}^1, f_{up}^2, ..., f_{up}^{N_0})$ for each form factor at any value of t for each of the N_0 inner bootstraps. As the form factor is allowed to take any value in the overlap region, the extremal bounds at any value of t are taken from the inner bootstrap events:

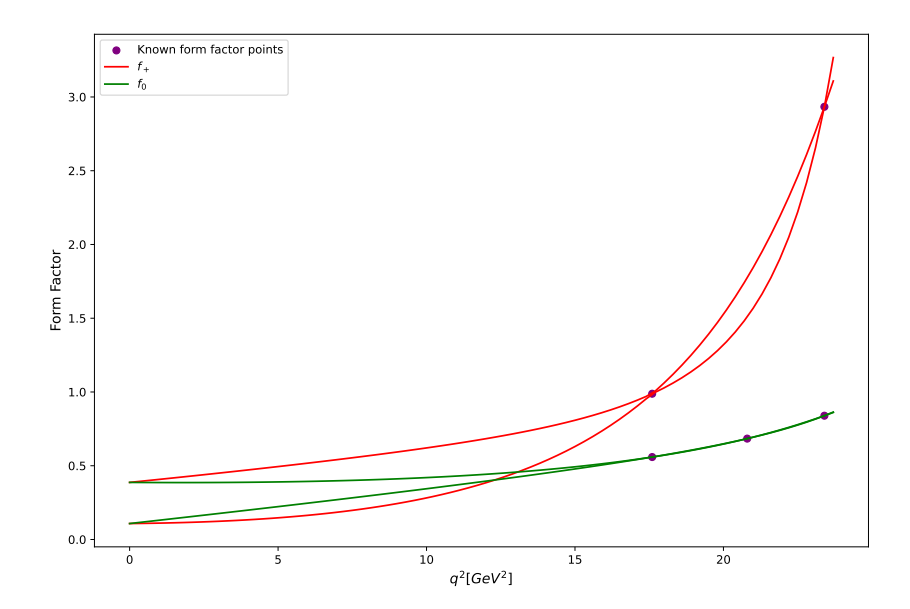


FIGURE 7.3: Example form factor bounds calculated using the DM method for $B_s \to K\ell\nu$ with the unitarity and kinematic constraints and a set of form factor points. Here, the curves plotted represent the top and the bottom of the region allowed by unitarity. This plot is for a single resample of form factors, and so, has no errors.

$$\bar{f}_{lo} = \min(f_{lo}^1, f_{lo}^2, ..., f_{lo}^{N_0})$$
(7.16)

$$\bar{f}_{up} = \max(f_{up}^1, f_{up}^2, ..., f_{up}^{N_0})$$
 (7.17)

Figure 7.3 shows an example set of form factor bounds that have been calculated using both the unitarity and kinematic constraints.

Doing this for all \tilde{N}_{boot} bootstrap events gives us \tilde{N}_{boot} sets of upper and lower bounds for each form factor (denoted with the subscripts up and lo, respectively) at each chosen value of t. From this we can calculate the average values, $f_{lo/up}(t)$, standard deviations, $\sigma_{lo/up}(t)$, and covariance matrix, $\rho_{lo,up}(t)$ (this is the covariance between lower and upper bound values):

$$f_{lo/up}(t) = \frac{1}{\tilde{N}_{hoot}} \sum_{i=1}^{\tilde{N}_{boot}} \bar{f}_{lo/up}^{i}, \tag{7.18}$$

$$\sigma_{lo/up}^{2}(t) = \frac{1}{\tilde{N}_{boot} - 1} \sum_{i=1}^{\tilde{N}_{boot}} \left[\bar{f}_{lo/up}^{i}(t) - f_{lo/up}(t) \right]^{2}, \tag{7.19}$$

$$\rho_{lo,up}(t) = \rho_{up,lo}(t) = \frac{1}{\tilde{N}_{boot} - 1} \sum_{i,j=1}^{\tilde{N}_{boot}} \left[\bar{f}_{lo}^{i}(t) - f_{lo}(t) \right] \left[\bar{f}_{up}^{j}(t) - f_{up}(t) \right]$$
(7.20)

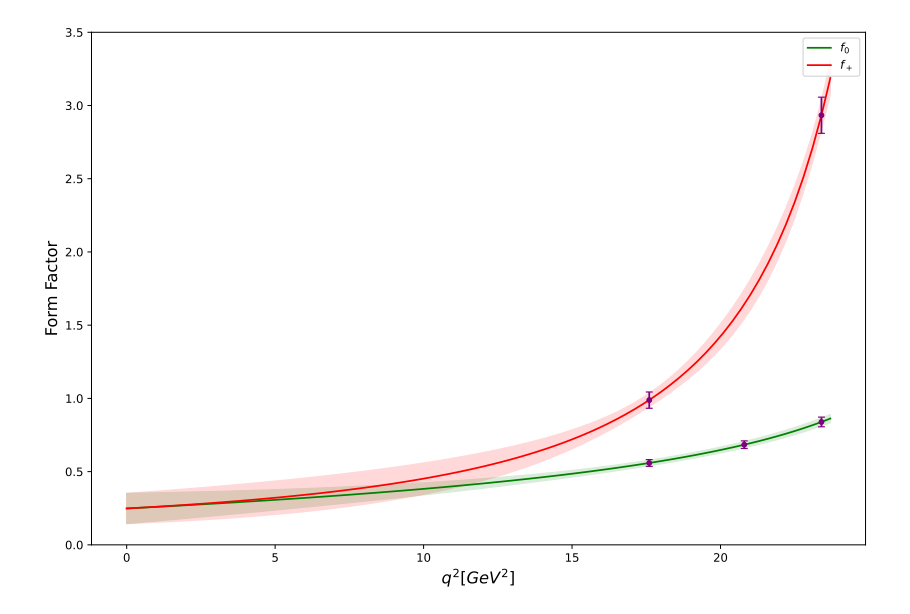


FIGURE 7.4: Form factor bounds calculated using the DM method over 2000 bootstrap events for $B_s \to K \ell \nu$ with both the unitarity and kinematic constraints. Synthetic form factor data is from the RBC/UKQCD collaboration [88]

We may combine the upper and lower bound results to calculate the average form factor values and standard deviations:

$$f(t) = \frac{f_{\rm lo}(t) + f_{\rm up}(t)}{2},\tag{7.21}$$

$$\sigma_f^2(t) = \frac{1}{12} \left[f_{\rm up}(t) - f_{\rm lo}(t) \right]^2 + \frac{1}{3} \left[\sigma_{\rm lo}^2(t) + \sigma_{\rm up}^2(t) + \rho_{\rm lo, up}(t) \right]. \tag{7.22}$$

Figure 7.4 shows bounds calculated using this procedure using input form factor values at $q^2 = 17.6$ and $23.4 GeV^2$ for f_0 and $q^2 = 17.6$, 20.8 and $23.4 GeV^2$ for f_+ over 2000 bootstrap events (again, using synthetic form factor data from the RBC/UKQCD collaboration [88]). Here, central values and errors shown are calculated using Equations 7.21 and 7.22.

7.2 Improving Numerical Stability

We may express the bounds in Equation 7.14 as

$$(B\phi f)_{lo/up}(t) = \frac{-\beta \mp \sqrt{\beta^2 + \alpha \gamma}}{\alpha}$$
 (7.23)

Numerical precision errors often arise from the formulation of the bounds above, as terms in the discriminant can become numerically tiny.

This can be mitigated by modifying the matrix M, which can be written as

$$M = \begin{pmatrix} \langle B\phi f \mid B\phi f \rangle & \overrightarrow{B\phi f^T} \\ \overrightarrow{B\phi f} & G \end{pmatrix}, \quad \overrightarrow{B\phi f} = (B(t)\phi(t)f(t), (B\phi f)_1, \dots (B\phi f)_n)^T. \quad (7.24)$$

We diagonalise the sub-matrix, G, $G = U^T \Lambda U$, where $UU^T = 1$ and $\Lambda = \text{diag}(\lambda_0, \dots, \lambda_n)$ (I thank Nikolai Husung for demonstrating this [81]).

We construct the modified matrix, M':

$$M' = \begin{pmatrix} \langle B\phi f \mid B\phi f \rangle & \vec{f}'^T \\ \vec{f}' & \Lambda \end{pmatrix}, \quad \overrightarrow{f}' = U \overrightarrow{B\phi f}. \tag{7.25}$$

Once again, M' is positive semi-definite, and we may use the determinant to find the bounds of the form factors. Collecting terms according to their dependence on f_0 gives modified α , β and γ coefficients:

$$\alpha' = \sum_{i=0}^{n} \frac{u_{i0}u_{i0}}{\lambda_i}, \quad \beta' = \sum_{i=0}^{n} \frac{u_{i0}\hat{f}_i}{\lambda_i}, \quad \gamma' = \langle B\phi f \mid B\phi f \rangle - \sum_{i=0}^{n} \frac{\hat{f}_i^2}{\lambda_i}$$
 (7.26)

where \hat{f}_i is

$$\hat{f}_i = \sum_{j>0} u_{ij} (B\phi f)_j. {(7.27)}$$

The discriminant may now be written as

$$\beta'^{2} + \alpha'\gamma' = \langle B\phi f \mid B\phi f \rangle + \sum_{i < j, i=0, j=1}^{n} \frac{1}{\lambda_{i}\lambda_{j}} \left[2u_{i0}u_{j0}\hat{f}_{i}\hat{f}_{j} - u_{i0}^{2}\hat{f}_{j}^{2} - u_{j0}^{2}\hat{f}_{i}^{2} \right].$$
 (7.28)

By re-writing in this way the largest and smallest terms have canceled out. Additionally, by performing the sum from the smallest eigenvalues to the largest we cancel most of the contribution from large terms before summing smaller ones.

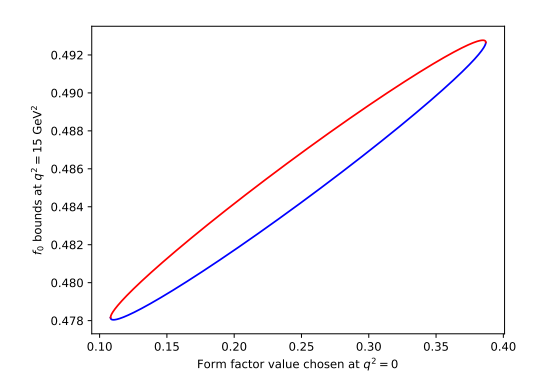
Implementing this more numerically stable approach drastically reduces the number of false-negative unitarity-violating bootstrap events (from around 3% of bounds calculations to almost none). These occur as bounds calculated using a synthetic data point at the top/bottom of the overlap range will have a zero or near-zero

discriminant, and any numerical instability will result in a significant portion of these coming out as negative.

7.3 Sampling Across the Overlap Region

The method outlined by Di Carlo et al. in [78] to find the extremal bounds within a bootstrap event is to perform an inner bootstrap that randomly and uniformly samples, N_0 times, across the bound at $q^2 = 0$ and select the maximum upper bounds and minimum lower bound (this implementation of the kinematic constraint differs from that first done by Lellouch [47]).

It seems logical that it is sufficient to only look at the top and bottom of the overlap region, as one would expect that the highest/lowest synthetic data point would correspond to the highest/lowest bounds. To test this, we may move our synthetic data point across the overlap region and see how the bounds change for each form factor. Figure 7.5 shows the relationship in a typical bootstrap event.



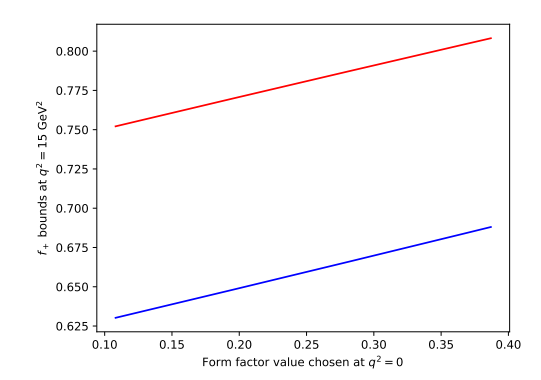


FIGURE 7.5: Form factor bounds for $B_s \to K\ell\nu$ calculated at $q^2 = 15~{\rm GeV}^2$ for an individual bootstrap event as the synthetic data point is moved over the overlap region at $q^2 = 0~{\rm GeV}^2$. f_0 is on the left and f_+ on the right. Here the red curve signifies the top of the bounds, and the blue curve is the bottom.

The relationship is almost monotonic, with a slight inversion near the very top and bottom of the bound in the example for f_0 [47].

The extremum does not lie at the top/bottom of the overlap region for a particular form factor if this form factor dictates the overlap region at that point (i.e. when the kinematical constraint is applied, the top of the overlap region is dictated by a particular form factor and so is the bottom). In this instance, we observe the extremum to be slightly away from the edge of the overlap. A more zoomed in plot of the f_0 bounds at the bottom of the overlap region can be seen in Figure 7.6. For the decays we are looking at it is always the case that f_0 dictates the bounds, as the unitarity

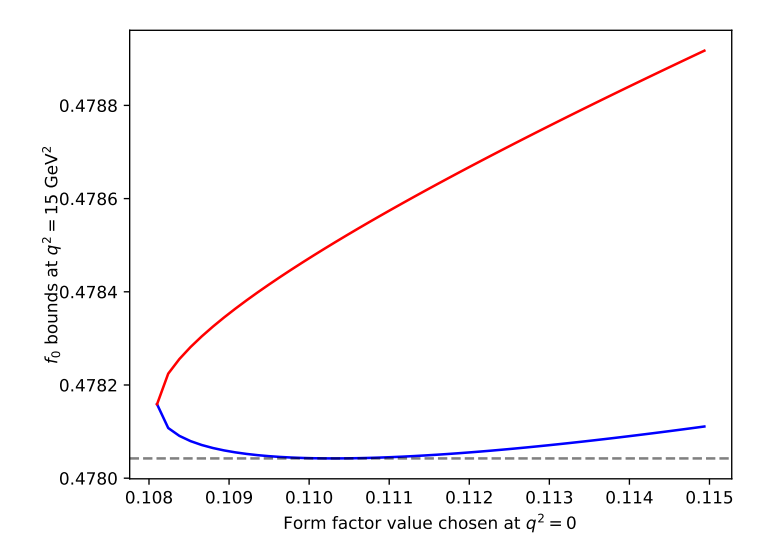


FIGURE 7.6: f_0 bounds at $q^2 = 15 \text{ GeV}^2$ for $B_s \to K\ell\nu$, as the synthetic data point is moved away from the bottom of the overlap region.

constraint gives much wider bounds for f_+ , and so the ellipse-like shape is cut on both ends, giving the monotonic behaviour we see for f_+ .

The difference between the extremal value and that from the top/bottom of the overlap region is very small. This, combined with the observation that most of the error in the final measurements comes from the variation in bootstrap events, indicates that looking at the top/bottom of the overlap region is sufficient until lattice measurements become much more precise.

If a more precise procedure is needed, one can instead use a minimisation algorithm such as SciPy's "optimize minimize scalar". For the "bounded" method between the bottom and top of the overlap region, and with default tolerance of 10^{-8} , the minimum and maximum bounds are found in 15-25 function evaluations, making it $10\times$ more expensive than just looking at the ends of the overlap region for just this part of the optimiser routine.

For a sample of 2000 bootstrap events in each case, we can compare the results from our approach looking at only the top and bottom of the overlap region, to the more precise approach using the algorithm to locate the exact minimum and maximum.

$q^2 \left(\text{GeV}^2 \right)$	$ f_0(q^2) _{\text{Top/Bot}}$	$f_+(q^2) _{\text{Top/Bot}}$	$\left f_0\left(q^2\right) \right _{\text{Min/Max}}$	$f_+(q^2) _{\mathrm{Min/Max}}$
5.0	0.306(71)	0.320(115)	0.305(70)	0.319(114)
10.0	0.381(42)	0.452(107)	0.381(41)	0.450(107)
15.0	0.486(23)	0.720(64)	0.485(22)	0.719(64)

TABLE 7.1: Means and uncertainties for the approach looking at only the top and bottom of the overlap region and when finding the minimum and maximum using the optimiser routine.

Table 7.1 shows that when looking at a large sample of bootstrap events, the results when using the optimiser are indiscernible from those when looking only at the top/bottom of the overlap region. If the method were sufficiently beneficial, for each bootstrap the bounds obtained would be notably wider, meaning the uncertainty in the form factor value would be consistently larger. We do not observe this for these results. Additionally, for a fixed computational budget, many more bootstrap events can be run if only the top and bottom are used. The precise approach may be used when calculating final results where computation time is available.

7.4 The DM method for two decays

We can express the dispersion relation for two-decays, given in Equation 6.20, as

$$\chi \ge \langle B\phi f \, | \, B\phi f \rangle^{B_s K} + \langle B\phi f \, | \, B\phi f \rangle^{B\pi}. \tag{7.29}$$

We shall now consider the case where we wish to use information from both decays to find bounds for $B_s \to K\ell\nu$ (which we will therefore refer to as the primary decay). The primary and secondary ($B \to \pi\ell\nu$) decays can be interchanged trivially. It is also easy to see that this method extends to any number of additional decays, which will all be treated identically to the secondary decay in the following procedure.

For the primary decay, we construct a Gram matrix:

$$\mathbf{M}_{P} = \begin{pmatrix} \langle B\phi f | B\phi f \rangle^{P} & \langle B\phi f | g_{t} \rangle^{P} & \langle B\phi f | g_{t_{1}} \rangle^{P} & \cdots & \langle B\phi f | g_{t_{n}} \rangle^{P} \\ \langle g_{t} | B\phi f \rangle^{P} & \langle g_{t} | g_{t} \rangle^{P} & \langle g_{t} | g_{t_{1}} \rangle^{P} & \cdots & \langle g_{t} | g_{t_{n}} \rangle^{P} \\ \langle g_{t_{1}} | B\phi f \rangle^{P} & \langle g_{t_{1}} | g_{t} \rangle^{P} & \langle g_{t_{1}} | g_{t_{1}} \rangle^{P} & \cdots & \langle g_{t_{1}} | g_{t_{n}} \rangle^{P} \\ \vdots & \vdots & \vdots & \vdots & \vdots \\ \langle g_{t_{n}} | B\phi f \rangle^{P} & \langle g_{t_{n}} | g_{t} \rangle^{P} & \langle g_{t_{n}} | g_{t_{1}} \rangle^{P} & \cdots & \langle g_{t_{n}} | g_{t_{n}} \rangle^{P} \end{pmatrix}$$

$$(7.30)$$

Here t_i denote the q^2 values for the input lattice form factor values, and t is the value of q^2 we wish to find the form factor bounds at. For the secondary decay, we construct an almost identical Gram matrix which only contains form factor information from the lattice:

$$\mathbf{M}_{S} = \begin{pmatrix} \langle B\phi f \mid B\phi f \rangle^{S} & \langle B\phi f \mid g_{t_{1}} \rangle^{S} & \cdots & \langle B\phi f \mid g_{t_{n}} \rangle^{S} \\ \langle g_{t_{1}} \mid B\phi f \rangle^{S} & \langle g_{t_{1}} \mid g_{t_{1}} \rangle^{S} & \cdots & \langle g_{t_{1}} \mid g_{t_{n}} \rangle^{S} \\ \vdots & \vdots & \vdots & \vdots \\ \langle g_{t_{n}} \mid B\phi f \rangle^{S} & \langle g_{t_{n}} \mid g_{t_{1}} \rangle^{S} & \cdots & \langle g_{t_{n}} \mid g_{t_{n}} \rangle^{S} \end{pmatrix}$$
(7.31)

We introduce the notation $M^{\{(i_1,j_1),(i_2,j_2),...\}}$, representing the matrix M with rows $i_1, i_2, ...$ and columns $j_1, j_2, ...$ removed. The matrix $M^{\{(0,0)\}}$ is then the matrix G.

As Gram matrices are semi-positive definite, this restriction on the determinant sets a lower bound imposed on the value of $\langle B\phi f | B\phi f \rangle^S$:

$$\langle B\phi f | B\phi f \rangle^{S} \ge \frac{1}{det(G)} \sum_{i=1}^{n} (-1)^{i+1} B(t_{i})^{S} \phi(t_{i})^{S} f(t_{i})^{S} \det(M_{S}^{\{(0,i)\}})$$
 (7.32)

We will name this lower bound χ^S . This can be substituted into Equation 7.29:

$$\chi \ge \langle B\phi f \mid B\phi f \rangle^P + \langle B\phi f \mid B\phi f \rangle^S \tag{7.33}$$

$$\chi \ge \langle B\phi f \mid B\phi f \rangle^P + \chi^S \tag{7.34}$$

$$\chi - \chi^{S} \ge \langle B\phi f \mid B\phi f \rangle^{P} \tag{7.35}$$

We may now perform the usual DM method to obtain the bounds for the form factor at a given value of t for our primary decay. However, now we substitute $\langle B\phi f \mid B\phi f \rangle^P$ with $\chi - \chi^S$ instead of χ .

This saturates the unitarity constraint more strongly, resulting in bounds that are narrower than for the single-decay method.

7.4.1 Comparison with single-decay

		Single Decay		2 Decay Method		% Improvement	
Decay	q^2 (GeV ²)	f_0	f_+	$\int f_0$	f_+	\int_0^{∞}	f_+
BsK	0.0	0.252(105)	0.252(105)	0.248(101)	0.248(101)	2.9	2.9
	5.0	0.310(71)	0.324(115)	0.307(69)	0.321(111)	2.0	2.5
	10.0	0.384(42)	0.453(107)	0.382(41)	0.452(105)	0.4	1.9
	15.0	0.487(22)	0.719(64)	0.486(22)	0.720(63)	-1.8	0.9
BPi	0.0	0.148(153)	0.148(153)	0.148(145)	0.148(145)	5.0	5.0
	5.0	0.210(105)	0.253(146)	0.210(100)	0.253(140)	4.9	4.2
	10.0	0.285(62)	0.414(124)	0.286(59)	0.415(120)	4.5	3.3
	15.0	0.384(30)	0.696(89)	0.385(29)	0.697(88)	1.9	1.5

TABLE 7.2: Comparison of the single decay and 2-decay DM methods for 2000 independent bootstrap events. The "% Improvement" is defined as the amount the standard deviation has decreased using the 2 Decay method compared to the single decay result.

Table 7.2 shows the results for both decays using the single decay and 2-decay methods at several values of q^2 , where all are using 2000 bootstrap events. Generally, both decays showed slight improvements to their errors, around 2% for $B_s \to K\ell\nu$ and

around 4% for $B \to \pi \ell \nu$. It is possible for other decays, where the unitarity condition is saturated more strongly, this method would provide a more substantial improvement to the results.

7.5 Form Factor Curves from the DM method

The Z-fit method has a very convenient feature in that the results are a set of coefficients describing a polynomial. As such, for a given choice of coefficients, it is trivial to evaluate the form factor at any desired value of q^2 .

This is very useful for generating phenomenological results, as we are required to integrate the form factors (or functions containing them) across q^2 bins.

The DM method makes it easy to find form factor bounds at any q^2 , but it is not so obvious how to exploit the bounds over continuous ranges of q^2 when, for example, (partially) integrating the differential decay rate.

One method of comparing DM results with binned experimental results involves taking the midpoint of each q^2 bin and performing the dispersive matrix method to find a distribution of form factors at each q^2 [82]. For each bin, from q_1^2 to q_2^2 , a value of V_{ub} can be estimated using

$$\begin{split} \int_{q_1^2}^{q_2^2} dq^2 \frac{d\Gamma}{dq^2} &\approx |V_{ub}|^2 (q_2^2 - q_1^2) \int dq^2 \frac{G_F^2}{24\pi^3} \frac{\left(q^2 - m_\ell^2\right)^2 \sqrt{E_\pi^2 - M_\pi^2}}{q^4 M_B^2} \times \\ & \left[\left(1 + \frac{m_\ell^2}{2q^2} \right) M_B^2 \left(E_\pi^2 - M_\pi^2 \right) \left| f_+ \left(q^2 \right) \right|^2 \right. \\ & \left. + \frac{3m_\ell^2}{8q^2} \left(M_B^2 - M_\pi^2 \right)^2 \left| f_0 \left(q^2 \right) \right|^2 \right] \Big|_{q^2 = \frac{q_1^2 + q_2^2}{2}} \end{split}$$

This method is simple and does allow for comparison between theory and experiment; however, this "midpoint method" suffers with substantial systematic errors, as it assumes that the form factor at the centre of the bin is the average value across it. Furthermore, even with results generated at many points across each bin, it is not clear how one would account for errors in and correlations between them.

We wish to find a method to generate form factor curves using the DM method that avoids such problems, and instead captures the shape of the form factor curves across the entire kinematic range.

7.5.1 Method

One assumption of the DM method is that the form factor is equally probable anywhere inside the upper and lower bounds given by our unitarity constraint. When considering an infinite number of form factor curves across the q^2 spectrum passing through the resampled form factor points, the bounds represent the maximum and minimum values the curves pass through if they obey unitarity. Our assumption that all form factor values within the bounds are equally likely means that the density of curves is uniform at every value of q^2 .

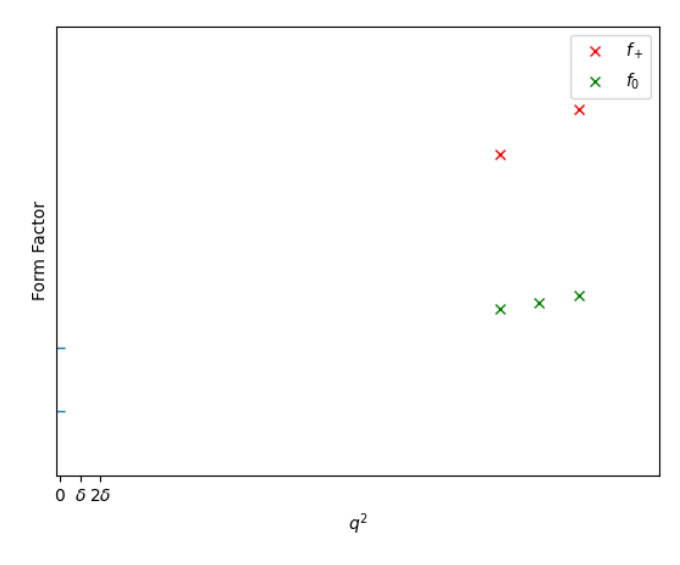


FIGURE 7.7: Example form factor inputs from Lattice data, and their resulting bounds at $q^2 = 0$ Ge V^2 .

The first step is to find the bounds at $q^2 = 0$ and implement the kinematic constraint, following the method described in Section 7.3 [84]. We separately determine the bounds for f_+ and f_0 at $q^2 = 0$ and then randomly and uniformly select a value in the intersection of these bounds as the common $f_+(0) = f_0(0)$ (as shown in Figure 7.7). From here on, both form factors are treated in the same way, and our discussion will apply for either one.

With the point at $q^2=0$ chosen, we have constrained our attention to all form factor curves passing through this point. The extra point is added as new input in the dispersive matrix, allowing us to determine a new bound at $q^2=\delta$, where δ is small. We randomly choose a value satisfying the bound, add the $q^2=\delta$ point to the dispersive matrix and compute bounds at $q^2=2\delta$ (this is visualised in Figures ??-??). We repeat this process to step across the entire physical q^2 region. We repeat this, constructing n_{inner} curves.

In the limits $n_{inner} \to \infty$, $\delta \to 0$, we will construct every form factor curve allowed by unitarity that passes through our resampled input points (and satisfies the kinematic

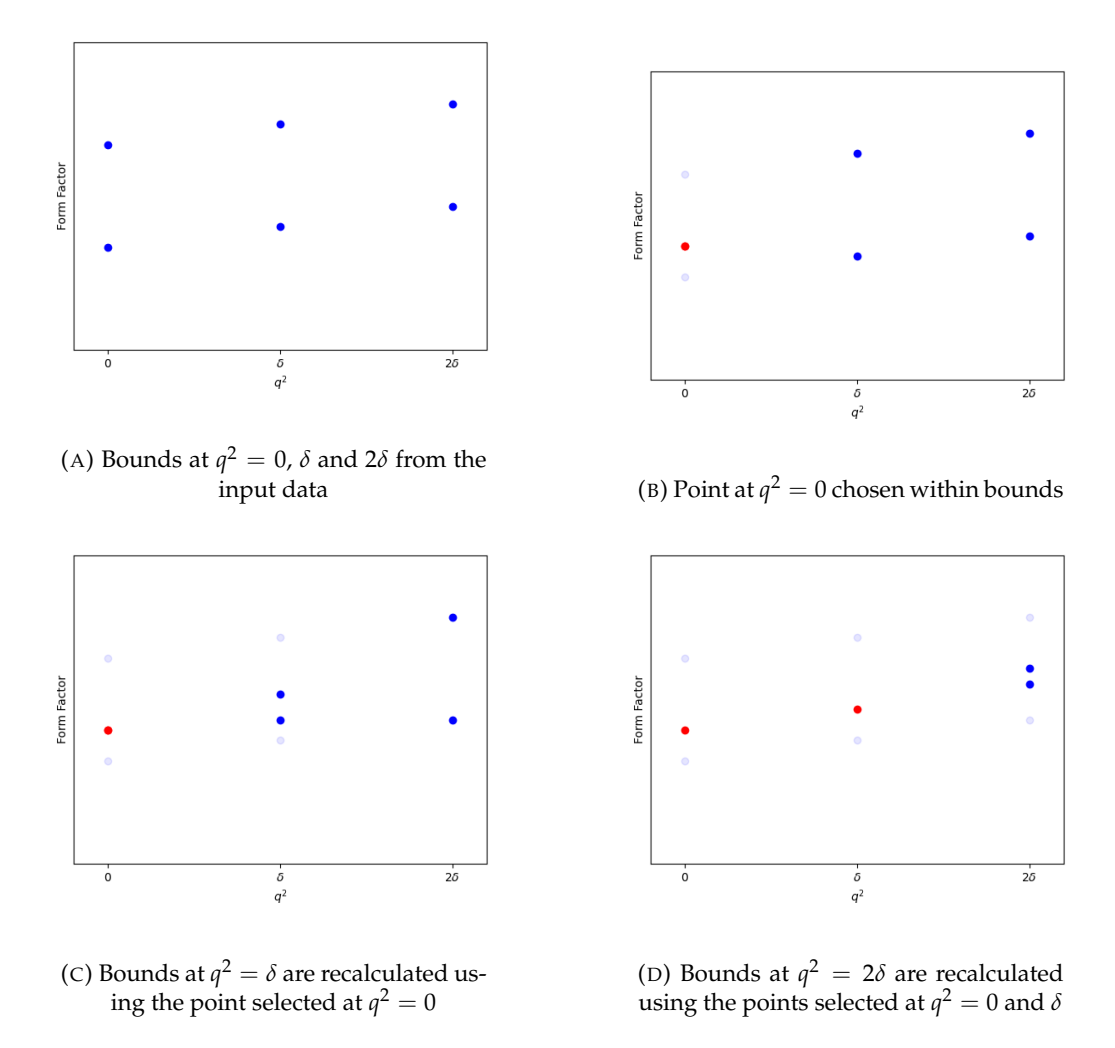


FIGURE 7.8: Step by step visualisation of how form factor curves are generated.

constraint). In practice, we keep δ finite and compute an interpolating function through all the generated points. We must therefore check that δ can be made small enough for it not to affect phenomenological quantities computed using the generated curves (and check for independence of the interpolation method).

This method to generate curves becomes incredibly expensive as the value of δ decreases, as the Dispersive Matrix becomes very large, and more bounds are calculated. Sections 7.5.2 and 7.5.3 show two different approaches to tackle this problem.

Figure 7.9 shows 100 curves generated for a single resample of JLQCD $B \to \pi \ell \nu$ synthetic data points [80], and Figure 7.10 shows the DM method bounds overlaid, showing that these match the envelope of the curves, as expected.

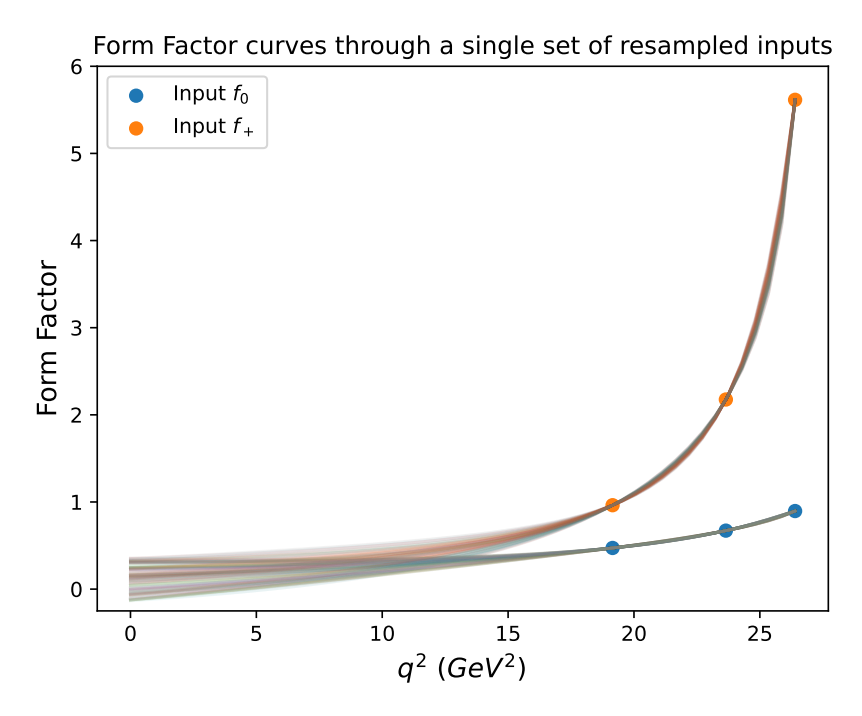


FIGURE 7.9: 100 curves generated for a single resample of JLQCD $B \to \pi \ell \nu$ synthetic data points [80].

7.5.2 Generating curves across bins

The described method allows us to generate form factor curves across the entire q^2 spectrum. However, for phenomenological values, we integrate over bins and, it is only necessary to generate curves over individual bins. This is advantageous as this decreased range means we can use a greater number of points per bin and increase the number of curves we can generate for a fixed computational cost.

The process is identical to that outlined before, however the first step is to $q^2 = t_{lower}$, where t_{lower} is the start of the bin, and we end after n_{points} at $q^2 = t_{upper}$.

To ensure that this method is valid, we test if these segments of form factor curves are equivalent when starting at t_{lower} compared to reaching t_{lower} after a series of small steps. Figure 7.11 shows the distribution of curves generated for a single resample of input lattice data for f_0 and f_+ . Because the kinematic constraint almost always influences f_+ and not f_0 , we observe a uniform distribution for f_0 only. For f_+ , the distribution is not uniform, so if we wish to compare two distributions, we instead perform a two-sample Kolmogorov–Smirnov test [49].

The tests indicate that the distributions of curves through a given q^2 are the same in both cases, indicating that the segments of curves over these ranges are equivalent to those generated over the whole kinematic region.

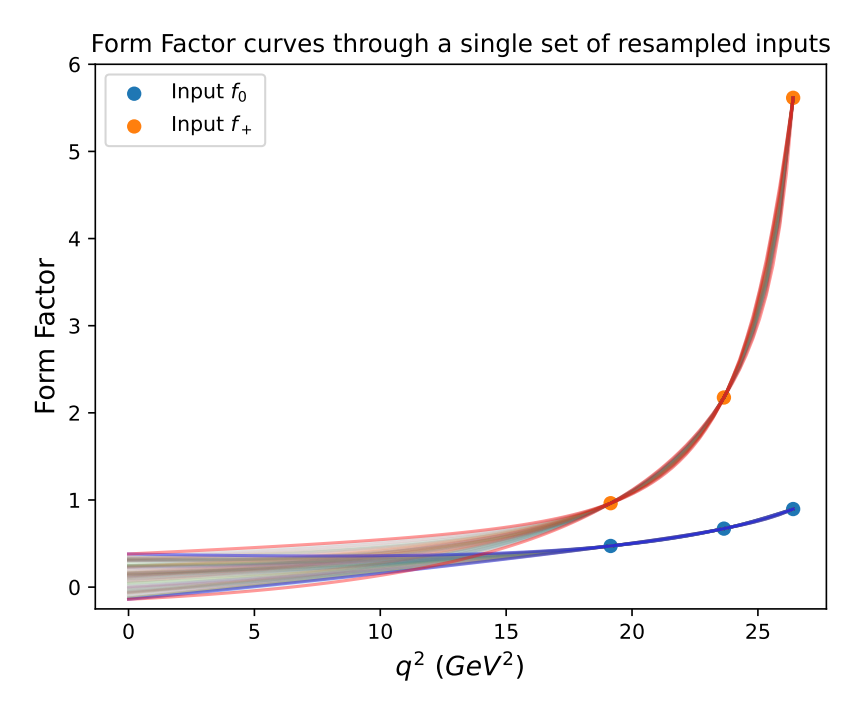


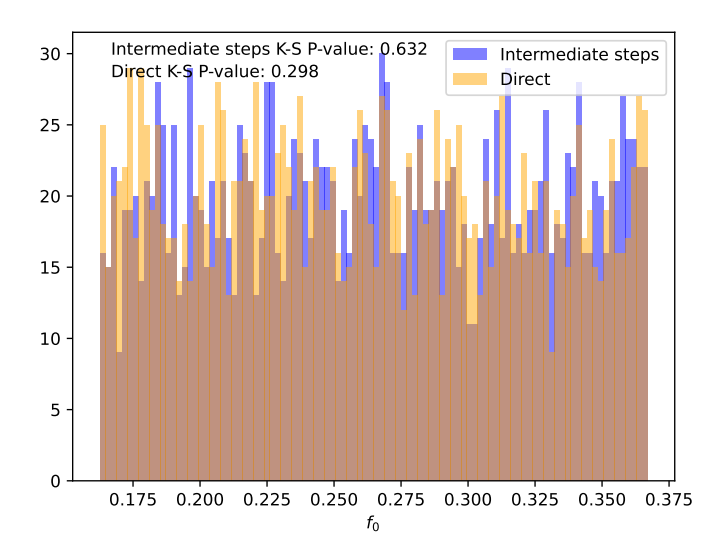
FIGURE 7.10: 100 curves generated for a single resample of JLQCD $B \to \pi \ell \nu$ synthetic data points [80]. The DM method bounds for these points are also plotted.

7.5.3 'Marching' across the full q^2 range

When generating form factor curves over the full q^2 range, the size and number of dispersive matrices increases, more so as δ decreases. However, the upper and lower bounds for adding new points to a curve become closer and closer and effectively coalesce as more points are added. This is because almost all freedom in the curve is exhausted after sufficiently many points have been chosen. We find that we can remove earlier points from the dispersive matrix provided we check that the width of the bound for a new point remains close enough to zero. This speeds up the generation of curves; the dispersive matrix does not keep growing in size and we 'march' across the range of q^2 . In practice, a threshold is set below which the width of the bound is considered to be zero. If the width is above the threshold, then we do not drop an earlier point before computing the next set of bounds. We check that we can make the threshold small enough for it not to affect phenomenological results.

7.5.4 Tests

This section contains various tests to check the validity of the method. As the method is identical for both decays, $B \to \pi \ell \nu$ and $B_s \to K \ell \nu$, tests are only performed on the former.



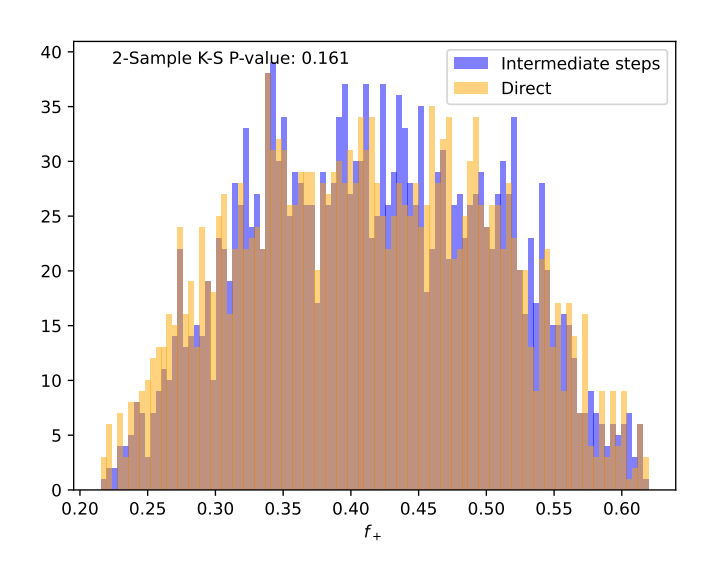


FIGURE 7.11: Comparing the distribution of form factor curves at $q^2 = 10 GeV^2$, when using intermediate points (at $q^2 = 1, 2, ..., 9 \text{ GeV}^2$) and when jumping directly.

7.5.4.1 Direction of curve generation

To convince ourselves that this method is valid, we can check if it is consistent. One test is to see if the curves created are equivalent if they are generated from low-to-high q^2 or high-to-low q^2 .

One assumption of the Dispersive Matrix method is that a single set of bounds gives the minimum and maximum allowed form factor values, and all values within these bounds are equally probable in the absence of other information.

For a distribution of curves through a chosen q^2 , we can test that this distribution aligns with our assumption.

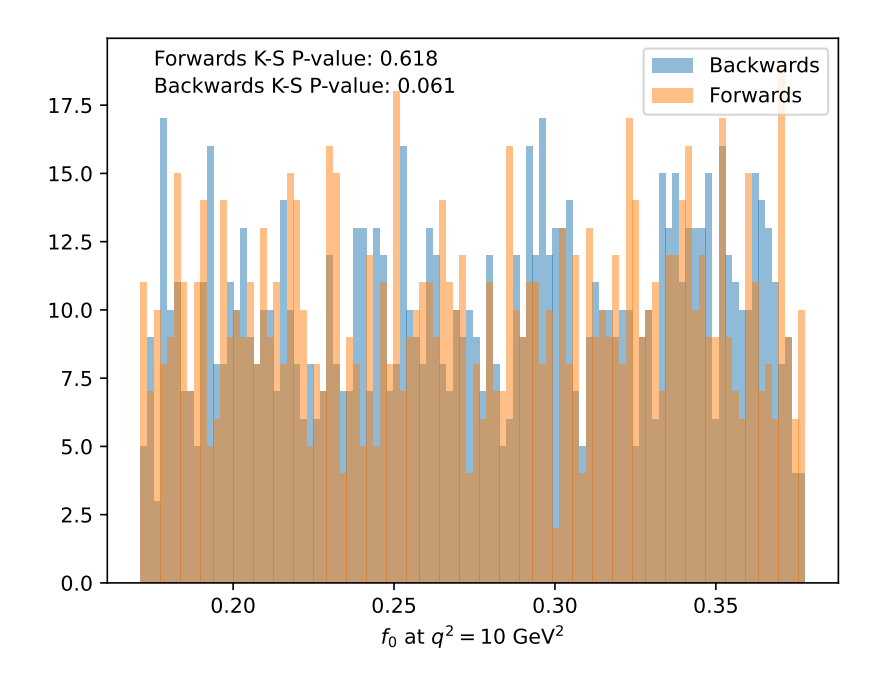


FIGURE 7.12: Comparison of the cross-section of f_0 curves at $q^2 = 10 GeV^2$, when generated forwards and backwards. For each direction, we have the K-S test p-value associated to an underlying uniform distribution.

Figure 7.12 shows that the distribution of curves for f_0 when generated forwards (starting at $q^2 = 0$ GeV²) and backwards (starting at $q^2 = 23.4$ GeV²) are consistent with the same uniform distribution. To generate curves forwards and backwards in the same way, we ignore the kinematic constraint. As in almost all cases this constraint does not impact f_0 , we use this form factor only to assess the impact of the direction of generation. The results of the K-S test provide evidence that the direction of curve generation does not influence the distribution of curves generated, as both are consistent with the uniform distribution.

7.5.4.2 Dependence on δ

Figure 7.13 shows how $\Gamma/|V_{ub}|^2$, the calculated decay rate with the CKM factor removed, changes as δ is varied. We see stability as δ is decreased and that the effects of non-zero δ are much smaller than the variations allowed by unitarity.

7.5.4.3 Dependence on interpolation method

For a sufficiently small value of δ , the points generated should be close enough together that the interpolation method chosen should not impact the curves meaningfully.

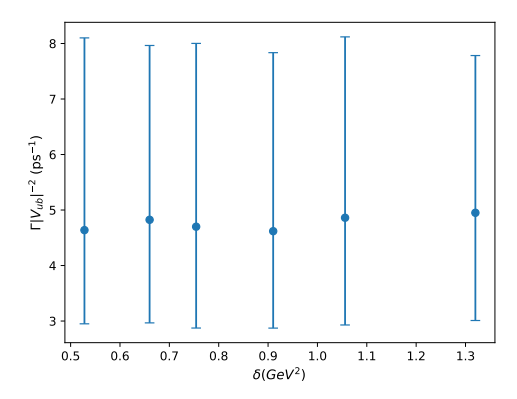


FIGURE 7.13: Calculation of $\Gamma |V_{ub}|^{-2}$ using 500 form factor curves for various values of δ . The plotted bars indicate the median, 16th and 84th percentile values.

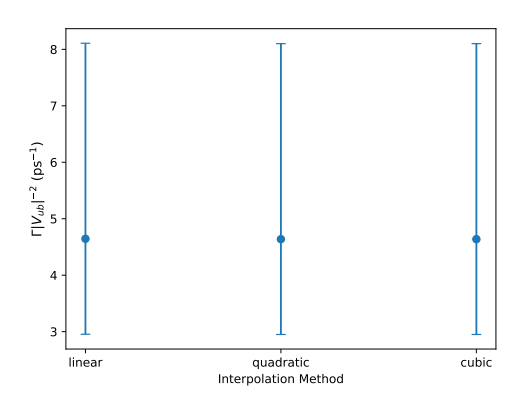


FIGURE 7.14: Calculation of $\Gamma |V_{ub}|^{-2}$ using 500 form factor curves for various interpolation methods. The plotted bars indicate the median, 16th and 84th percentile values.

We can see from figure 7.14 that the effect of our choice of interpolation method does not have an appreciable effect on the results.

7.5.5 Marching parameters

In the implementation of the marching method, we have a number of parameters that influence the degree to which previous points are excluded. The three parameters are as follows:

• "marching threshold" - This parameter is used to specify the maximum width threshold we consider to be effectively zero. If the width calculated is below this threshold, then the next bounds calculated (at the next integer multiple of δ) will use the same number of input points as in this calculation. If the width is found to be above this threshold, then the process continues as normal, but the next bounds calculation will have an additional input point (no input point will be removed).

- "warning threshold" In this method, we dynamically adjust the number of points being used by monitoring the width of the bounds. We have a threshold width that we set that tells us if the bounds become too large. This indicates to us that we have started the marching method, but we have not properly managed the number of points used in our calculation, resulting in the newly calculated bound width to become too large. If this warning triggers, the curve we are generating must not be used.
- "marching delay" This is the number of times the bounds calculation must satisfy the marching threshold condition before the marching procedure begins.
 This should not impact the creation of curves, but practically it can help make sure bounds stay below our warning threshold.

There are a few ways we can test the impact of these parameters, and if they are found to be incorrectly set, they can be changed until they are found to not impact the generation of curves.

The first is to compare the distribution of curves generated at various values of q^2 , when generated forwards and backwards. If these parameters are poorly chosen, then the generation of curves will deviate away from those allowed by unitarity the further along the process we are. This would lead to the distribution of curves at various q^2 not being the same for each direction of curve generation.

The second method is to use the curves to calculate a phenomenological value, such as V_{ub} , while varying the parameters. These parameters are then varied and their impact on V_{ub} results is measured.

7.5.5.1 Marching threshold

To assess the impact of this parameter, we vary our marching threshold and, using experimental data, calculate the decay rate (without the CKM matrix element factor) for 500 curves over many resamples of our lattice data.

Figure 7.15 shows that the impact of the marching threshold, over the range of values chosen, does not have a significant impact on the decay rate.

7.5.5.2 Warning threshold and marching delay

The "warning threshold" parameter does not impact the generation of curves, but instead acts as an indicator that the marching method impacted curve generation. We would also know that this has occurred if the distribution of curves differs from forward/backward generation.

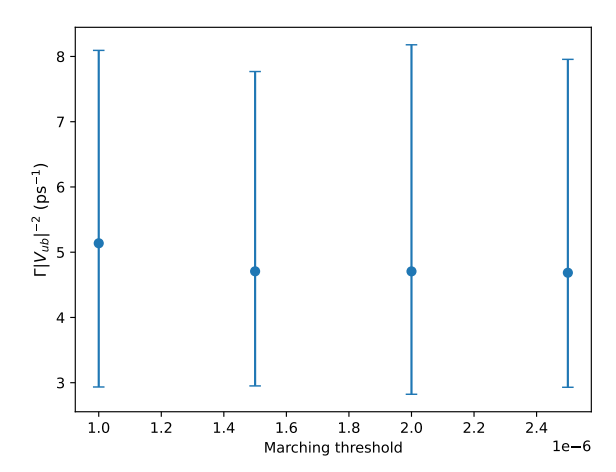


FIGURE 7.15: Dependence of $\Gamma |V_{ub}|^{-2}$ on marching threshold, using 500 curves per threshold.

Similarly, as "marching delay" serves only a practical purpose, variation of this parameter is not necessary as the "warning threshold" warning is not triggered.

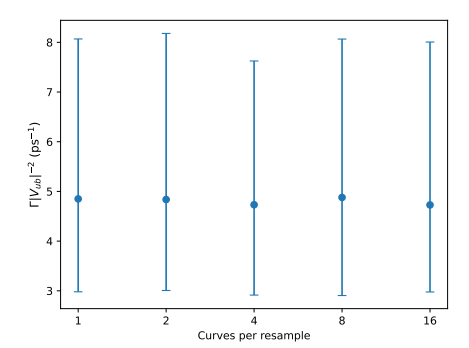
7.5.6 Number of curves per resample

When generating curves, a choice needs to be made on how many curves are generated per resample of our input form factor values. In the limit of an infinite number of resamples, the results generated using the curves will be independent of this choice. In reality, with a fixed amount of computation, we should ensure this choice does not meaningfully affect our results.

One would expect that the best choice would be a single curve generated per resample, however if more curves per resample yields the same results then more curves would be preferable as this cuts down on the overhead of resampling more often (and also from initialization of parallel processing tasks). In reality, the process of generating the curves is much more expensive than all other parts of the process, so this benefit is very minimal.

Figure 7.16 shows how the full range $\Gamma |V_{ub}|^{-2}$ changes as the number of curves per resample is varied. For each, the total number of curves generated is fixed (1760 curves), and a delta value of 0.776 was used.

It can be seen from the graph that, as expected, any effect of the choice is much smaller than the combined effect of all other sources of error (with an extreme enough number of curves per resample, meaning very few resamples, this will not stay true).



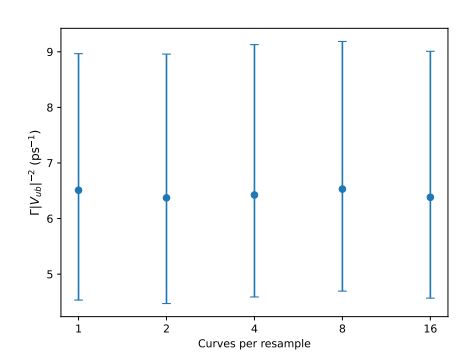


FIGURE 7.16: Effect of varying the number of curves per resample on $\Gamma |V_{ub}|^{-2}$ for $B \to \pi \ell \nu$ (left) and $B_s \to K \ell \nu$ (right)

7.5.7 Extraction of V_{ub} for DM Curves

Unlike the fitting procedure for Z-fits (namely for $B \to \pi \ell \nu$ in this work), the generation of form factor curves using the DM framework cannot be done for lattice and experimental data simultaneously. Hence, we take a set of curve pairs (for f_+ and f_0) generated using lattice data and subsequently combine it with experimental data to extract V_{ub} .

In the case of $B \to \pi \ell \nu$, we have 4 experimental datasets, each giving binned differential decay rate measurements and associated covariance matrices, from Belle and BaBar [64, 68, 62, 65].

For a set of curves generated for this decay, we can extract a V_{ub} for each curve pair, c, by finding the $\theta^2 = |V_{ub}|^2$ that minimises

$$\chi_c^2(\theta) = \sum_e \left(\vec{\Delta}_e - \theta^2 \vec{\Delta}_c^0 \right)^{\mathrm{T}} C_e^{-1} \left(\vec{\Delta}_e - \theta^2 \vec{\Delta}_c^0 \right), \tag{7.36}$$

Here $\vec{\Delta}_e$ is a vector of experimental partial branching fractions for a set of q^2 bins for experiment e, while $\vec{\Delta}_c^0$ are the corresponding quantities, without the CKM factor, computed using the curve pair c. C_e is the experimental covariance matrix.

Table 7.3 gives the average V_{ub} values for these experimental datasets over a sample of 1760 curves generated for $B \to \pi \ell \nu$.

As these curves were generated without experimental data, the shape of $\vec{\Delta}_c^0$ often does not align well with the differential decay rate measurements and the χ^2/DoF for many of these curves is very large, shown in Figure 7.17.

Curves with a large χ^2 fit the experimental differential decay rate distribution poorly, and so we would like to account for this. This is done by using the Bayesian

Experiment	$V_{ub}~(\times 10^3)$
Belle 2010	3.70(65)
Belle 2013	3.84(61)
BaBar 2012	3.66(49)
BaBar 2010	3.70(56)
All experiments excl. BaBar 2010	3.71(56)
All experiments	3.73(59)

Table 7.3: V_{ub} results for $B \to \pi \ell \nu$ from different experiments.

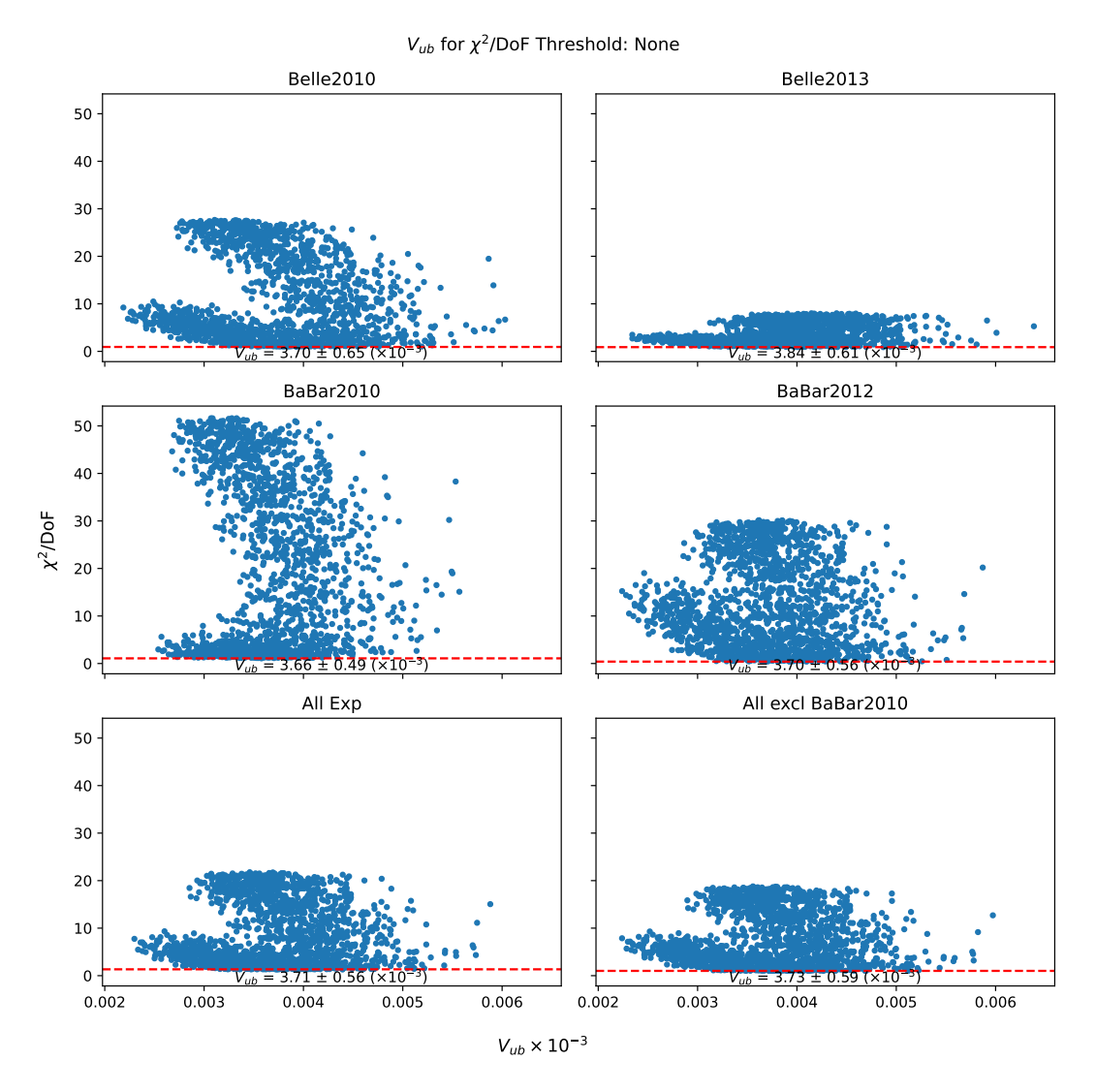


FIGURE 7.17: V_{ub} vs $\chi^2/{\rm DoF}$ for all curves.

viewpoint, where the result for each curve pair is weighted by a likelihood, $e^{-\chi^2/2}$. The posterior for a V_{ub} value θ is

$$\rho(\theta) = \frac{\sum_{c} \exp\left[-\chi_{c}^{2}(\theta)/2\right]}{\sum_{c} \int_{\theta_{0}}^{\theta_{1}} \exp\left[-\chi_{c}^{2}(\theta)/2\right] d\theta},$$
(7.37)

and from this distribution which we can evaluate the expectation value for some function g of θ according to

$$\hat{g} = \int_{\theta_0}^{\theta_1} g(\theta) \rho(\theta) d\theta. \tag{7.38}$$

In particular, we can evaluate the mean and variance of θ to provide an estimated $|V_{ub}|$. We are assuming a uniform prior for θ in the range $[\theta_0, \theta_1]$. We checked that several choices of the range did not change our results within the accuracy quoted. Table 7.4 and figure 7.19 show results for $|V_{ub}|$ for different combinations of experimental inputs. The table also shows the compatibility of our results with those obtained by JLQCD [80] from a BCL Z-fit to the same inputs. The variation from resampling the input form factor values when computing phenomenological results is bigger than the variation seen by changing $n_{\rm inner}$. Hence, we performed the above analysis by generating one curve for each resample and increasing the number of resamplings. We used 1760 form-factor curve pairs.

This is one demonstration of a method to generate form factor curves as functions of q^2 which satisfy dispersive unitarity constraints and can easily be used in phenomenology, maintaining the DM matrix method's feature that no functional form needs to be imposed in advance.

Figure 7.18 shows the differential decay rate from all pairs of curves (f_0 and f_+) with opacity scaling with the relative likelihood (the likelihood relative to the maximum likelihood of all the curves for that experimental dataset).

Experiment	V_{ub} (×10 ³) DM Curves	V_{ub} (×10 ³) BCL z-fit
Belle 2010	4.05(43)	4.10(45)
Belle 2013	4.14(52)	3.91(45)
BaBar 2010	3.55(39)	3.58(41)
BaBar 2012	3.97(48)	4.04(43)
All experiments	3.88(38)	3.93(41)
All excl. BaBar 2010	4.08(45)	4.01(42)

TABLE 7.4: V_{ub} results for $B \to \pi \ell \nu$ for different experimental datasets using the posterior distribution[62, 65, 63, 68].

For $B_s \to K\ell\nu$, we undergo the same procedure as for the Z-fit approach in Section 6.7.2. Our weighted V_{ub} value is $3.74(43) \times 10^{-3}$, with $\chi^2 = 0.042$ (this is compatible with the RBC/UKQCD result of 3.66(31)). Figure 7.20 shows how χ^2 varies with V_{ub} .

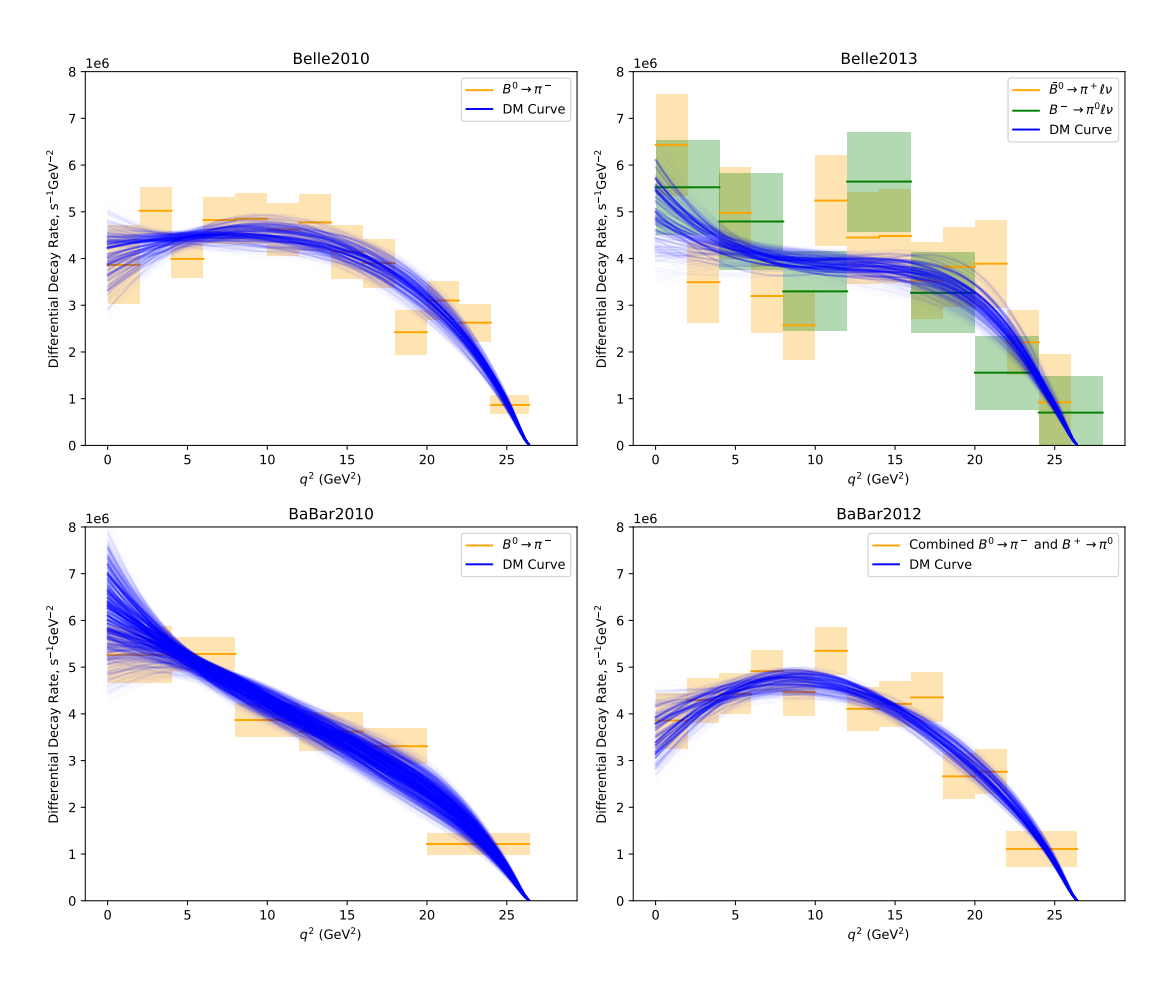


FIGURE 7.18: Differential decay rate of all curve pairs, with opacity scaling with the relative likelihood, alongside binned experimental results.

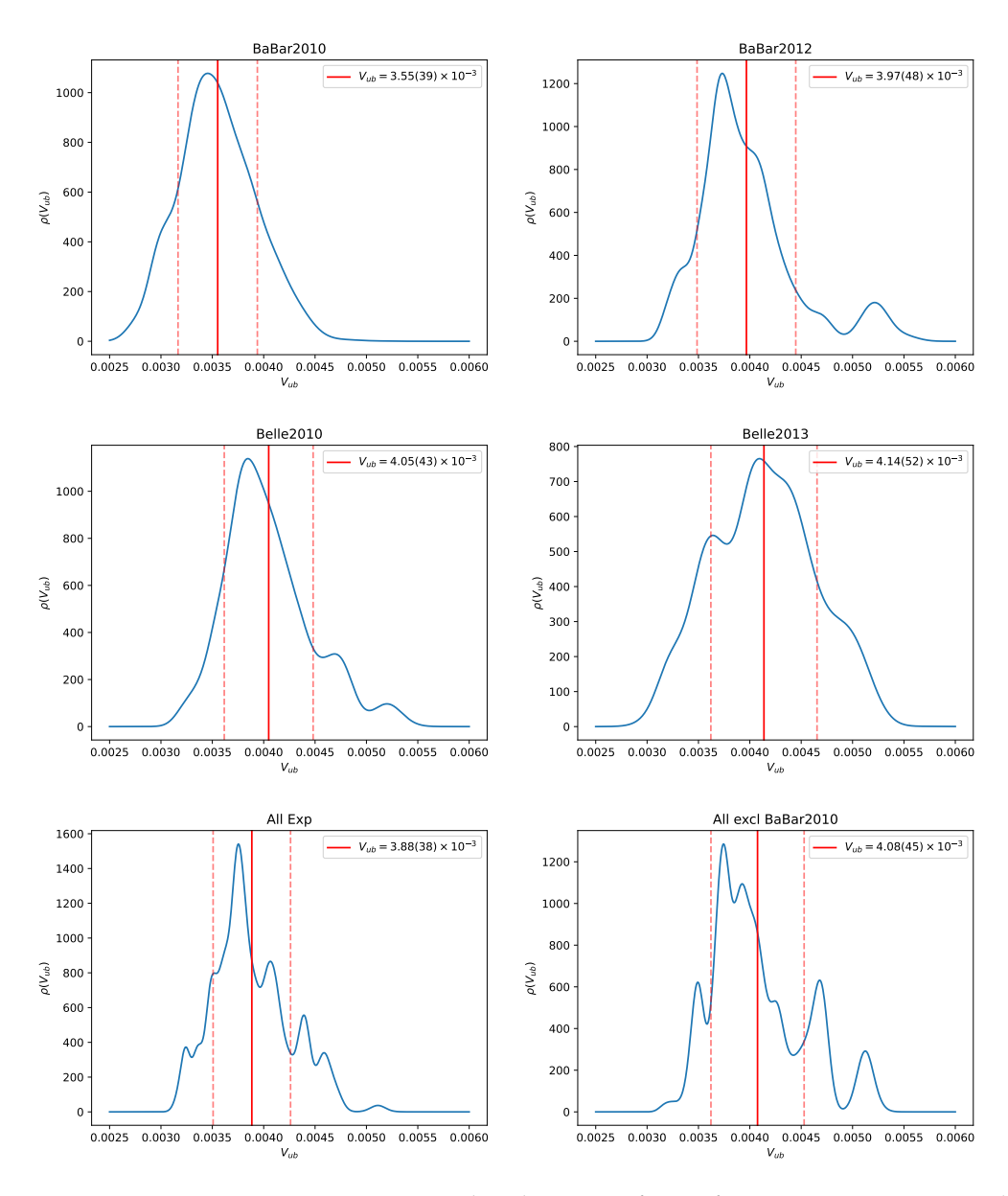


Figure 7.19: Bayesian posterior distributions of V_{ub} for various experimental datasets.

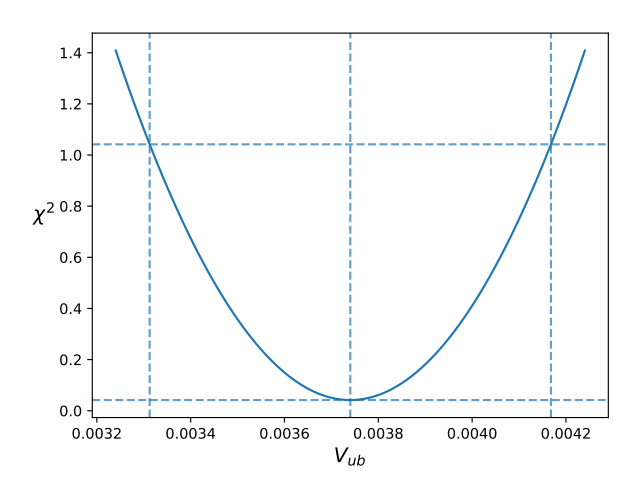


Figure 7.20: χ^2 minimisation to extract V_{ub} for $B_s \to K \ell \nu$ over a sample of 1760 curves, using the LHCb experimental results [76].

Chapter 8

Phenomenology

Two methods in this work, the Z-fit method and the DM curve method, allow for the generation of form factor curves across the kinematic range using unitarity and lattice QCD results. The motivation for doing so is to allow us to measure phenomenological values. This section shows the results using both of these methods, for both decays, for quantities introduced in Section 2.8: the differential decay rate, forward-backward asymmetry, R ratio, and the 'improved' R ratio.

8.1 Comparison with 2015 Results

To test the implementation of phenomenological equations, we test to see if the correct curves and results are recovered when using the central BCL coefficients from the RBC/UKQCD collaboration's 2015 paper [72]. The various results are in Appendix A.

We can see from Figures A.1-A.5 the central curves from the previous phenomenology plots have been successfully refitted.

The Z-fit column in Table A.1 shows the reconstructed values from the BCL coefficients. Some values differ by a small amount, however this can most likely be attributed to updated mass/constant values and any discrepancy between values calculated using the central form factor coefficient values only, and the mean of values generated using the full distribution of coefficients.

8.2 Z-fit and DM Curve Results

Table 8.1 gives a summary of key phenomenological quantities, using either the Z-fit approach or the DM curves method, and Figures 8.1-8.12 compare the q^2 dependence

of these quantities. For all the phenomenological results in this section, the DM curves are not weighted according to experimental results.

These plots consistently show a much wider spread of values for the DM curves method compared to the Z-fit approach. A possible explanation to this is the fundamental difference in the fitting procedure for each of these methods. For a given resample of the synthetic form factor points, the Z-fit approach finds the best fitting set of coefficients, corresponding to a single, most likely, pair of form factor curves. In contrast, for the same synthetic form factor points, the DM curves method can generate curves that may take any form, provided they obey unitarity constraint.

Another possible explanation is the truncation for the z-series. For the Z-fit method used in this work, we are forced to truncate the z-expansion due to the number of degrees of freedom of the data generated on the lattice. This truncation limits the shape of the form factor curves, which may artificially reduce the spread in the results we see in this section. The 2023 RBC/UKQCD paper for $B_s \to K\ell\nu$ uses a Bayesian fitting approach, which allows a larger number of coefficients to be used in the Z-fits [88]. The phenomenological plots shown in this paper more closely resemble those from the DM curves method, suggesting truncation of the z-expansion may play a significant role in the results of this method.

Quantity	Z -fit	DM Curves
$\Gamma(B o \pi \mu \nu)/ V_{ub} ^2$	$5.91(1.22) ps^{-1}$	$5.38(2.38) ps^{-1}$
$\Gamma(B o \pi au u) / V_{ub} ^2$	$4.19(0.75) ps^{-1}$	$3.94(1.02) ps^{-1}$
$\Gamma(B_s \to K \mu \nu) / V_{ub} ^2$	$3.68(0.70) \mathrm{ps}^{-1}$	$6.26(2.29) ps^{-1}$
$\Gamma(B_s \to K au u) / V_{ub} ^2$	$3.54(0.45) ps^{-1}$	$4.50(86) \mathrm{ps}^{-1}$
$R_{\pi}^{ au/\mu}$	0.71(03)	0.80(16)
$R_K^{ au/\mu}$	0.97(07)	0.77(15)
$\frac{1}{\int_{m_{\mu}^2}^{q_{\max}^2} dq^2 \mathcal{A}_{FB}^{B \to \pi\mu\nu}(q^2)/ V_{ub} ^2}$	$0.028(6) \mathrm{ps}^{-1}$	$0.025(22) ps^{-1}$
$\int_{m_{\tau}^2}^{q_{\max}^2} dq^2 \mathcal{A}_{\mathrm{FB}}^{B o \pi au u}(q^2) / V_{ub} ^2$	$1.09(19) \mathrm{ps}^{-1}$	$1.02(29) \mathrm{ps}^{-1}$
$\int_{m_{\mu}^2}^{q_{\max}^2} dq^2 \mathcal{A}_{FB}^{B_s \to K\mu\nu}(q^2) / V_{ub} ^2$	$0.0103(36)~\mathrm{ps^{-1}}$	$0.0403(248) \mathrm{ps^{-1}}$
$\frac{\int_{m_{\tau}^2}^{q_{\max}^2} dq^2 \mathcal{A}_{FB}^{B_s \to K\tau\nu}(q^2) / V_{ub} ^2}{\overline{\mathcal{A}_{FB}^{B \to \pi\mu\nu}}}$	$0.95(13) \mathrm{ps^{-1}}$	$1.27(27) \mathrm{ps}^{-1}$
$\overline{\mathcal{A}}_{\mathrm{FB}}^{B o\pi\mu u}$	0.0048(02)	0.0040(21)
$\overline{\mathcal{A}}_{ ext{FB}}^{B o\pi au u}$	0.262(04)	0.256(13)
$\overline{\mathcal{A}}_{\mathrm{FB}}^{B_{\mathrm{s}} \to K \mu \nu}$	0.0027(04)	0.0059(20)
$\overline{\mathcal{A}}_{\mathrm{FB}}^{B_s o K au u}$	0.2671(25)	0.2823(90)

TABLE 8.1: Various phenomenological quantities calculated using the Z-fit method (with 10000 sets of coefficients) and the DM curves method (1760 curve pairs).

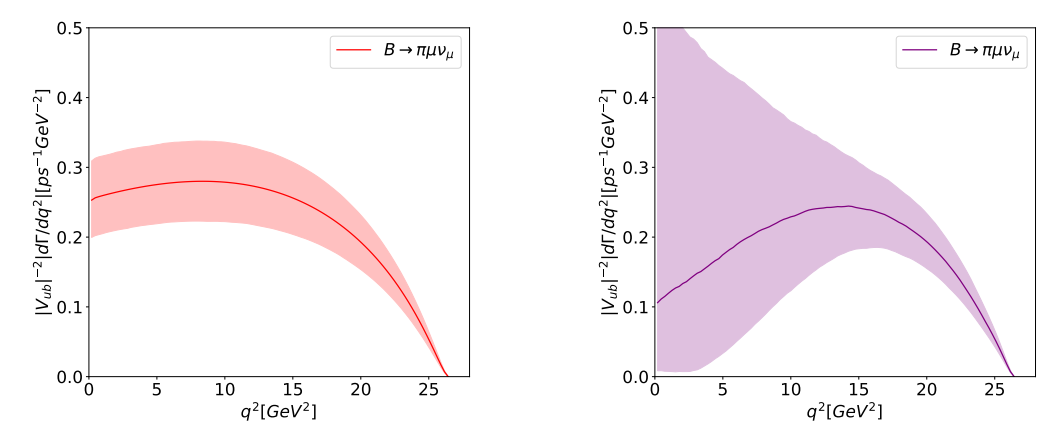


Figure 8.1: Differential decay rate divided by $|V_{ub}|^2$ for $B\to\pi\mu\nu_\mu$ using Z-fit (left) and DM curve (right) methods.

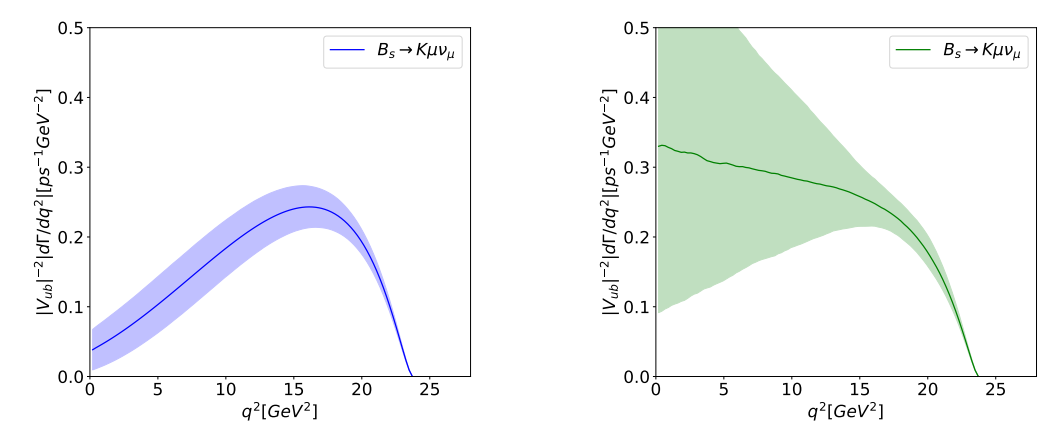


Figure 8.2: Differential decay rate divided by $|V_{ub}|^2$ for $B_s \to K \mu \nu_\mu$ using Z-fit (left) and DM curve (right) methods.

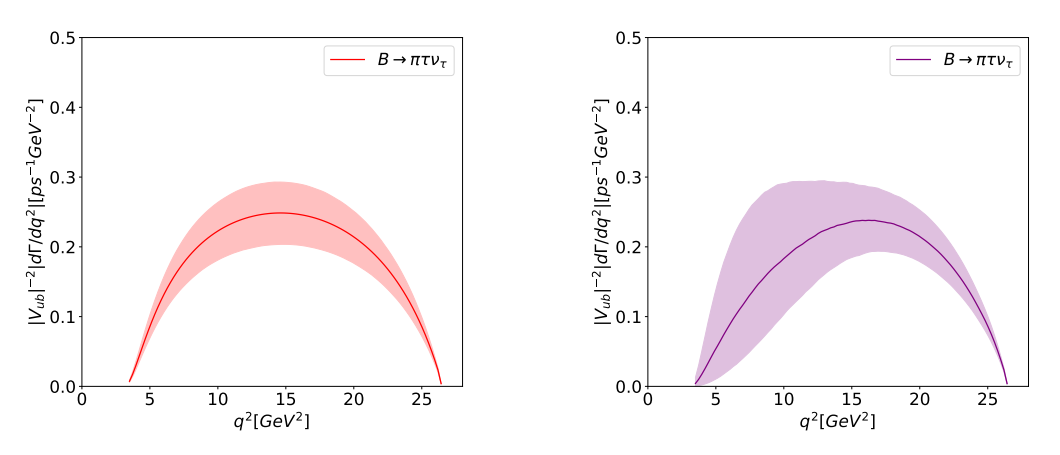


Figure 8.3: Differential decay rate divided by $|V_{ub}|^2$ for $B\to\pi\tau\nu_\tau$ using Z-fit (left) and DM curve (right) methods.

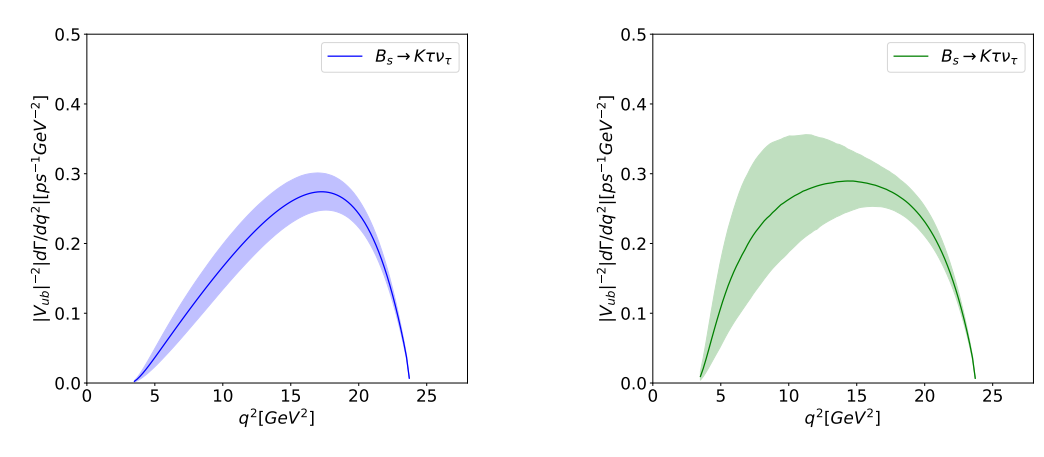


Figure 8.4: Differential decay rate divided by $|V_{ub}|^2$ for $B_s \to K \tau \nu_{\tau}$ using Z-fit (left) and DM curve (right) methods.

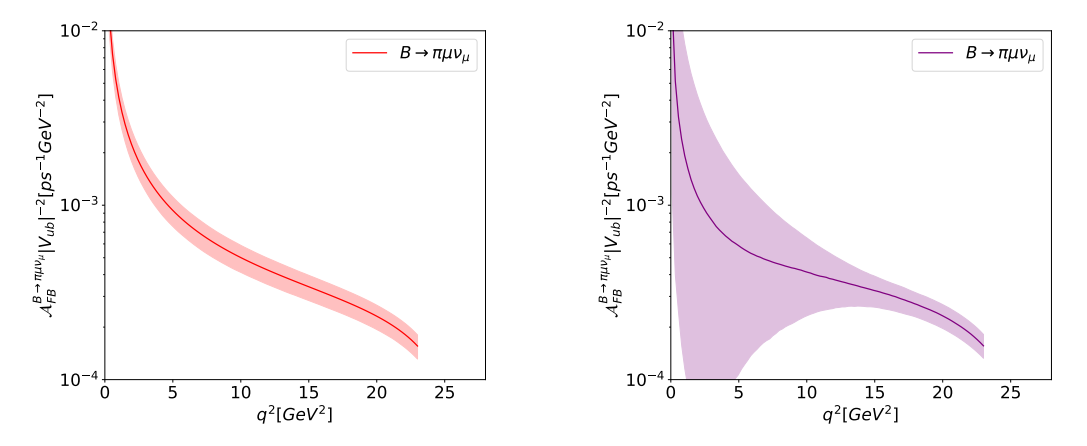


FIGURE 8.5: Forward-backward asymmetry for $B \to \pi \mu \nu_{\mu}$ using Z-fit (left) and DM curve (right) methods.

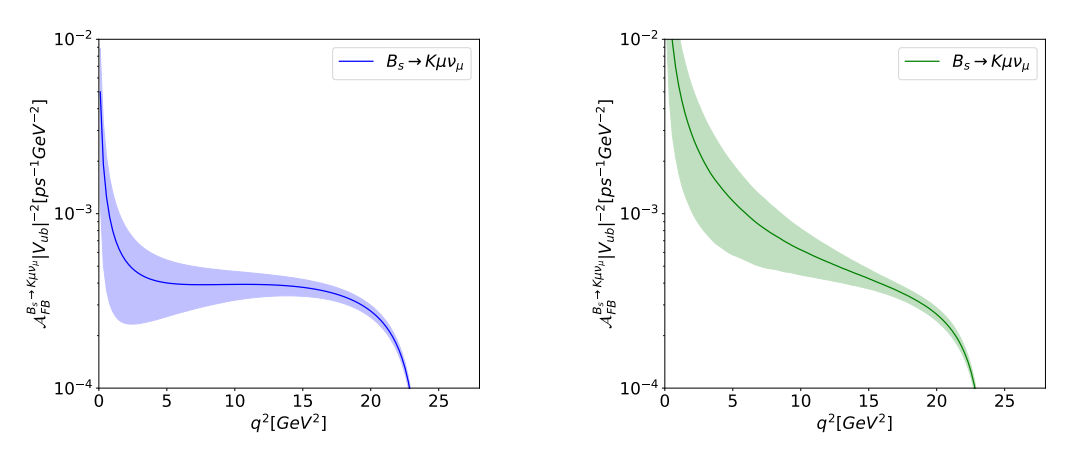


FIGURE 8.6: Forward-backward asymmetry for $B_s \to K \mu \nu_{\mu}$ using Z-fit (left) and DM curve (right) methods.

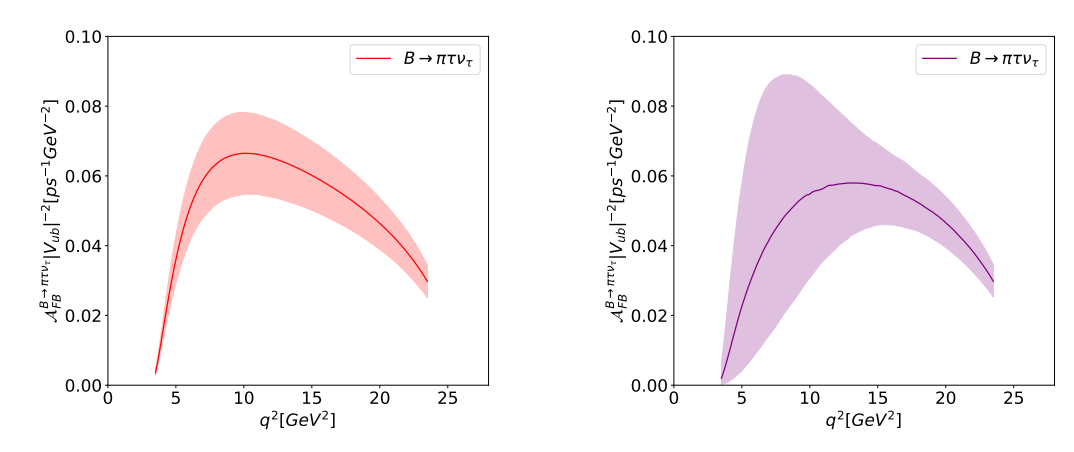


FIGURE 8.7: Forward-backward asymmetry for $B \to \pi \tau \nu_{\tau}$ using Z-fit (left) and DM curve (right) methods.

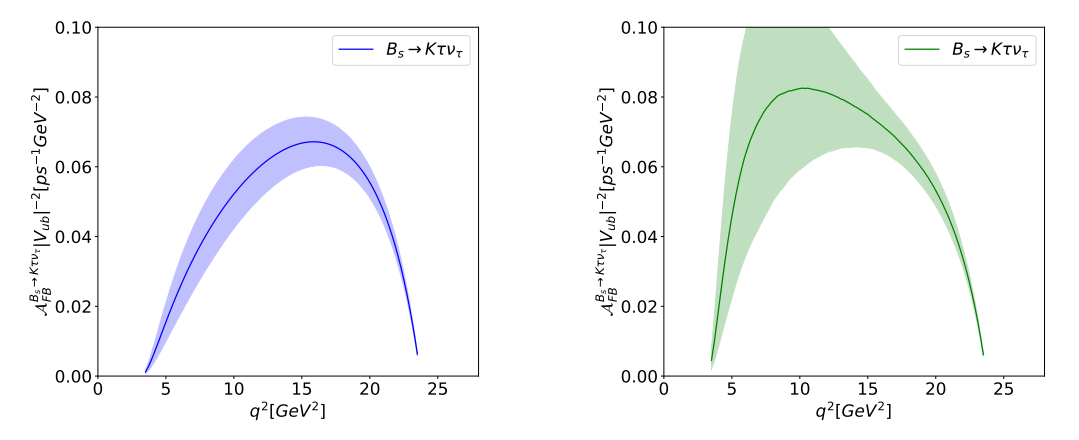


FIGURE 8.8: Forward-backward asymmetry for $B_s \to K \tau \nu_{\tau}$ using Z-fit (left) and DM curve (right) methods.

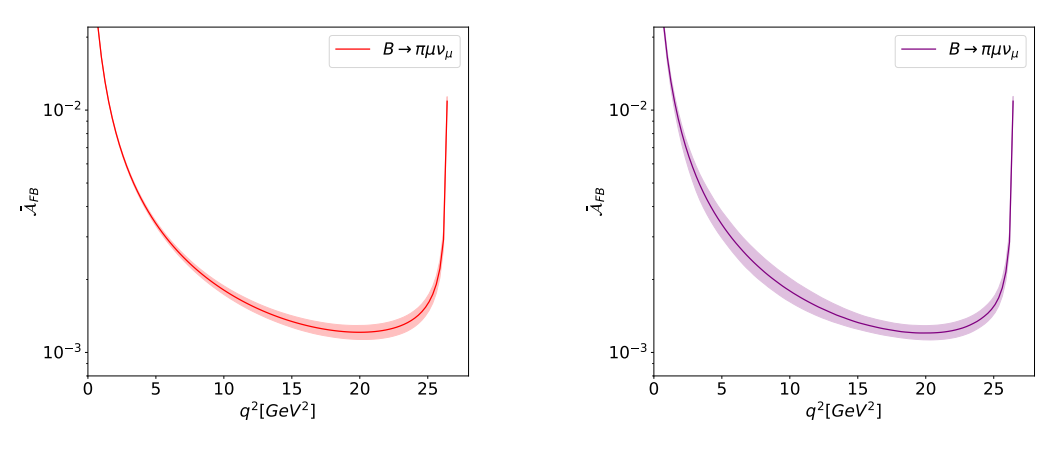


Figure 8.9: Normalized forward-backward asymmetry for $B \to \pi \mu \nu_{\mu}$ using Z-fit (left) and DM curve (right) methods.

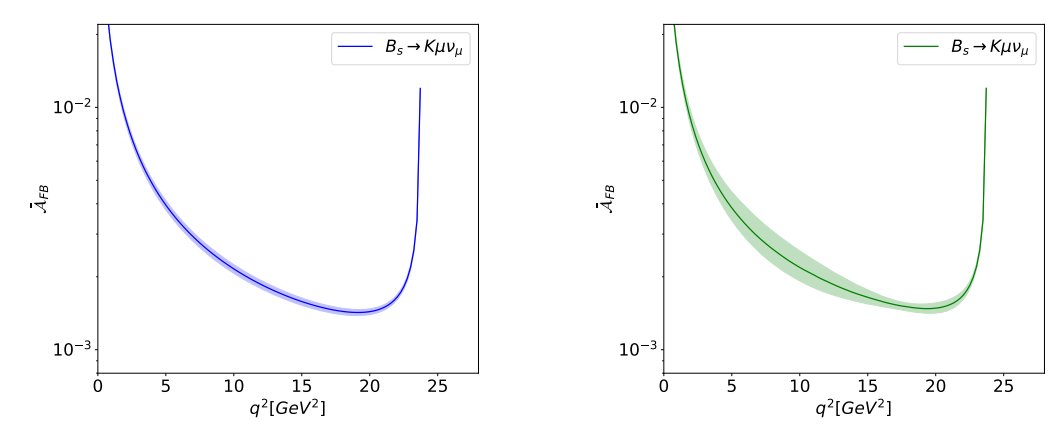


FIGURE 8.10: Normalized forward-backward asymmetry for $B_s \to K \mu \nu_{\mu}$ using Z-fit (left) and DM curve (right) methods.

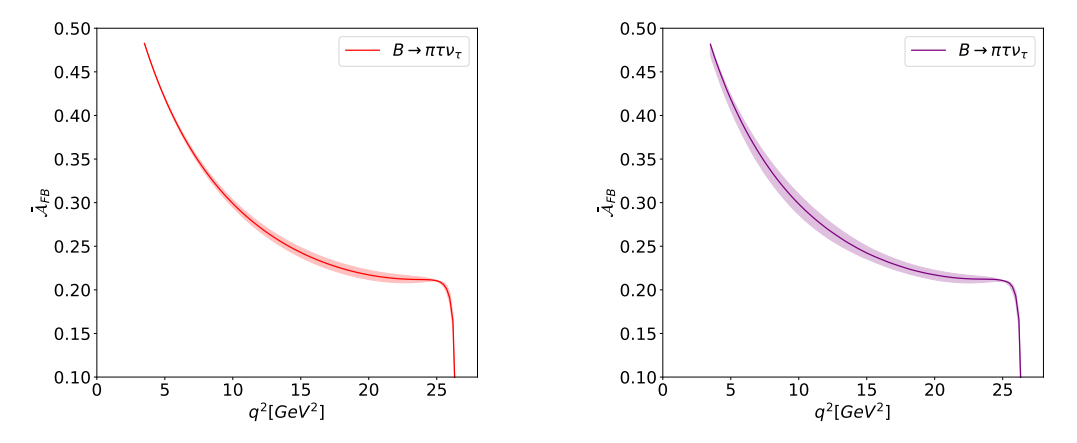


FIGURE 8.11: Normalized forward-backward asymmetry for $B \to \pi \tau \nu_{\tau}$ using Z-fit (left) and DM curve (right) methods.

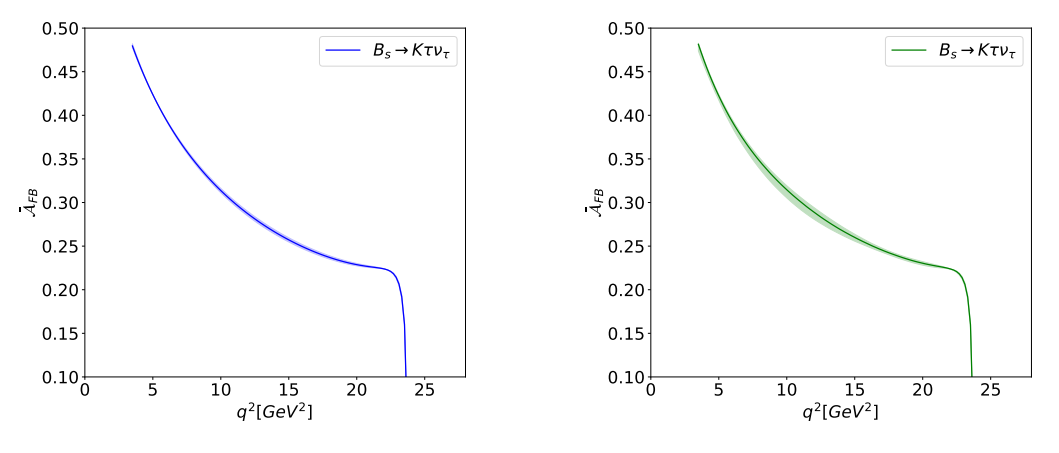


FIGURE 8.12: Normalized forward-backward asymmetry for $B_s \to K \tau \nu_{\tau}$ using Z-fit (left) and DM curve (right) methods.

Chapter 9

Conclusions

This work has seen similar techniques used to try and improve both the Z-fit and dispersive matrix methods, with mixed success. One example of this is the inclusion of information from both decays to saturate the unitarity constraint more fully.

In the case of Z-fits, the unitarity constraint acts as a condition on the fitted coefficients, which never came close to affecting the fitting procedure, and hence did not change the results of the fit. This was seen from the results of the two-sample Kolmogorov–Smirnov test, which determined there was insufficient evidence that the sets of coefficients obtained using the single-decay and two-decay method were drawn from different underlying distributions. This was expected, as the unitarity constraint does not play a significant role in the fitting for $B \to \pi \ell \nu$ and $B_s \to K \ell \nu$.

On the other hand, as the unitarity constraint plays a core role in the DM method, directly determining the limits of the bounds (as the lower and upper bounds are the threshold, beyond which the unitarity constraint is no longer fulfilled), we would expect improvement to the bounds from any extra contribution to the unitarity constraint. For this method, the two-decay variation saw slight improvements to the width of the bounds (around 2-4%). It is possible that for both Z-fits and the DM method, combining results for several decays would be far more significant for a different choice of decays.

For similar reasons to the two-decay method, the use of alternative polynomials for $B_s \to K \ell \nu$ to more accurately implement the unitarity constraint (as unlike for $B \to \pi \ell \nu$, the pair production threshold does not align with the start of the cut) did not see any measurable difference in the Z-fit coefficients. This was tested using the two-sample Kolmogorov–Smirnov test.

When implementing a kinematic constraint on form factors, the application of the DM method in previous literature [78, 84] handled the sampling over the overlap region fairly exhaustively, where many points were chosen over this region and the bounds

at some value of q^2 were calculated for each point, keeping only the most extreme bounds. A faster method of finding these extremal bounds was discussed in Section 7.3, where a minimisation procedure is used. It was then found that for a fixed computational budget, it was more efficient to use the very top and bottom points in the overlap region, as the difference between the bounds found was so small that the results obtained over the many resamples of the lattice form factor data were indistinguishable from those using the optimiser (this is true for the data at present, however in the limit of more and more precise data and more computation, it may prove beneficial to find the true extremal bounds using a minimisation algorithm).

Section 7.5 presents a novel approach to using the DM framework to generate a family of form factor curves consistent with unitarity. This method avoids the parametrization of the Z-fit approach, and any issues from truncating the z-expansion.

The computational cost of the curves method is greatly reduced using two different approaches. Section 7.5.2 introduces the idea of generating curves only across individual bins, as these bins are the regions over which we need to integrate our curves over to compare to experimental data. Generating the curves over a much smaller range of q^2 prevents the Gram matrices becoming too large over subsequent steps. This method was shown to generate curves consistent with those generated over the full range.

The second approach, which was used for all the phenomenological results, is to only include a certain number of the most recent points on the curve in the generation of the next point. This also limits how large the Gram matrices grow, while also allowing for curves to be generated over the full range of q^2 . This method had several systematic variables which were investigated to show, at the scale of the values chosen, that they did not change the curves generated. Although slower in most cases than generation of curves over individual bins, this approach results in curves which can then be used for comparison with any experimental data bins.

The phenomenological values for the two different methods were largely similar for $B \to \pi \ell \nu$, however they differed (sometimes fairly significantly) for $B_s \to K \ell \nu$. The 2023 paper by the RBC/UKQCD collaboration [88] for $B_s \to K \ell \nu$ using a Bayesian fitting method, allowing for a larger number of Z-fit coefficients (not limited by the number of degrees of freedom of the lattice simulation results), shows results using the choice of 2 points for f_+ and 3 for f_0 give poor agreement compared to other choices. This could explain why the Z-fit results for $B \to \pi \ell \nu$ gives better agreement, as we are able to use 3 points for both form factors.

The graphs for the differential decay rate and forward-backward asymmetry highlight the greater spread of curves generated using the DM curves method. The RBC/UKQCD phenomenological plots, that use a much greater number of coefficients (5 for f_0 and 5 for f_+), more closely resemble those from the DM method, suggesting the discrepancy may come from the truncation of the z-expansion.

Where we see good agreement between the two methods for both decays is with the extraction of the CKM matrix element, V_{ub} , as can be seen in Table 9.1. In this table, we see the mean and error of V_{ub} extracted using the Z-Fit method and the DM curve method (using the posterior distribution). The values obtained are very close for both methods, and the errors are of similar size.

Experiment	V_{ub} (×10 ³) - Z-Fit	V_{ub} (×10 ³) - DM Curves
Belle 2010	4.08(45)	4.05(43)
Belle 2013	3.83(44)	4.14(52)
BaBar 2010	3.57(39)	3.55(39)
BaBar 2012	3.92(42)	3.97(48)
All experiments	3.91(41)	3.88(38)
All excl. BaBar 2010	4.00(41)	4.08(45)
LHCb $(B_s \to K \ell \nu)$	3.66(31)	3.74(43)

TABLE 9.1: V_{ub} results for $B \to \pi \ell \nu$ and $B_s \to K \ell \nu$ for different experimental datasets using Z-Fit and DM Curves.

To continue the research presented, there are several options. Firstly, one could expand the analysis to numerous other sources of lattice data, and combine the results to improve precision. This work chose data from JLQCD and RBC/UKQCD and used them to compare proposed improvements to each method, as well as comparing the results of the two methods.

Secondly, this work focusses on two semi-leptonic pseudoscalar to pseudoscalar decays, $B \to \pi \ell \nu$ and $B_s \to K \ell \nu$. There are many other decays of interest with different (and a different number of) form factors that may see improvement from the multiple-decay methods introduced.

Another potential direction of research would be to develop a method of generating the DM curves using lattice and experimental data simultaneously, instead of relying on likelihood weighting.

Appendix A

Reconstruction of phenomenological quantities

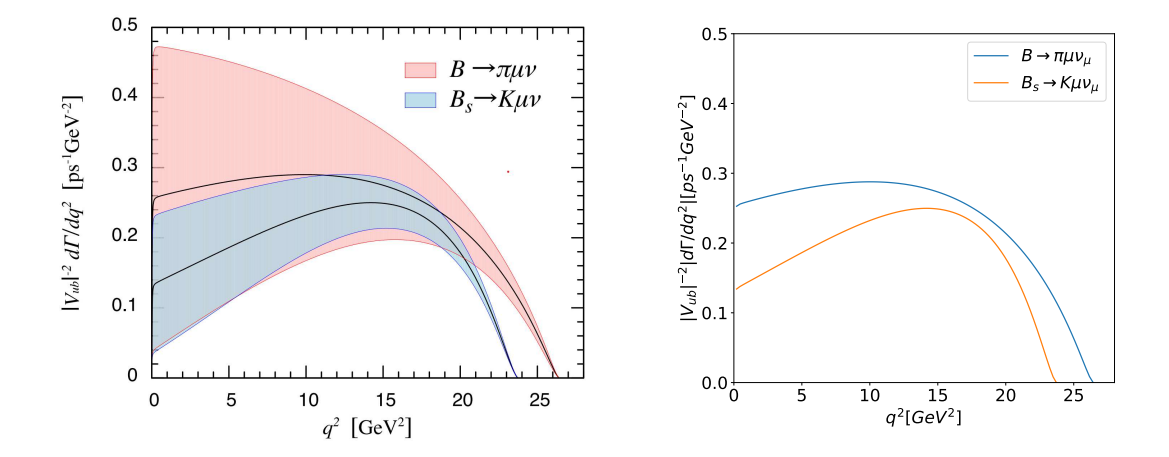


Figure A.1: Differential decay rate divided by $|V_{ub}|^2$ for $B_s \to K \mu \nu_\mu$ and $B \to \pi \mu \nu_\mu$ from the 2015 paper (left) and central value curve reconstruction (right).

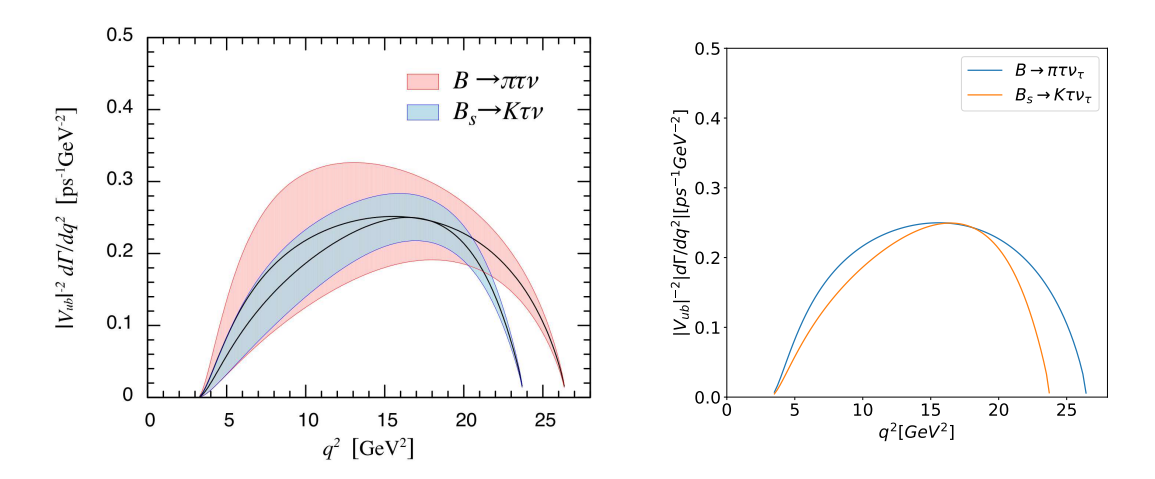


FIGURE A.2: Differential decay rate divided by $|V_{ub}|^2$ for $B_s \to K\tau\nu_{\tau}$ and $B \to \pi\tau\nu_{\tau}$ from the 2015 paper (left) and central value curve reconstruction (right).

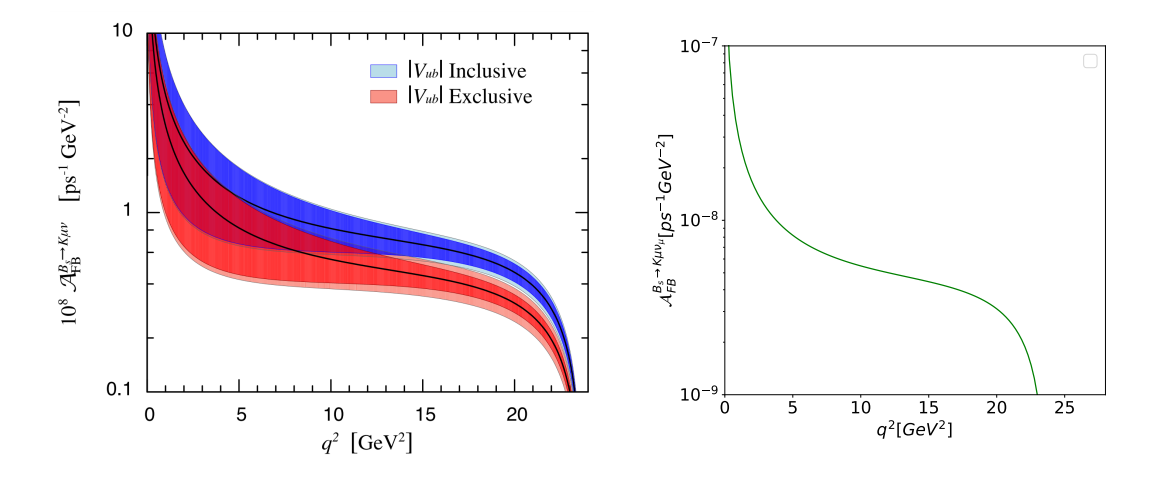


FIGURE A.3: Forward-backward asymmetry for $B_s \to K \mu \nu_{\mu}$ from the 2015 paper (left) and central value curve reconstruction (right).

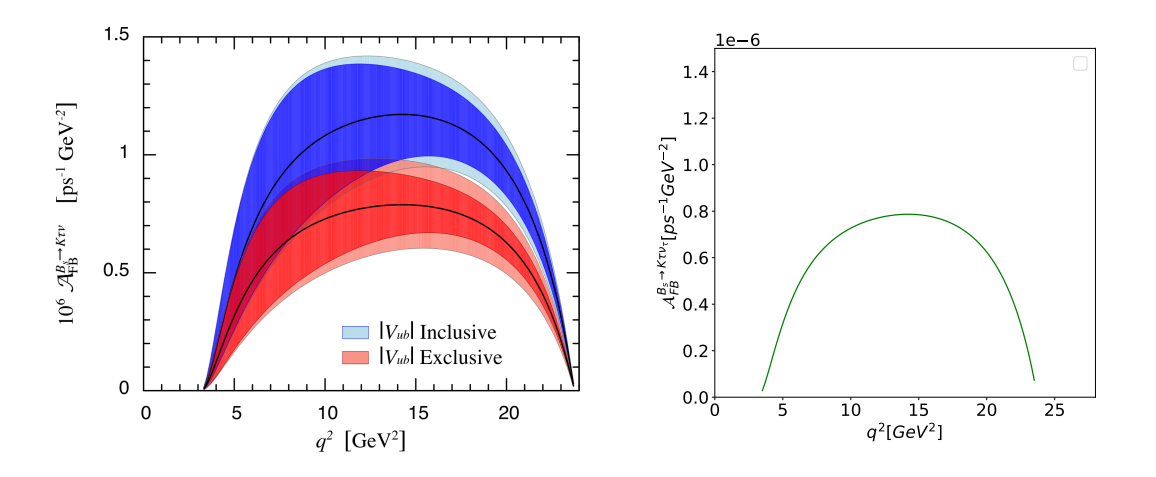


FIGURE A.4: Forward-backward asymmetry for $B_s \to K\tau\nu_{\tau}$ from the 2015 paper (left) and central value curve reconstruction (right).

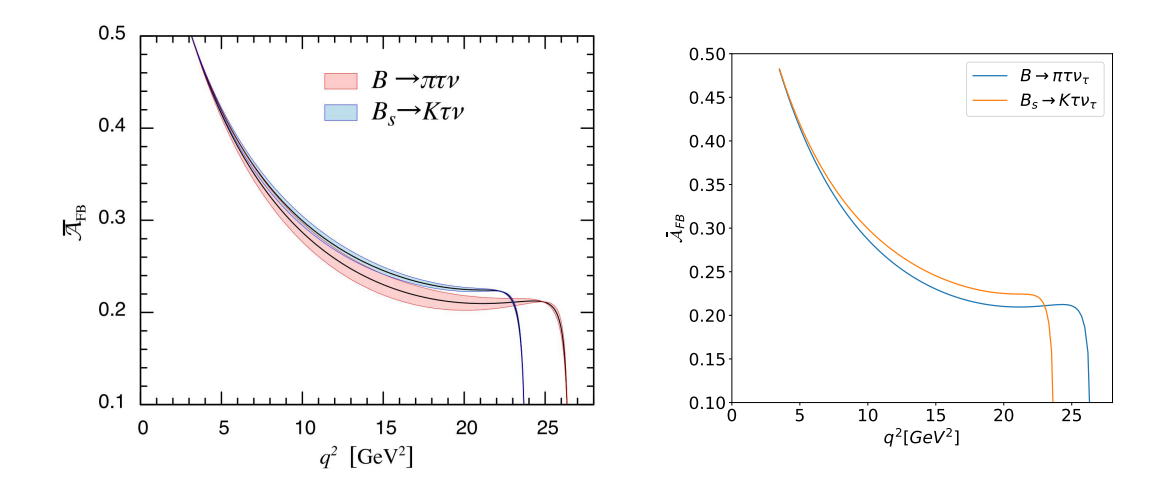


FIGURE A.5: Normalized forward-backward asymmetry for $B \to \pi \tau \nu_{\tau}$ and $B_s \to K \tau \nu_{\tau}$ from the 2015 paper (left) and central value curve reconstruction (right).

Quantity	2015 Result	Reconstructed Central Value
$\Gamma(B o \pi \mu \nu)/ V_{ub} ^2$	$6.2(2.5) ps^{-1}$	$6.20 \mathrm{ps}^{-1}$
$\Gamma(B o \pi au u)/ V_{ub} ^2$	$4.3(1.2) ps^{-1}$	$4.27 \mathrm{ps}^{-1}$
$\Gamma(B_s \to K\mu\nu)/ V_{ub} ^2$	$4.55(1.08) \mathrm{ps}^{-1}$	$4.55 ps^{-1}$
$\Gamma(B_s \to K au u) / V_{ub} ^2$	$3.52(0.60) ps^{-1}$	$3.51 \mathrm{ps}^{-1}$
$R_{\pi}^{ au/\mu}$	0.69(19)	0.69
$R_K^{ au/\mu}$	0.77(12)	0.77
$\frac{R_K^{\tau/\mu}}{\int_{m_\mu^2}^{q_{\text{max}}^2} dq^2 \mathcal{A}_{\text{FB}}^{B \to \pi\mu\nu}(q^2)/ V_{ub} ^2}$	$0.028(19) \mathrm{ps}^{-1}$	$0.028 \mathrm{ps^{-1}}$
$\int_{m_{\tau}^2}^{q_{\max}^2} dq^2 \mathcal{A}_{\mathrm{FB}}^{B \to \pi \tau \nu}(q^2) / V_{ub} ^2$	$1.08(35) ps^{-1}$	$1.07 \mathrm{ps}^{-1}$
$\int_{m_{\mu}^2}^{q_{\text{max}}^2} dq^2 \mathcal{A}_{\text{FB}}^{B_s \to K\mu\nu}(q^2)/ V_{ub} ^2$	$0.0175(87) \text{ ps}^{-1}$	$0.0179 \mathrm{ps}^{-1}$
$\frac{\int_{m_{1}^{2}}^{q_{\max}^{2}} dq^{2} \mathcal{A}_{FB}^{B_{s} \to K\tau\nu}(q^{2})/ V_{ub} ^{2}}{\mathcal{A}_{FB}^{B \to \pi\mu\nu}}$	$0.93(18) \mathrm{ps^{-1}}$	$0.93 \mathrm{ps}^{-1}$
$\overline{\mathcal{A}}_{\mathrm{FB}}^{B o\pi\mu u}$	0.0044(13)	0.0045
$\overline{\mathcal{A}}_{ ext{FR}}^{B o\pi au u}$	0.252(12)	0.251
$\overline{\mathcal{A}}_{\mathrm{FB}}^{B_s \to K \mu \nu}$	0.0039(11)	0.0039
$\frac{\overline{\mathcal{A}}_{FB}^{B_s \to K\tau\nu}}{\mathcal{A}_{FB}}$	0.2650(79)	0.2645

TABLE A.1: Comparison of RBC/UKQCD $B \to \pi \ell \nu$ phenomenological quantities and the reconstructed values from the central values of the corresponding BCL coefficients.

Appendix B

Derivation of the Outer Function

The susceptibilities are defined from derivatives of Π , leading to subtracted dispersion relations:

$$\chi_{0^{+}}(Q^{2}) \equiv \frac{\partial \Pi_{0^{+}}}{\partial q^{2}} = \frac{1}{\pi} \int_{0}^{\infty} dt \frac{\text{Im}\,\Pi_{0^{+}}(t)}{(t - Q^{2})^{2}},$$
(B.1)

$$\chi_{1^{-}}(Q^{2}) \equiv \frac{1}{2} \frac{\partial^{2} \Pi_{1^{-}}}{\partial (q^{2})^{2}} = \frac{1}{\pi} \int_{0}^{\infty} dt \frac{\operatorname{Im} \Pi_{1^{-}}(t)}{(t - Q^{2})^{3}},$$
(B.2)

where we denote the outgoing lepton-pair momentum, q^2 , as the Mandelstam variable t for clarity.

$$\Pi_{\mu\nu}(Q^2) = i \int d^4x e^{iqx} \langle 0|J_{\mu}(x)J_{\nu}^{\dagger}(0)|0\rangle$$
 (B.3)

$$=i\int \frac{d^4k}{(2\pi)^4} \langle 0|\widetilde{J}_{\mu}(q)\widetilde{J}_{\nu}^{\dagger}(k)|0\rangle \tag{B.4}$$

$$\operatorname{Im} \Pi_{\mu\nu}(Q^2) = \frac{1}{2} \int \frac{d^4k}{(2\pi)^4} \sum_{\Gamma} \prod_{i \in \Gamma} \int \frac{d^3p_i}{(2\pi)^3} \frac{1}{2\omega_i} \langle 0|\widetilde{J}_{\mu}(q)|\Gamma\rangle \langle \Gamma|\widetilde{J}_{\nu}^{\dagger}(k)|0\rangle \tag{B.5}$$

$$.(2\pi)^{8}\delta^{(4)}(q-p_{\Gamma})\delta^{(4)}(k-p_{\Gamma})$$

$$= \frac{1}{8(2\pi)^{2}} \int \frac{\delta(q_{0}-\omega_{B_{s}}-\omega_{K})}{\omega_{B_{s}}\omega_{K}} |\langle 0|\widetilde{J}|B_{s}(p_{1})K(p_{2})\rangle|^{2}\delta^{(3)}(q-p_{\Gamma})d^{3}p_{1}d^{3}p_{2}$$
(B.6)

Using $\int \frac{d^3p}{2E} = \int d^4p \, \delta(p^2 - m^2) \Theta(p_0)$ on momentum p_1 gives:

$$\frac{1}{4(2\pi)^2} \int \frac{d^4 p_1 d^3 p_2}{\omega_K} \delta(p_1^2 - M^2) \Theta(p_{10}) \delta(q_0 - p_{10} - \omega_K) \delta^{(3)}(\vec{q} - \vec{p}_{\Gamma}) |\langle 0| \widetilde{J} | B_s(p_1) K(p_2) \rangle|^2$$
(B.7)

$$= \frac{1}{4(2\pi)^2} \int \frac{d^3 p_2}{\omega_K} \delta((q_0 - \omega_K)^2 - \vec{p}_2^2 - M^2) \Theta(q_0 - \omega_K) |\langle 0| \widetilde{J} | B_s(q, p_2) K(p_2) \rangle|^2$$
 (B.8)

Using the Lorentz-invariance, we may choose the centre of mass frame. We switch to spherical coordinates

$$\vec{p}_2 = p \begin{pmatrix} \cos(\phi)\sin(\theta) \\ \sin(\phi)\sin(\theta) \\ \cos(\theta) \end{pmatrix}$$
(B.9)

Im
$$\Pi_{\mu\nu} = \frac{1}{4(2\pi)^2} \int_0^{q_0} d\omega_K \, p \, \delta(q_0^2 - 2q_0\omega_K + m^2 - M^2) \Theta(q_0 - \omega_K) \times$$

$$|\langle 0|\widetilde{J}|B_s(q_0, \vec{p}, \omega_K)K(q_0, \vec{p}, \omega_K)\rangle|^2 d\phi d\cos(\theta)$$
(B.10)

$$= \frac{p}{8(2\pi)^2 q_0} \int_{-1}^{1} d\cos(\theta) \int_{0}^{2\pi} d\phi |\langle 0|\widetilde{J}|B_s(q_0, \vec{p}, \omega_K)K(q_0, \vec{p}, \omega_K)\rangle|^2$$
 (B.11)

Where $\omega_K=rac{q_0}{2}+rac{m^2-M^2}{2q_0}$. We substitute 2.71 into the above, where

$$p = \begin{pmatrix} \omega_{K} \\ pcos(\phi)sin(\theta) \\ psin(\phi)sin(\theta) \\ pcos(\theta) \end{pmatrix}$$
(B.12)

$$q = \begin{pmatrix} q_0 \\ \vec{0} \end{pmatrix} \tag{B.13}$$

$$\frac{p}{8(2\pi)^{2}q_{0}} \int_{-1}^{1} d\cos(\theta) \int_{0}^{2\pi} d\phi \left[2f_{+} \left(q^{2} \right) \left(p_{\mu} - \frac{p \cdot q}{q^{2}} q_{\mu} \right) + f_{0} \left(q^{2} \right) \frac{M^{2} - m^{2}}{q^{2}} q_{\mu} \right] \quad (B.14)$$

$$\left[2f_{+} \left(q^{2} \right) \left(p_{\nu} - \frac{p \cdot q}{q^{2}} q_{\nu} \right) + f_{0} \left(q^{2} \right) \frac{M^{2} - m^{2}}{q^{2}} q_{\nu} \right]$$

$$= \frac{p}{8(2\pi)^{2}q_{0}} \int_{-1}^{1} d\cos(\theta) \int_{0}^{2\pi} d\phi \, 4 \, |f_{+}|^{2} \left[p_{\mu}p_{\nu} - \frac{\omega_{K}}{q_{0}} (p_{\mu}q_{\nu} + q_{\mu}p_{\nu}) + \frac{\omega_{K}^{2}}{q_{0}^{2}} q_{\mu}q_{\nu} \right] \quad (B.15)$$

$$+ |f_{0}|^{2} \left[\frac{(M^{2} - m^{2})^{2}}{q_{0}^{4}} \right] q_{\mu}q_{\nu} + f_{+}f_{0} \left[\frac{M^{2} - m^{2}}{q_{0}^{2}} \left(p_{\mu}q_{\nu} + q_{\mu}p_{\nu} - \frac{\omega_{K}}{q_{0}} (2q_{\mu}q_{\nu}) \right) \right]$$

$$= \frac{p}{(2\pi)^{2}q_{0}} \int_{-1}^{1} d\cos(\theta) \int_{0}^{2\pi} d\phi \, 4 \, |f_{+}|^{2} \left[p_{\mu}p_{\nu} - 2\frac{\omega_{K}}{q_{0}} (p_{\mu}q_{\nu}) + \frac{\omega_{K}^{2}}{q_{0}^{2}} q_{\mu}q_{\nu} \right]$$

$$+ |f_{0}|^{2} \left[\frac{(M^{2} - m^{2})^{2}}{q_{0}^{4}} \right] q_{\mu}q_{\nu} + 2f_{+}f_{0} \left[\frac{M^{2} - m^{2}}{q_{0}^{2}} \left(p_{\mu}q_{\nu} - \frac{\omega_{K}}{q_{0}} q_{\mu}q_{\nu} \right) \right]$$

$$(B.16)$$

We look at the integrand as μ , ν varies (only components with non-zero contribution):

$$\begin{array}{c|c} \mu, \nu & \text{Integrand} \\ \hline 0, 0 & 4 \, |f_{+}|^{2} \left(\omega_{K}^{2} - \omega_{K}^{2}\right) + |f_{0}|^{2} \frac{(M^{2} - m^{2})^{2}}{q_{0}^{2}} \\ 1, 1 & 4 \, |f_{+}|^{2} p^{2} \cos^{2}(\phi) \sin^{2}(\theta) \\ 2, 2 & 4 \, |f_{+}|^{2} p^{2} \sin^{2}(\phi) \sin^{2}(\theta) \\ 3, 3 & 4 \, |f_{+}|^{2} p^{2} \cos^{2}(\theta) \end{array}$$

Integrating:

$$\mu\nu$$
 Integrand $0,0$ $4\pi|f_0|^2\frac{(M^2-m^2)^2}{q_0^2}$ $1,1$ $4|f_+|^2p^2\pi\frac{4}{3}$ $2,2$ $4|f_+|^2p^2\pi\frac{4}{3}$ $3,3$ $4|f_+|^2p^22\pi\frac{2}{3}$

Therefore

$$\operatorname{Im}\Pi_{\mu\nu} = \frac{p}{8(2\pi)^2 q_0} \left(4|f_+|^2 \frac{4\pi p^2}{3} \delta_{ij} + 4\pi |f_0|^2 \frac{q_\mu q_\nu}{q^2} \frac{(M^2 - m^2)^2}{q_0^2} \right)$$
(B.17)

$$= \frac{1}{q^2} \left(q^{\mu} q^{\nu} - q^2 g^{\mu \nu} \right) \Pi_J^T \left(q^2 \right) + \frac{q^{\mu} q^{\nu}}{q^2} \Pi_J^L \left(q^2 \right) \tag{B.18}$$

$$\operatorname{Im}\Pi^{T}(Q^{2}) = \frac{p^{3}}{6\pi q_{0}}|f_{+}|^{2}$$
(B.19)

$$\operatorname{Im} \Pi^{L}(Q^{2}) = \frac{p}{8\pi q_{0}} \frac{(M^{2} - m^{2})^{2}}{q_{0}^{2}} |f_{0}|^{2}$$
(B.20)

Using $\omega_K^2 - p^2 = m^2$ and $\omega_K = \frac{q_0}{2} + \frac{m^2 - M^2}{2q_0}$, we have

$$p = \left(\left[\frac{q_0}{2} + \frac{m^2 - M^2}{2q_0} \right]^2 - m^2 \right)^{\frac{1}{2}}$$
 (B.21)

$$= \left(\frac{q_0^2}{4} + \frac{(m^2 - M^2)^2}{4q_0^2} - \frac{m^2 + M^2}{2}\right)^{\frac{1}{2}}$$
 (B.22)

$$= \left(\frac{(t-t_{+})(t-t_{-})}{4t}\right)^{\frac{1}{2}} \tag{B.23}$$

We define $z(t;t_0)$ as

$$z(t;t_0) \equiv \frac{\sqrt{t_{\text{cut}} - t} - \sqrt{t_{\text{cut}} - t_0}}{\sqrt{t_{\text{cut}} - t} + \sqrt{t_{\text{cut}} - t_0}},$$
(B.24)

where $t_{cut} = (M+m)^2$ is the pair production threshold and $t_0 = t_{cut} - \sqrt{t_{cut}(t_{cut} - (M-m)^2)}$ is a common choice to make z(t) symmetric around 0 for the range of available t values. This mapping takes the q^2 complex plane onto a unit disc. Therefore,

$$\frac{dz}{dt} = \frac{\sqrt{t_{\text{cut}} - t_0}}{\sqrt{t_{\text{cut}} - t} \left(\sqrt{t_{\text{cut}} - t} + \sqrt{t_{\text{cut}} - t_0}\right)^2}.$$
(B.25)

We define the following functions:

$$W_{+}(t) = \frac{1}{6\pi t^{\frac{1}{2}}} \left(\frac{(t - t_{+})(t - t_{-})}{4t} \right)^{\frac{3}{2}}$$
 (B.26)

$$W_0(t) = \frac{1}{8\pi t^{\frac{3}{2}}} (t_+ t_-) \left(\frac{(t - t_+)(t - t_-)}{4t} \right)^{\frac{1}{2}}$$
 (B.27)

Here we have introduced $t_{\pm} = M \pm m$. We define our outer function, $\phi_i(t; t_0)$:

$$\phi_{i}(t;t_{0}) = \left[\frac{W_{i}(t)}{|dz(t;t_{0})/dt|\chi^{j}(q^{2})(t-Q^{2})^{n_{j}}}\right]^{\frac{1}{2}}$$
(B.28)

We make the common choice, $Q^2 = 0$. $\phi_+(t;t_0)$ and $\phi_0(t;t_0)$ are then given by:

$$\phi_{+}(t;t_{0}) = \left[\frac{W_{+}(t)}{|dz(t;t_{0})/dt|\chi_{1}-t^{3}}\right]^{\frac{1}{2}}$$
(B.29)

$$= \sqrt{\frac{1}{48\pi\chi_{1^{-}}}} \left(\frac{t_{\text{cut}} - t}{t_{\text{cut}} - t_{0}} \right)^{\frac{1}{4}} \left(\sqrt{t_{\text{cut}} - t} + \sqrt{t_{\text{cut}} - t_{0}} \right) (t_{+} - t)^{\frac{3}{4}}$$
 (B.30)

$$\left(\sqrt{t_{\rm cut}-t}+\sqrt{t_{\rm cut}-t_{-}}\right)^{\frac{3}{2}}\left(\sqrt{t_{\rm cut}-t}+\sqrt{t_{\rm cut}}\right)^{-5}$$

$$\phi_0(t;t_0) = \left[\frac{W_0(t)}{|dz(t;t_0)/dt|\chi_{0^+}t^2} \right]^{\frac{1}{2}}$$
(B.31)

$$= \sqrt{\frac{1}{16\pi\chi_{0^{+}}}} \left(\frac{t_{\text{cut}} - t}{t_{\text{cut}} - t_{0}}\right)^{\frac{1}{4}} \left(\sqrt{t_{\text{cut}} - t} + \sqrt{t_{\text{cut}} - t_{0}}\right) (t_{+} - t)^{\frac{1}{4}}$$

$$\left(\sqrt{t_{\text{cut}} - t} + \sqrt{t_{\text{cut}} - t_{-}}\right)^{\frac{1}{2}} \left(\sqrt{t_{\text{cut}} - t} + \sqrt{t_{\text{cut}}}\right)^{-4}$$
(B.32)

Bibliography

- [1] W. Blaschke. "Eine Erweiterung des Satzes von Vitali über Folgen analytischer Funktionen". German. In: *Berichte Math.-Phys. Kl.* 67 (1915). Public Domain in the United States, Google-digitized, pp. 194–200. URL: https://hdl.handle.net/2027/mdp.39015036849837.
- [2] E. Noether. "Invariante Variationsprobleme". ger. In: *Nachrichten von der Gesellschaft der Wissenschaften zu Göttingen, Mathematisch-Physikalische Klasse* 1918 (1918), pp. 235–257. URL: http://eudml.org/doc/59024.
- [3] G. Szegö. Ein Beitrag zur Theorie der Thetafunktionen. Sitzungsberichte der Preussischen Akademie der Wissenschaften. Physikalisch-mathematische Klasse. 1926. URL: https://books.google.co.uk/books?id=tXXmSAAACAAJ.
- [4] R. P. Feynman. "Space-Time Approach to Quantum Electrodynamics". In: *Phys. Rev.* 76 (6 Sept. 1949), pp. 769–789. DOI: 10.1103/PhysRev.76.769. URL: https://link.aps.org/doi/10.1103/PhysRev.76.769.
- [5] R. P. Feynman. "Mathematical Formulation of the Quantum Theory of Electromagnetic Interaction". In: *Phys. Rev.* 80 (3 Nov. 1950), pp. 440–457. DOI: 10.1103/PhysRev.80.440. URL: https://link.aps.org/doi/10.1103/PhysRev.80.440.
- [6] G. C. Wick. "Properties of Bethe-Salpeter Wave Functions". In: Phys. Rev. 96 (4 Nov. 1954), pp. 1124–1134. DOI: 10.1103/PhysRev.96.1124. URL: https://link.aps.org/doi/10.1103/PhysRev.96.1124.
- [7] C. N. Yang and R. L. Mills. "Conservation of Isotopic Spin and Isotopic Gauge Invariance". In: *Phys. Rev.* 96 (1 Oct. 1954), pp. 191–195. DOI: 10.1103/PhysRev.96.191. URL: https://link.aps.org/doi/10.1103/PhysRev.96.191.
- [8] C. S. Wu et al. "Experimental Test of Parity Conservation in Beta Decay". In: *Phys. Rev.* 105 (4 Feb. 1957), pp. 1413–1415. DOI: 10.1103/PhysRev.105.1413. URL: https://link.aps.org/doi/10.1103/PhysRev.105.1413.

[9] Sheldon L. Glashow. "The renormalizability of vector meson interactions". In: Nuclear Physics 10 (1959), pp. 107-117. ISSN: 0029-5582. DOI: https://doi.org/10.1016/0029-5582(59)90196-8. URL: https://www.sciencedirect.com/science/article/pii/0029558259901968.

- [10] Abdus Salam and John Clive Ward. "Weak and electromagnetic interactions". In: *Nuovo Cim.* 11 (1959), pp. 568–577. DOI: 10.1007/BF02726525.
- [11] Yoichiro Nambu. "Quasi-Particles and Gauge Invariance in the Theory of Superconductivity". In: Phys. Rev. 117 (3 Feb. 1960), pp. 648–663. DOI: 10.1103/PhysRev.117.648. URL: https://link.aps.org/doi/10.1103/PhysRev.117.648.
- [12] Olive Jean Dunn. "Multiple Comparisons among Means". In: Journal of the American Statistical Association 56.293 (1961), pp. 52–64. DOI: 10.1080/01621459.1961.10482090. eprint: https://www.tandfonline.com/doi/pdf/10.1080/01621459.1961.10482090. URL: https://www.tandfonline.com/doi/abs/10.1080/01621459.1961.10482090.
- [13] Murray Gell-Mann. "The Eightfold Way: A Theory of strong interaction symmetry". In: (Mar. 1961). DOI: 10.2172/4008239.
- [14] Sheldon L. Glashow. "Partial-symmetries of weak interactions". In: Nuclear Physics 22.4 (1961), pp. 579–588. ISSN: 0029-5582. DOI: https://doi.org/10.1016/0029-5582(61)90469-2. URL: https://www.sciencedirect.com/science/article/pii/0029558261904692.
- [15] J. Goldstone. "Field theories with "Superconductor" solutions". In: *Il Nuovo Cimento* (1955-1965) 19.1 (1961), pp. 154–164. ISSN: 1827-6121. DOI: 10.1007/BF02812722. URL: https://doi.org/10.1007/BF02812722.
- [16] Murray Gell-Mann. "Symmetries of Baryons and Mesons". In: Phys. Rev. 125 (3 Feb. 1962), pp. 1067–1084. DOI: 10.1103/PhysRev.125.1067. URL: https://link.aps.org/doi/10.1103/PhysRev.125.1067.
- [17] Nicola Cabibbo. "Unitary Symmetry and Leptonic Decays". In: *Phys. Rev. Lett.* 10 (12 June 1963), pp. 531–533. DOI: 10.1103/PhysRevLett.10.531. URL: https://link.aps.org/doi/10.1103/PhysRevLett.10.531.
- [18] F. Englert and R. Brout. "Broken Symmetry and the Mass of Gauge Vector Mesons". In: Phys. Rev. Lett. 13 (9 Aug. 1964), pp. 321–323. DOI: 10.1103/PhysRevLett.13.321. URL: https://link.aps.org/doi/10.1103/PhysRevLett.13.321.
- [19] Peter W. Higgs. "Broken Symmetries and the Masses of Gauge Bosons". In: *Phys. Rev. Lett.* 13 (16 Oct. 1964), pp. 508–509. DOI: 10.1103/PhysRevLett.13.508. URL: https://link.aps.org/doi/10.1103/PhysRevLett.13.508.

[20] Abdus Salam and John Clive Ward. "Electromagnetic and weak interactions". In: *Phys. Lett.* 13 (1964), pp. 168–171. DOI: 10.1016/0031-9163(64)90711-5.

- [21] Steven Weinberg. "A Model of Leptons". In: Phys. Rev. Lett. 19 (21 Nov. 1967), pp. 1264–1266. DOI: 10.1103/PhysRevLett.19.1264. URL: https://link.aps.org/doi/10.1103/PhysRevLett.19.1264.
- [22] Li. Ling-Fong and H. Pagels. "Comment on a rigorous bound for the $f_+(0)$ form-factor of K_{l3} decay". In: *Phys. Rev. D* 4 (1971), pp. 255–256. DOI: 10.1103/PhysRevD.4.255.
- [23] Li. Ling-Fong and H. Pagels. "Rigorous bound on K_{l3} decay amplitudes". In: *Phys. Rev.* D 3 (1971), pp. 2191–2195. DOI: 10.1103/PhysRevD.3.2191.
- [24] Susumu Okubo. "Exact Bounds for K_{l3} Decay Parameters". In: *Phys. Rev. D* 3 (11 June 1971), pp. 2807–2813. DOI: 10.1103/PhysRevD.3.2807. URL: https://link.aps.org/doi/10.1103/PhysRevD.3.2807.
- [25] Susumu Okubo. "New Improved Bounds for K_{l3} Parameters". In: *Phys. Rev. D* 4 (3 Aug. 1971), pp. 725–733. DOI: 10.1103/PhysRevD.4.725. URL: https://link.aps.org/doi/10.1103/PhysRevD.4.725.
- [26] Susumu Okubo and I-Fu Shih. "Exact Inequality and Test of Chiral SW(3) Theory in K_{l3} Decay Problem". In: Phys. Rev. D 4 (7 Oct. 1971), pp. 2020–2029. DOI: 10.1103/PhysRevD.4.2020. URL: https://link.aps.org/doi/10.1103/PhysRevD.4.2020.
- [27] H. Fritzsch, Murray Gell-Mann, and H. Leutwyler. "Advantages of the Color Octet Gluon Picture". In: *Phys. Lett. B* 47 (1973), pp. 365–368. DOI: 10.1016/0370-2693(73)90625-4.
- [28] David J. Gross and Frank Wilczek. "Ultraviolet Behavior of Non-Abelian Gauge Theories". In: Phys. Rev. Lett. 30 (26 June 1973), pp. 1343–1346. DOI: 10.1103/PhysRevLett.30.1343. URL: https://link.aps.org/doi/10.1103/PhysRevLett.30.1343.
- [29] Makoto Kobayashi and Toshihide Maskawa. "CP-Violation in the Renormalizable Theory of Weak Interaction". In: *Progress of Theoretical Physics* 49.2 (Feb. 1973), pp. 652–657. ISSN: 0033-068X. DOI: 10.1143/PTP.49.652. eprint: https://academic.oup.com/ptp/article-pdf/49/2/652/5257692/49-2-652.pdf. URL: https://doi.org/10.1143/PTP.49.652.
- [30] H. David Politzer. "Reliable Perturbative Results for Strong Interactions?" In: Phys. Rev. Lett. 30 (26 June 1973), pp. 1346–1349. DOI: 10.1103/PhysRevLett.30.1346. URL: https://link.aps.org/doi/10.1103/PhysRevLett.30.1346.
- [31] K. G. Wilson. "Confinement of quarks". In: Phys. Rev. D 10 (1974), pp. 2445–2459.

[32] Kenneth G. Wilson. "Confinement of quarks". In: Phys. Rev. D 10 (8 Oct. 1974), pp. 2445–2459. DOI: 10.1103/PhysRevD.10.2445. URL: https://link.aps.org/doi/10.1103/PhysRevD.10.2445.

- [33] Kenneth G. Wilson and J. Kogut. "The renormalization group and the ϵ expansion". In: *Physics Reports* 12.2 (1974), pp. 75–199. ISSN: 0370-1573. DOI: https://doi.org/10.1016/0370-1573(74)90023-4. URL: https://www.sciencedirect.com/science/article/pii/0370157374900234.
- [34] J. B. Kogut and L. Susskind. "Hamiltonian Formulation of Wilson's Lattice Gauge Theories". In: *Phys. Rev. D* 11.2 (1975), pp. 395–408.
- [35] Michael Creutz. "Monte Carlo study of quantized SU(2) gauge theory". In: *Phys. Rev. D* 21 (8 Apr. 1980), pp. 2308–2315. DOI: 10.1103/PhysRevD.21.2308. URL: https://link.aps.org/doi/10.1103/PhysRevD.21.2308.
- [36] C. Bourrely, B. Machet, and E. de Rafael. "Semileptonic decays of pseudoscalar particles ($M \rightarrow M' + \ell + \nu_{\ell}$) and short-distance behaviour of quantum chromodynamics". In: Nuclear Physics B 189.1 (1981), pp. 157–181. ISSN: 0550-3213. DOI: https://doi.org/10.1016/0550-3213(81)90086-9. URL: https://www.sciencedirect.com/science/article/pii/0550321381900869.
- [37] BRADLEY EFRON. "Nonparametric estimates of standard error: The jackknife, the bootstrap and other methods". In: *Biometrika* 68.3 (Dec. 1981), pp. 589–599. ISSN: 0006-3444. DOI: 10.1093/biomet/68.3.589. eprint: https://academic.oup.com/biomet/article-pdf/68/3/589/581658/68-3-589.pdf. URL: https://doi.org/10.1093/biomet/68.3.589.
- [38] K. Symanzik. "Continuum limit and improved action in lattice theories: (I). Principles and ϕ^4 theory". In: Nuclear Physics B 226.1 (1983), pp. 187–204. ISSN: 0550-3213. DOI: https://doi.org/10.1016/0550-3213(83)90468-6. URL: https://www.sciencedirect.com/science/article/pii/0550321383904686.
- [39] K. Symanzik. "Continuum limit and improved action in lattice theories: (II). O(N) non-linear sigma model in perturbation theory". In: Nuclear Physics B 226.1 (1983), pp. 205–227. ISSN: 0550-3213. DOI: https://doi.org/10.1016/0550-3213(83)90469-8. URL: https://www.sciencedirect.com/science/article/pii/0550321383904698.
- [40] Lincoln Wolfenstein. "Parametrization of the Kobayashi-Maskawa Matrix". In: Phys. Rev. Lett. 51 (21 Nov. 1983), pp. 1945–1947. DOI: 10.1103/PhysRevLett.51.1945. URL: https://link.aps.org/doi/10.1103/PhysRevLett.51.1945.
- [41] Ling-Lie Chau and Wai-Yee Keung. "Comments on the Parametrization of the Kobayashi-Maskawa Matrix". In: *Phys. Rev. Lett.* 53 (19 Nov. 1984), pp. 1802–1805. DOI: 10.1103/PhysRevLett.53.1802. URL: https://link.aps.org/doi/10.1103/PhysRevLett.53.1802.

[42] Manfred Bauer, B. Stech, and M. Wirbel. "Exclusive Nonleptonic Decays of D, D(s), and B Mesons". In: *Z. Phys. C* 34 (1987), p. 103. DOI: 10.1007/BF01561122.

- [43] David B. Kaplan. "A method for simulating chiral fermions on the lattice". In: *Phys. Lett. B* 288.3–4 (1992), pp. 342–347. DOI: 10.1016/0370-2693(92)91112-M.
- [44] C. Glenn Boyd, Benjamin Grinstein, and Richard F. Lebed. *Model-Independent Determinations of B* \rightarrow $D\ell\nu$, $D^*\ell\nu$ Form Factors. 1995. arXiv: hep-ph/9508211 [hep-ph]. URL: https://arxiv.org/abs/hep-ph/9508211.
- [45] Michael E. Peskin and Daniel V. Schroeder. *An Introduction to Quantum Field Theory*. Reading, USA: Addison-Wesley, 1995.
- [46] C. Glenn Boyd, Benjamín Grinstein, and Richard F. Lebed. "Model-independent determinations of $B \to D\ell\nu$, $D^*\ell\nu$ form factors". In: Nuclear Physics B 461.3 (1996), pp. 493–511. ISSN: 0550-3213. DOI: https://doi.org/10.1016/0550-3213(95)00653-2. URL: https://www.sciencedirect.com/science/article/pii/0550321395006532.
- [47] Laurent Lellouch. "Lattice-constrained unitarity bounds for decays". In: *Nuclear Physics B* 479.1–2 (Nov. 1996), pp. 353–391. ISSN: 0550-3213. DOI: 10.1016/0550-3213(96)00443-9. URL: http://dx.doi.org/10.1016/0550-3213(96)00443-9.
- [48] C. Glenn Boyd, Benjamín Grinstein, and Richard F. Lebed. "Precision corrections to dispersive bounds on form factors". In: *Physical Review D* 56.11 (Dec. 1997), pp. 6895–6911. ISSN: 1089-4918. DOI: 10.1103/physrevd.56.6895. URL: http://dx.doi.org/10.1103/PhysRevD.56.6895.
- [49] Donald E. Knuth. *The Art of Computer Programming, Volume 2: Seminumerical Algorithms*. 3rd. Eq. (15) in Section 3.3.1. Reading, Mass: Addison Wesley, 1998.
- [50] Damir Becirevic and Alexei B. Kaidalov. "Comment on the heavy→light form factors". In: *Physics Letters B* 478.4 (Apr. 2000), pp. 417–423. ISSN: 0370-2693. DOI: 10.1016/s0370-2693(00)00290-2. URL: http://dx.doi.org/10.1016/S0370-2693(00)00290-2.
- [51] Pietro Colangelo and Alexander Khodjamirian. "QCD sum rules, a modern perspective". In: (Oct. 2000). Ed. by M. Shifman and Boris Ioffe, pp. 1495–1576. DOI: 10.1142/9789812810458_0033. arXiv: hep-ph/0010175.
- [52] Q. R. Ahmad et al. "Measurement of the Rate of $v_e + d \rightarrow p + p + e^-$ Interactions Produced by ⁸B Solar Neutrinos at the Sudbury Neutrino Observatory". In: *Phys. Rev. Lett.* 87 (7 July 2001), p. 071301. DOI: 10.1103/PhysRevLett.87.071301. URL: https://link.aps.org/doi/10.1103/PhysRevLett.87.071301.
- [53] R. Frezzotti et al. "Lattice QCD with a chirally twisted mass term". In: *JHEP* 08 (2001), p. 058. DOI: 10.1088/1126-6708/2001/08/058. arXiv: hep-lat/0101001.

[54] Patricia Ball and Roman Zwicky. "New results on $B \to \pi$, K, η decay form factors from light-cone sum rules". In: *Phys. Rev. D* 71 (1 Jan. 2005), p. 014015. DOI: 10.1103/PhysRevD.71.014015. URL: https://link.aps.org/doi/10.1103/PhysRevD.71.014015.

- [55] CKMfitter Group (J. Charles et al.) "CP violation and the CKM matrix: Assessing the impact of the asymmetric *B* factories". In: *Eur. Phys. J. C* 41 (2005). Updated results and plots available at: http://ckmfitter.in2p3.fr, pp. 1–131. arXiv: hep-ph/0406184. URL: http://ckmfitter.in2p3.fr.
- [56] G. Peter Lepage. Lattice QCD for Novices. 2005. arXiv: hep-lat/0506036 [hep-lat]. URL: https://arxiv.org/abs/hep-lat/0506036.
- [57] Michele Maggiore. *A modern introduction to quantum field theory*. Oxford master series in statistical, computational, and theoretical physics. Oxford: Oxford Univ., 2005. URL: https://cds.cern.ch/record/845116.
- [58] Mike Peardon. Lecture Slides: Quantum Chromodynamics on the Lattice. Lecture series for Hampton University Graduate Studies Program, Jefferson Lab, Newport News, Virginia, June 2-20, 2008. Accessed: 2024-11-20. 2008. URL: https://www.jlab.org/hugs/archive/Schedule2008/Peardon-Mike/slides_3.pdf.
- [59] Claude Bourrely, Laurent Lellouch, and Irinel Caprini. "Model-independent description of $B \to \pi l \nu$ decays and a determination of $|V_{ub}|$ ". In: *Phys. Rev. D* 79 (1 Jan. 2009), p. 013008. DOI: 10.1103/PhysRevD.79.013008. URL: https://link.aps.org/doi/10.1103/PhysRevD.79.013008.
- [60] P. A. Boyle et al. " $K \to \pi$ form factors with reduced model dependence". In: *The European Physical Journal C* 69.1–2 (Aug. 2010), pp. 159–167. ISSN: 1434-6052. DOI: 10.1140/epjc/s10052-010-1405-4. URL: http://dx.doi.org/10.1140/epjc/s10052-010-1405-4.
- [61] Christof Gattringer and Christian B. Lang. *Quantum chromodynamics on the lattice*. Vol. 788. Berlin: Springer, 2010. ISBN: 978-3-642-01849-7, 978-3-642-01850-3. DOI: 10.1007/978-3-642-01850-3.
- [62] P. del Amo Sanchez et al. "Study of $B \to \pi l \nu$ and $B \to \rho l \nu$ decays and determination of $|V_{ub}|$ ". In: *Phys. Rev. D* 83 (3 Feb. 2011), p. 032007. DOI: 10.1103/PhysRevD.83.032007. URL: https://link.aps.org/doi/10.1103/PhysRevD.83.032007.
- [63] H. Ha et al. "Measurement of the decay $B^0 \to \pi^- \ell^+ \nu$ and determination of $|V_{ub}|$ ". In: *Phys. Rev. D* 83 (7 Apr. 2011), p. 071101. DOI: 10.1103/PhysRevD.83.071101. URL: https://link.aps.org/doi/10.1103/PhysRevD.83.071101.

[64] Ha H et al. "Measurement of the decay $B^0 \to \pi^- \ell^+ \nu$ and determination of $|V_{ub}|$ ". In: *Phys. Rev. D* 83 (7 Apr. 2011), p. 071101. DOI: 10.1103/PhysRevD.83.071101. URL: https://link.aps.org/doi/10.1103/PhysRevD.83.071101.

- [65] J. P. Lees et al. "Branching fraction and form-factor shape measurements of exclusive charmless semileptonic B decays, and determination of $|V_{ub}|$ ". In: *Phys. Rev. D* 86 (9 Nov. 2012), p. 092004. DOI: 10.1103/PhysRevD.86.092004. URL: https://link.aps.org/doi/10.1103/PhysRevD.86.092004.
- [66] R. Aaij et al. "First Observation of the Decay $B_{s2}^*(5840)^0 \rightarrow B^{*+}K^-$ and Studies of Excited B_s^0 Mesons". In: *Phys. Rev. Lett.* 110 (15 Apr. 2013), p. 151803. DOI: 10.1103/PhysRevLett.110.151803. URL: https://link.aps.org/doi/10.1103/PhysRevLett.110.151803.
- [67] John Ellis. *Higgs Physics*. 2013. arXiv: 1312.5672 [hep-ph]. URL: https://arxiv.org/abs/1312.5672.
- [68] A. Sibidanov et al. "Study of exclusive $B \to X_u \ell \nu$ decays and extraction of $|V_{ub}|$ using full reconstruction tagging at the Belle experiment". In: *Phys. Rev. D* 88 (3 Aug. 2013), p. 032005. DOI: 10.1103/PhysRevD.88.032005. URL: https://link.aps.org/doi/10.1103/PhysRevD.88.032005.
- [69] Andreas Crivellin and Stefan Pokorski. "Can the Differences in the Determinations of V u b and V c b Be Explained by New Physics?" In: *Physical review letters* 114 (July 2014). DOI: 10.1103/PhysRevLett.114.011802.
- [70] Cush. Standard Model of Elementary Particles.

 https://en.wikipedia.org/wiki/File:

 Standard_Model_of_Elementary_Particles.svg. Public Domain. 2014.
- [71] Matthew D. Schwartz. *Quantum Field Theory and the Standard Model*. 3rd ed. Cambridge University Press, 2014.
- [72] J. M. Flynn et al. " $B \to \pi \ell \nu$ and $B_s \to K \ell \nu$ form factors and $|V_{ub}|$ from 2+1-flavor lattice QCD with domain-wall light quarks and relativistic heavy quarks". In: *Phys. Rev. D* 91.7 (2015), p. 074510. DOI: 10.1103/PhysRevD.91.074510. arXiv: 1501.05373 [hep-lat].
- [73] T. Aoyama et al. "The anomalous magnetic moment of the muon in the Standard Model". In: Physics Reports 887 (2020). The anomalous magnetic moment of the muon in the Standard Model, pp. 1–166. ISSN: 0370-1573. DOI: https://doi.org/10.1016/j.physrep.2020.07.006. URL: https://www.sciencedirect.com/science/article/pii/S0370157320302556.

[74] Dimitrina S. Dimitrova, Vladimir K. Kaishev, and Senren Tan. "Computing the Kolmogorov-Smirnov Distribution When the Underlying CDF is Purely Discrete, Mixed, or Continuous". In: *Journal of Statistical Software* 95.10 (2020), pp. 1–42. DOI: 10.18637/jss.v095.i10. URL: https://www.jstatsoft.org/index.php/jss/article/view/v095i10.

- [75] Pauli Virtanen et al. "SciPy 1.0: Fundamental Algorithms for Scientific Computing in Python". In: *Nature Methods* 17 (2020), pp. 261–272. DOI: 10.1038/s41592-019-0686-2.
- [76] R. Aaij et al. "First Observation of the Decay $B_s^0 \to K^- \mu^+ \nu_\mu$ and a Measurement of $|V_{ub}|/|V_{cb}|$ ". In: *Phys. Rev. Lett.* 126 (8 Feb. 2021), p. 081804. DOI: 10.1103/PhysRevLett.126.081804. URL: https://link.aps.org/doi/10.1103/PhysRevLett.126.081804.
- [77] Ho-Meoyng Choi. "Current-Component Independent Transition Form Factors for Semileptonic and Rare D—*π*K Decays in the Light-Front Quark Model". In: *Adv. High Energy Phys.* 2021 (2021), p. 4277321. DOI: 10.1155/2021/4277321. arXiv: 2108.10544 [hep-ph].
- [78] M. Di Carlo et al. "Unitarity bounds for semileptonic decays in lattice QCD". In: *Phys. Rev. D* 104 (5 Sept. 2021), p. 054502. DOI: 10.1103/PhysRevD.104.054502. URL: https://link.aps.org/doi/10.1103/PhysRevD.104.054502.
- [79] Silvano Simula et al. "Exclusive B-meson semileptonic decays from unitarity and lattice QCD". In: *PoS* CKM2021 (2021), p. 045. DOI: 10.22323/1.411.0045. arXiv: 2203.16213 [hep-ph].
- [80] Brian Colquhoun et al. "Form factors of $B \to \pi \ell \nu$ and a determination of $|V_{ub}|$ with Möbius domain-wall fermions". In: *Phys. Rev. D* 106 (5 Sept. 2022), p. 054502. DOI: 10.1103/PhysRevD.106.054502. URL: https://link.aps.org/doi/10.1103/PhysRevD.106.054502.
- [81] Nikolai Husung. Private communication. 2022.
- [82] G. Martinelli, S. Simula, and L. Vittorio. " $|V_{cb}|$ and $R(D^{(*)})$ using lattice QCD and unitarity". In: *Phys. Rev. D* 105 (3 Feb. 2022), p. 034503. DOI: 10.1103/PhysRevD.105.034503. URL: https://link.aps.org/doi/10.1103/PhysRevD.105.034503.
- [83] G. Martinelli, S. Simula, and L. Vittorio. "Exclusive determinations of $|V_{cb}|$ and $R(D^*)$ through unitarity". In: *Eur. Phys. J. C* 82.12 (2022), p. 1083. DOI: 10.1140/epjc/s10052-022-11050-0. arXiv: 2109.15248 [hep-ph].
- [84] Guido Martinelli, Silvano Simula, and Ludovico Vittorio. "Exclusive semileptonic $B \to \pi \ell \nu$ and $B_s \to K \ell \nu$ decays through unitarity and lattice QCD". In: *Journal of High Energy Physics* 2022.8 (Aug. 2022), p. 22. ISSN: 1029-8479. DOI: 10.1007/JHEP08(2022)022. URL: https://doi.org/10.1007/JHEP08(2022)022.

[85] Guido Martinelli, Silvano Simula, and Ludovico Vittorio. "Non-perturbative bounds for $B \to D^{(*)} \ell \nu_\ell$ decays and phenomenological applications". In: *PoS* LATTICE2021 (2022), p. 365. DOI: 10.22323/1.396.0365. arXiv: 2111.10582 [hep-ph].

- [86] R. L. Workman et al. "Review of Particle Physics". In: PTEP 2022 (2022), p. 083C01. DOI: 10.1093/ptep/ptac097.
- [87] Thomas Blake et al. "Dispersive bounds for local form factors in $\Lambda_b \to \Lambda$ transitions". In: *Physical Review D* 108 (Nov. 2023). DOI: 10.1103/PhysRevD.108.094509.
- [88] J. M. Flynn et al. "Exclusive semileptonic $B_s \to K\ell\nu$ decays on the lattice". In: Phys. Rev. D 107 (11 June 2023), p. 114512. DOI: 10.1103/PhysRevD.107.114512. URL: https://link.aps.org/doi/10.1103/PhysRevD.107.114512.
- [89] Guido Martinelli et al. "The DM approach to semileptonic heavy-to-heavy and heavy-to-light *B* decays". In: *PoS* LATTICE2022 (2023), p. 298. DOI: 10.22323/1.430.0298. arXiv: 2211.15131 [hep-ph].
- [90] Maxwell T. Hansen and Toby Peterken. Discretization effects in finite-volume $2 \rightarrow 2$ scattering. 2024. arXiv: 2408.07062 [hep-lat]. URL: https://arxiv.org/abs/2408.07062.
- [91] S. Navas et al. "Review of particle physics". In: *Phys. Rev. D* 110.3 (2024), p. 030001. DOI: 10.1103/PhysRevD.110.030001.